Lunar Regolith Characterization for Solar Wind Implanted Helium-3 using M^3 Spectroscopy and Bistatic Miniature RADAR

SHASHWAT SHUKLA
March, 2019

SUPERVISORS:
Mr. Shashi Kumar
Dr. Valentyn A. Tolpekin

Lunar Regolith Characterization for Solar Wind Implanted Helium-3 using M³ Spectroscopy and Bistatic Miniature RADAR

SHASHWAT SHUKLA
Enschede, The Netherlands, March, 2019

Thesis submitted to the Faculty of Geo-Information Science and Earth Observation of the University of Twente in partial fulfilment of the requirements for the degree of Master of Science in Geo-information Science and Earth Observation.
Specialization: Geoinformatics

SUPERVISORS:
Mr. Shashi Kumar
Dr. Valentyn A. Tolpekin

THESIS ASSESSMENT BOARD:
Prof. Dr. Ir. A. Stein (Chair, ITC Professor)
Dr. Satadru Bhattacharya (External Examiner, Space Application Centre (SAC), Ahmedabad)

Don’t tell me the sky’s the limit when there are footprints on the Moon.

-Paul Brandt

ABSTRACT

The Moon serves as an attic to the Earth's treasure by preserving the volatile repository from the harsh space environment. The exposure of the lunar surface to the solar wind plasma results in the implantation of potential ^3He into the top 1 mm of the regolith. The retention of the ^3He primarily depends on the regional ilmenite content and maturation subject to the solar wind plasma supply. In the present research, an attempt is made to explore the influence of petrophysical properties of the regolith on the retained ^3He using multisensor approach. The retention framework is improved by incorporating the associated effects of space weathering on the regolith materials, which are represented by spectral parameters. The integration of the spectral parameters, plasma flux, and ilmenite content leads to a novel hybrid variable that is directly compared with the in-situ ^3He measurements at the Apollo and Luna landing sites. Considering the independence of the space weathering processes, the correlation analysis suggests that the predicted ^3He contents are in close agreement with the actual abundance. However, all the weathering processes lead to the reduction of Fe^{2+} into the nanophase metallic iron particles, thereby interrelating to each other. The applicability of the weighted average linear combination is utilized to model the unknown inherent relationship between the weathering trends. Upon comparing with the in-situ ^3He, the RMSE reduces to 1.17 ppb compared to the independent approach. The empirical relationship is applied to the Vallis Schroteri region, wherein the high ^3He abundant regions emerge out to be pyroclastic deposits and localized hotspots near the primary rille and Agricola Mountains. It is also observed that the two dominant processes governing the abundance are attenuation of the mafic absorption band depths and reddening of the soil. However, a different scenario all together appears for the ^3He abundance per unit area, wherein the soil chemistry proves to be a deciding factor. The spatial variability of the ^3He abundant regolith is found to be aligned with the episodic space weathering events over the geological timescale, clearly indicated by the cyclic behaviour of the variogram trends. Moreover, the highly retained ^3He content may be oriented at around 135º relative to other directions. The lower cutoff and width increases the spatial variability of the deposition. The retention of the ^3He is found to be associated with the petrophysical properties of the soil. This is clearly illustrated by comparing the retrieved scattering mechanisms, dielectric content, and geotechnical variations. In the research, the utility of the radar backscatter is modelled as a function of incidence angle, dielectric constant and surface roughness. The sensitivity analysis is performed, which provides the bounding limits of the realistic surface parameters and radar configuration. This is fed into the multilayer perceptron neural network for performing the inversion based on multivariate regression. The inverted dielectric constant shows an RMSE of 0.26. The retrieval process is applied to the monostatic data of the landing sites, wherein the inverted values are in close agreement with the actual values. Upon testing the study site, the pyroclastic regoliths are associated with high dielectric constant and increased surface scattering mechanisms. The regolith is also characterized by lower void spaces between the grains and higher relative density. Due to the freshly formed microcraters, the excavation of the rocks from the interior lowers the penetration of the radar wave, thereby increasing the granular packing of the gardened regolith. As the dielectric contrast increases, the retention of the lower ^3He ejecta regolith increases, attributing to the roughness variations. The observation is also aligned with the CPR. Moreover, the abundance is negatively correlated with the void ratio for shorter lag distances. On the contrary, the higher abundant pyroclastic regolith relates well with the surface scattering mechanisms associated with cyclicity. An opposition is also observed in this to the bistatic angle with a more significant exponential depth profile. Furthermore, retention modelling provides new insights into the potential mining operations for the lunar outposts. The study recommends a deeper exploration of the pyroclastic regoliths through rover, thereby contributing to the lunar mining paradigm.

Keywords: Regolith, ^3He, Space Weathering, Solar Wind Plasma, Moon

ACKNOWLEDGEMENTS

Throughout the entire MSc research period, I have received significant support from not only my supervisors but also from my friends and family members. Therefore, I would like to thank each one of them personally.

At first, I am deeply grateful to my supervisors Mr. Shashi Kumar and Dr. Valentyn A. Tolpekin under whose guidance I have been able to complete my research goals. They have helped me to think critically and develop my overall scientific knowledge base. Moreover, their unflinching support, assistance, valuable suggestions and sustained encouragement throughout the course of this investigation is highly acknowledged.

I want to express my sincere gratitude to the MSc course director Dr. Sameer Saran for his constant support throughout the course duration, especially in matters of extending lab timings and considering regular feedbacks.

Next, I want to thank PDS Geosciences Node for providing the free lunar datasets of the Chandrayaan-1 Moon Mineralogy Mapper and Lunar Reconnaissance Orbiter bistatic MiniRF. In this regard, I would like to convey my special thanks to Prof. Tim Swindle from the University of Arizona for making the ^{3}He ground-truth measurements accessible. Without his kind support, it would have been impossible for me to perform the research. Also, Dr. Wenzhe Fa and Dr. Anup Das deserve special mention for helping me out in understanding the theoretical aspects of backscattering modelling. I would also like to convey my sincere gratitude to Mrs. Shefali Agarwal who have had a substantial influence on my academic achievements so far. I am thankful for her scientific thoughts and suggestions.

I am thankful to my friends at IIRS and ITC, especially, Abhisek, Raktim, and Sayantan who have helped to maintain my focus. Moreover, with their help, I was able to remain positive even during stressful situations. Finally, I am also indebted to my parents and sister without whom I would never have made this far. They have always encouraged me in all my academic endeavors, and for that, I am extremely grateful to them.

Shashwat Shukla

TABLE OF CONTENTS

List of Figures iv
List of Tables v
1. Introduction 1
   1.1. Planetary Remote Sensing: A New Vision 1
   1.2. The Moon: A Cornerstone of Understanding Space Weathering Processes 2
   1.3. Importance of Solar Wind Implanted ^3He 3
   1.4. Problem Statement 4
   1.5. Research Identification 5
   1.6. Thesis Outline 6
2. Literature Review 7
   2.1. Evolution of ^3He in the Solar System 7
   2.2. Understanding the Lunar ^3He Retention Scenario 9
   2.3. Advances in Remote Sensing: Lunar Perspective 13
   2.4. Summary 25
3. Study Area and Datasets 27
   3.1. Vallis Schroteri, Aristarchus Plateau, Lunar Nearside: Geological Background 27
   3.2. Lunar Datasets 29
   3.3. Software 30
   3.4. Summary 31
4. Methodology 33
   4.1. Data Preprocessing 33
   4.2. Retention Hypothesis of Solar Wind ^3He 34
   4.3. Petrophysical Characterization of Lunar Regolith 38
   4.4. Multisensor Data Analysis, Interpretation and Validation 41
   4.5. Summary 43
5. Results and Discussion 45
   5.1. Estimation of Solar Wind Implanted ^3He: Implications for In-situ Lunar Mining Operations 45
   5.2. Petrophysical Content Retrieval using Bistatic MiniRF Data Processing 59
   5.3. Multisensor Data Analysis 67
   5.4. Summary 71
6. Conclusion and Recommendations 73
List of References 77
Appendix A 85
Appendix B 87
Appendix C 89

LIST OF FIGURES

Figure 1: Space weathering agents, in the form of ionized radiations and meteorite bombardments. 3
Figure 2: The variability of ^{3}He content with respect to the grain size of several returned samples..............9
Figure 3: The relationship of the measured ^{3}He as a function of Ti content for all the lunar soils. 11
Figure 4: The observed variability trend of retained ^{3}He with the combined properties of Ti content and maturity (Is/FeO)..........12
Figure 5: The plot suggestive of hypothetical optimized origin estimates by considering the NIR ratio and reflectance values of the returned Apollo samples. 16
Figure 6: Radar architecture for a) Monostatic systems and b) Bistatic system, in the lunar perspective.. ..20
Figure 7: Geological Perspective of the Vallis Schroteri over Aristarchus Plateau 29
Figure 8: a) M^3 False Colour Composite (FCC). b) MiniRF S1 Image of the Vallis Schroteri..........31
Figure 9: Flowchart of the adopted methodology in the research. 33
Figure 10: Flowchart of the Chandrayaan - 1 M^3 Data Processing...........38
Figure 11: Flowchart of the LRO MiniRF Data Processing. 40
Figure 12: a) Solar wind plasma flux, normalized with respect to local incidence angle, in the Vallis Schroteri region, and b) Frequency distribution of the plasma fluence. 45
Figure 13: TiO_2 Mapping of the Vallis Schroteri Region..........47
Figure 14: Spectral representation of the space weathering effects. 48
Figure 15: False Colour Composite of the Vallis Schroteri Region. 49
Figure 16: a) Retained ^{3}He in the Vallis Schroteri Region. b) Comparison of FTC/IA with in-situ ^{3}He content. 51
Figure 17: a) Retained ^{3}He in the Vallis Schroteri Region. b) Comparison of weighted averaged hybrid parameter with in-situ ^{3}He content. 52
Figure 18: a) Spatial distribution of ^{3}He abundance per unit area for Vallis Schroteri region. b) Histogram plot of the corresponding areal concentrations..........55
Figure 19: Spatial variability of the ^{3}He distribution..........57
Figure 20: Effect of cutoff on spatial variability in terms of variogram image. 58
Figure 21: a) m-Chi decomposition image of the Vallis Schroteri region. b) CPR image. 59
Figure 22: Simulated radar backscatter return as a function of incidence angle 61
Figure 23: Simulated radar backscatter return as a function of a) surface roughness, and b) dielectric content. 61
Figure 24: 3D Sensitivity plots representing the simulated radar backscatter. 62
Figure 25: Changes in the loss with respect to the number of training iterations performed. 63
Figure 26: Retrieved dielectric constant of the study site from MLP NN-based inversion model..........65
Figure 27: Geotechnical Characteristics of the Vallis Schroteri region.. 67
Figure 28: Multisensor comparison of ^{3}He content, for ejecta cover blanket..........68
Figure 29: Effect of bistatic angle on retained ^{3}He content. 70

LIST OF TABLES

Table 1: Characterization of Regolith based on Relative Density 25
Table 2: Sensitivity Range of Parameters for IEM and MLP Neural Network Inversion Modelling. 40
Table 3: Statistical measures of the solar wind ^{3}He concentration. 54
Table 4: Comparison of the inverted and in-situ dielectric constant values of the Apollo landing sites.. ... 63

1. INTRODUCTION

Following the curiosity of mankind towards solar system science, the Moon obscures a brief overview of the unprecedented reality that lies within the stellar evolution. The purpose of this chapter is to outline the state of the art remote sensing technologies for distant planetary observations, to review the lunar surface, space weathering processes with special emphasis on solar wind and their associated impacts, and finally to specify the importance of the current research work.

1.1. Planetary Remote Sensing: A New Vision

The emergence of planetary systems underlines the importance of space exploration for understanding the physical and geological processes associated with it. This further addresses the need for envisaging the fundamental scientific attributes and applied mission-specific technologies in conjunction with planetary timescale. Stepping towards the twenty-first century, the realm of knowledge has significantly advanced in the stellar science as compared to the traditional solar system studies (Taylor, 1982). In accordance, the increased capability of flying technical instruments to the extraterrestrial space connects the research gap between the theoretical and practical viewpoint of the planetary geosciences (LExSWG, 1992). There exists an interdisciplinary component of remote sensing, which unravels the scientific perspective of any phenomena through remote data acquisition practices. It is the process of procuring information from a target entity without actually coming into contact with it (Lillesand et al., 2008). Ideally, the validation for realising the geochemical and isotopic composition of the Earth's crust can be done through in-situ measurements of the surface samples. However, this becomes a constraint while exploring distant planetary surfaces as direct sampling is not possible. Remote sensing, as a tool, facilitates a unique context in such scenarios by utilizing the spectrum of electromagnetic (EM) radiation and enabling its imaging capabilities for mapping the geological characteristics.

Among different regions of the EM spectrum, the reflected visible to near-infrared radiation provides new insights into the mineralogical exposure of the planetary surfaces. Such behavior originates due to the presence of highly diagnostic absorption features in the wavelength region of approximately 400-1500 nm (Clark & Roush, 1984). Particularly, these features can be identified by measuring the spectrum for each spatial element of an image. This spectral observation considers the geophysical imaging of the surface as an integrated part of imaging spectroscopy (Clark et al., 2003). The primary application of the technique often utilizes the capability of separating materials on the basis of their interaction with the radiation and hence, generating a unique signature. This also has an implication for determining the geological evolution of the sub-crustal processes based on the correlation with the Apollo in-situ data (Clark et al., 2003; Lillesand et al., 2008). Furthermore, the surface exhibiting an abundant mineral deposit identifies the characterization of the soil grains by comparing their physical properties (Ulaby et al., 1982). This can be well evaluated by focusing the microwave region of the EM wave through radar remote sensing (Woodhouse, 2006). The sensitivity of radar echo towards surface roughness, moisture, wavelength and dielectric property makes it significant in mapping the physiography of a planet (Ulaby et al., 1986). This also yields higher subsurface penetration in contrast to the conventional imaging spectroscopy, thereby expanding the scope of understanding the inner dynamics of the planet.

One of the nearest astronomical bodies to the Earth is the Moon, which has been the key source of evidence in terms of experimental observations and validation (LExSWG, 1992). In 1969, as stated by Neil Armstrong, "That's one step for a man, one giant leap for mankind", revolutionised the potential of manned missions to reach the planetary surfaces and till now, the Moon is the only manifestation that can be used to unravel the mystery of the solar system (Heiken et al., 1991). Several remote sensing studies have been conducted for investigating the nature of the lunar surface with a geological outlook whilst looking for the possibility of future human colonization (Campbell et al., 1997; Clark & Roush, 1984; Gaddis et al., 1985; Hawke & Bell, 1981; Heiken et al., 1991; Korotev et al., 2003). This opens new exploration strategies and intellectual policies for providing new insights into the essential life-sustaining segments of the Moon.

1.2. The Moon: A Cornerstone of Understanding Space Weathering Processes

In geology, the 'Rosetta' stone is often interpreted as revealing ancient civilizations of Egypt and hence, a key origin for extracting valuable information from the past (Andrews, 1985). From a remote sensing perspective, the Moon, being the geological Rosetta of the Earth, has always been a great source of interest for understanding the evolution of the solar system. This is because of the development and refinement of remote sensing techniques that can be well demonstrated and compared with the in-situ lunar samples of Apollo and Luna landing sites. Apart from this, the propinquity of the Moon drives the reason of it being explored as a calibration site for other distant planets. The Moon is a heavily-cratered rocky planetary body with a crust, mantle, and core in varying proportions as similar to the Earth (Heiken et al., 1991). In fact, the surface of the Moon is exposed to the harsh environment of the outer space due to the absence of dense atmosphere or significant magnetic field. This makes it vulnerable to various forms of weathering processes. The implication of this is in grinding up the surface rocks into a chaotic upper layer of powdery debris called the regolith (Keller & Mckay, 1997). The continuous bombardment of space weathering agents, such as meteorites/micro-meteorites, solar wind, and galactic cosmic rays, excavates the underlying fractured bedrock and gardens the upper regolith while exposing some of the fresh bedrock in the regions having steep-sided slopes. A conceptual diagram representing the interaction of the aforementioned agents with the lunar regolith is displayed in Figure 1. However, the evolution of the regolith follows at a slow rate as the geomorphological entities on the Moon erode about a centimeter in every 20 million years (Horz et al., 1991). Moreover, this phenomenon has been found to be correlated with the effects of space weathering on the lunar soil (Pieters & Noble, 2016).

The immediate cause of space weathering on the regolith grains primarily includes comminution, melting, sputtering and vaporization. This further makes it difficult for the remote sensing data interpretation as the characteristics of the weathered soil behaves differently under the influence of EM wave (Keller & Mckay, 1997; Noble, 2004; Pieters & Noble, 2016). Therefore, the study of space weathering processes forms an integrated part in the planetary remote sensing for characterizing the surfaces. From the lunar viewpoint, one of the major products of space weathering is the glass welded aggregates (agglutinates) of surrounding glass and mineral fragments formed during the melting of that portion of soil (Keller & Mckay, 1997). This makes the regolith appear dark in the reflectance spectroscopy due to the enrichment of nanophase iron, which is ubiquitous in the rims and agglutinated portion of the regolith. The inclusion of such minute blebs of metallic iron attributes to the redeposition of the liberated iron during the vaporization of iron-rich minerals like pyroxene and olivine in its native form (Horz et al., 1991). In addition, the space weathering also produces the surface correlated products in the form of volatile implantation, glass splashes and accretion. The concerned factors contribute to the changes in spectral properties of the lunar soil from a remote sensing perspective, which is threefold. With the regolith more exposed to the space weathering agents, the albedo and mafic absorption band depth decrease with an increase in the spectral slope (Lucey et al., 2006). This further implies toward the darkening and reddening of the surface largely due to the creation of nanophase iron in the agglutinated rims. However, the emerging research focus lies in examining the nature of weathered grains that can retain the implanted volatiles, as potential in-situ resources, originating from incoming solar wind plasma.

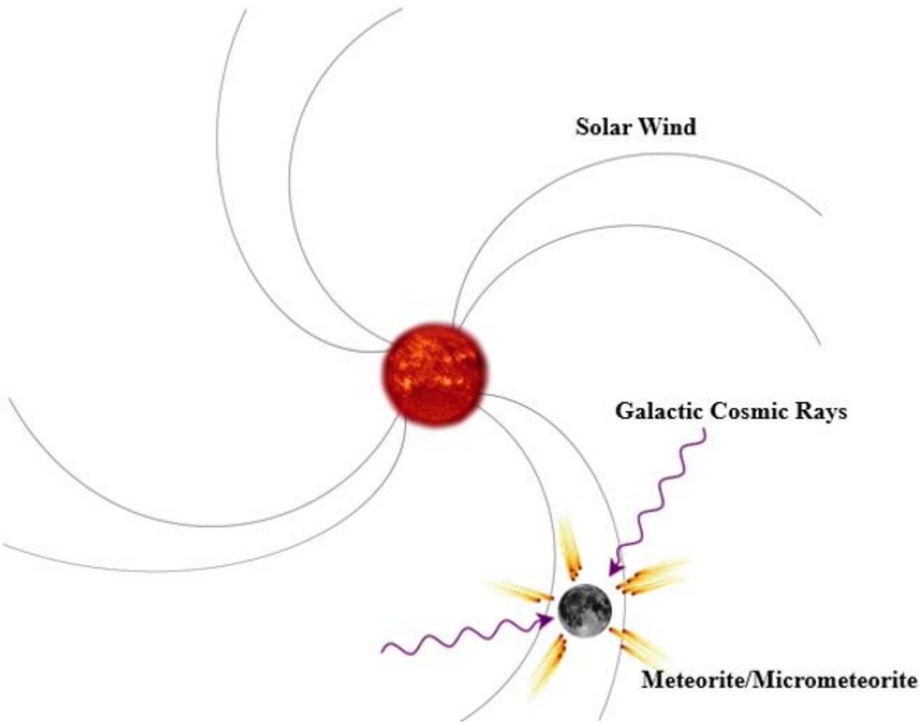

Figure 1: Space weathering agents, in the form of ionized radiations and meteorite bombardments, influencing the physical and optical properties of the Moon.

1.3. Importance of Solar Wind Implanted ^{3}He

One of the space weathering agents that significantly influences the regolith of the planetary bodies is the solar wind. The Sun immerses the Moon in a constant flux of solar wind particles. Moreover, the interaction of solar wind with the local planetary surface provides an insight into the implantation scenario of highly energized charged particles. Such emanation tends to maintain the heliosphere against the compressive pressure of the interstellar medium, thereby continuously contributing to the evolving dynamics of the solar system (Halekas et al., 2005; Lue et al., 2011; Stern, 1999). Compositionally, the solar wind is a stream of charged particle ions with enhanced proton population and trace heavy elements like O^{7+}, C, ^{3}He, etc. (Farrell et al., 2015). These ions governed by high temperature variations along with magnetic field lines flow outward from the solar corona, wherein the gravity is insufficient to hold the rapidly moving particles. Hence, the combination of hot ionized particles and associated magnetic field sectors is called plasma (Cladis et al., 1994; Farrell et al., 2012). The emergence of this plasma phenomenon is aligned with the theory of twisted magnetic flux ropes which states the uneven rotation of magnetic field, thereby resulting in the exposure of plasma to the outer space once the magnetic field breaks (Wang et al., 2017). The solar wind originating from such anomalies is classified as fast wind, with temperatures reaching up to 5 million K, while a much slower wind arises from the coronal steamer belt around the equator (Winske et al., 1985). Importantly, the behaviour of the solar wind upon interacting with either the surface, in case of airless bodies or the magnetosphere of a planet, changes with respect to the media.

The Moon behaves as a solid dielectric obstacle to the solar wind. When the solar wind plasma interacts with the lunar surface, two events occur- the magnetic field lines pass through the Moon, and the hot ionized particles impact the surface, thereby burying themselves into the regolith grains (Halekas et al., 2005; Zimmerman et al., 2011). Due to this, a particle void is created behind the Moon. The ions implanted into the surface layers of lunar grains are overwhelmingly protons, but ionized nuclei of various heavy elements are also included. One such element is ^3He that could be utilized as a fusion fuel for providing clean energy without any radioactive wastes, contrary to the case of uranium fission based terrestrial nuclear reactors (Heiken et al., 1991; Santarius et al., 2006; Santarius, 2004). Consequently, on the Earth, ^3He occurs as a primordial nuclide escaping from the crust to the atmosphere and outer space for millions of years (Santarius, 2004). Apart from this source, it has also been established that only 15 kg of ^3He is produced annually during the maintenance of nuclear weapons (Heiken et al., 1991). This amount is insufficient for yielding enough energy in a dedicated nuclear fusion reactor. However, the Moon has been subjected to a large quantile bombardment of ^3He by the solar wind since its origin. Eventually, up to ~20 ppb (by weight) of ^3He have been implanted in some of the lunar soils, making them suitable candidates for future lunar mining operations (Fa & Jin, 2007; Fa & Jin, 2010; Johnson et al., 1999).

The concentration of ^3He in the lunar regolith at a given location is mainly governed by two factors- the amount of ^3He implanted by the solar wind supply, and efficient retention of the implanted ^3He (Fa & Jin, 2007; Johnson et al., 1999). The impact of the solar wind depends on the latitude and longitude of the lunar geomorphological units. This can be further demonstrated by a theoretical solar wind fluence model, which takes into account the period when the Moon is in the Earth's magnetotail (Johnson et al., 1999). The retention scenario of solar wind implanted ^3He is quantitatively described by the abundance of electro-conductive mineral and maturity of the soil. The degree to which the regolith accumulates the physical and chemical changes resulting from the continuous exposure of the space weathering agents is measured in terms of maturity. Moreover, the quantification of this parameter based on the spectral reflectance measurements is known as optical maturity (Lucey et al., 2000). The challenges concerned with remote observations involve the validity of the estimated variable due to insufficient ground data. However, the returned samples show the variations in the optical maturity to correlate well with other maturity parameters like agglutination, Is/FeO, etc. (Lucey et al., 2000). The more mature regolith attributes to a finer crystalline structure of the grains as compared to that of the coarsely grained immature soil. The former results in a relatively increased surface area with respect to total volumetric regolith weight, thereby accumulating higher concentrations of ^3He. The second parameter is the ilmenite abundance, which is a highly electro-conductive mineral. Under the influence of solar wind, this mineral retains its original crystal structure while other rock minerals become amorphous. Thus, ilmenite-rich deposits are capable of retaining more ^3He. TiO_2 serves as a good tracer for determining the quantitative aspects of ilmenite abundance (Kumar & Kumar, 2014; Lucey et al., 1995; Lucey et al., 2000; Lucey et al., 1998; Shukla et al., 2017; Taylor et al., 2001). It is observed that the ^3He content shows a high correlation with the product of maturation and ilmenite abundance for the Apollo samples and hence, can be retained more over a highly mature and ilmenite-rich lunar grain (Conway, 1988; Jordan, 1990). However, it takes nearly thousand years for outgassing the retained ^3He by a lunar grain (Poupeau et al., 1978).

1.4. Problem Statement

Several research activities have been carried out in retrieving the ^3He abundance by incorporating the solar wind fluence and optical properties of the regolith in conjunction with the Clementine UVVIS and Apollo landing site data (Abdrakhimov & Galimov, 2007; Fa & Jin, 2007; Heiken et al., 1991; Johnson et al., 1999). Contrary to the maturation of the regolith, the physical properties of the lunar grains are also governed by the impact of solar wind plasma. This includes the geotechnical characterization of the soil by considering the mechanical stability of the rocks in terms of porosity, void ratio, bulk density and relative density. The former two could, in fact, prove their potential towards understanding the retention of solar wind gases based on the presence of void spaces between the soil grains. Subsequently, the latter describes the compaction of the soil, whether it is loosely packed or tightly grained, attributing to the penetrating capabilities of the solar wind. The physical properties also incorporate the electrical parameters of the soil, like complex dielectric constant and loss tangent, which explains the degree of attenuation of EM wave, when interacted with the regolith. This describes the response of lunar soil materials towards electrical current flow and influence of electromagnetic energy in propagating within the soil (Horz et al., 1991). Hence, the net effect of electrical and geotechnical properties on the regolith grains for understanding an efficient ^{3}He retention is an important factor to consider.

The mapping of the physical properties of the lunar surface has been well demonstrated by utilizing the potential of Radar astronomy (Horz et al., 1991). Evidently, the bistatic radar imaging of the Moon, by the Lunar Reconnaissance Orbiter (LRO) and Earth-based Arecibo Observatory, has provided new insights into exploring coherent backscattering opposition effect that has not been observed in the monostatic campaign (Patterson et al., 2017; Wahl et al., 2012). According to the effect, the most important factor for determining the probable regions of water-ice and dark mantle deposits has been substantially overestimated in the monostatic observations (Patterson et al., 2017). However, the behaviour of the physical properties of the regolith towards varying local bistatic angle has not been explored yet. Additionally, the Chandrayaan–1 Moon Mineralogy Mapper (M^3) proves to be effective in producing high spectral/spatial resolution abundance and maturity maps with its wider spectral coverage as compared to that of the Clementine UVVIS camera (Pieters et al., 2009). Thus, the M^3 data could be utilized for investigating the spectral behaviour of the regolith so as to improve the previously generated low-resolution ^{3}He retained maps. Instead of adopting and recalibrating the hypothetical origin for maturity measurements specific to M^3 data, a spectral parametric approach could be envisaged through integrating the contribution of space weathering associated with the ^{3}He retention. This offers a significant perspective of the regolith towards establishing a capture mechanism for solar wind implanted ^{3}He by employing M^3 spectroscopy.

The lunar topography is not well associated with the overall repository of ^{3}He, thereby resulting in the lack of knowledge concerning the directional spread of the ^{3}He with respect to depth. The importance of the directional component provides potential abundant sources of ^{3}He, wherein the future mining operations could be efficiently performed without any volatile loss. The present work contributes to a deeper understanding of the physics behind the retention scenario of solar wind implanted ^{3}He into the lunar soil grains. The study determines the spatial orientation of the future ^{3}He mining reserves while considering the topographical and geotechnical characteristics of the surface. This also includes developing a spectral parameter based quantitative ^{3}He retention model by evaluating the effects of space weathering. Additionally, the petrophysical properties of the regolith are incorporated in conjunction with the global inventory of future lunar ^{3}He mining sites. The research intends to develop a methodology for analyzing the dual frequency SAR and Imaging Infrared Spectrometer data of the ISRO Chandrayaan – 2 mission. Furthermore, the future scope of the study may utilize the solar wind variability for modelling the solar wind fluence more accurately from the recently launched NASA Parker Solar Probe measurements.

1.5. Research Identification

The overall focus of this research is to develop a remote sensing based framework for revisiting the science behind the retention scenario of the lunar ^{3}He, assess the potential of bistatic miniature radar in characterizing the physical properties of the regolith and incorporate a spatial component by determining the orientation of the ^{3}He with respect to depth, thereby proving significant for future mining strategies.

1.5.1. Research Objectives

To investigate the characterization of the solar wind implanted ^{3}He in conjunction with the individual space weathering processes and petrophysical indicators of the lunar regolith.

Specific Objectives are:

1. To explore the role of local incidence angle on quantifying the distribution of normalized solar wind plasma over the surface.
2. To evaluate the spectral effects of space weathering on lunar soil in developing a hybrid quantitative model of lunar ^{3}He.
3. To examine the potential of the LRO Bistatic Miniature Radar data for retrieving the electrical and geotechnical characteristics of the regolith.
4. To analyze the retention mechanism of solar wind ^{3}He based on petrophysical properties of the lunar soil.

1.5.2. Research Questions

For the fulfilment of objectives, the present study aims at answering the following questions:

1. Specific Objective 1:
   a. How do the variations in topography affect the distribution of incoming solar wind plasma onto the surface?
   b. What are the theoretical constraints to be considered for solar wind fluence model?
2. Specific Objective 2:
   a. What are the spectral parameters associated with the quantification of optical maturation?
   b. How can the local maturity trends and soil chemistry be compared in conjunction with ^{3}He retention?
   c. How is the orientation of the solar wind ^{3}He with respect to the directional component?
3. Specific Objective 3:
   a. How is the sensitivity of the radar backscatter towards surface parameters, incidence angle and polarization?
   b. What are the physical models for retrieving the dielectric and geotechnical properties of the regolith?
4. Specific Objective 4:
   a. What is the influence of the physical characteristics on the retained ^{3}He?
   b. What are the implications of the bistatic angle on the solar wind ^{3}He abundance?

1.5.3. Innovation Aimed At

The novelty of the research is to develop a hybrid retention model for quantifying the solar wind ^{3}He of the regional lunar soils while considering the effects of space weathering. The work investigates to improve the solar wind fluence model by accounting the influence of local topography. The research also attempts to incorporate a spatial component of the directionally oriented solar wind implanted ^{3}He along with physical and topographical properties of the lunar regolith. Furthermore, the study explores the physics-based backscattering models in retrieving the petrophysical characteristics of the lunar soil.

1.6. Thesis Outline

This thesis is divided into six chapters. Chapter 1 provides an introduction to lunar science paradigm. Chapter 2 deals with detailed theoretical concepts relevant to the research goals. In Chapter 3 and Chapter 4, study area, datasets and methodological framework are put forward. Finally, Chapter 5 presents the obtained results and relevant analysis followed by the conclusive remarks in Chapter 6.

2. LITERATURE REVIEW

The intention of this chapter is to provide a theoretical and technical background of the sources of ^{3}He whilst focussing on the solar wind plasma as the potential ^{3}He carrier, to envisage the retention hypothesis during the plasma interaction with lunar regolith, to briefly outline the remote sensing based surface characterization essential for retention modelling with a major focus on spectroscopy and radar, to facilitate a framework for the theoretical modelling of the incoming solar wind distribution, and finally to review some of the recent lunar studies on the plasma interaction physics.

2.1. Evolution of ^{3}He in the Solar System

The availability of ^{3}He is enormous in space, however, the mechanism of trapping it back to the Earth is limited. This leads to exploring alternative sources within the Earth's vicinity for an overall establishment of future energy goals through ^{3}He fusion (Kulcinski & Schmitt, 1988). Compositionally, ^{3}He can be regarded as light and non-radioactive isotope of Helium with one neutron and two protons. The utilization of ^{3}He atoms in the nuclear fusion reaction furnishes a large amount of energy without making the surrounding environment radioactive (Wittenberg et al., 1991). This remains a quest among scientific researchers to understand the existing repositories of ^{3}He in the solar system and develop the state of the art technologies for performing remote mining operations.

2.1.1. Terrestrial Sources

The abundance of Helium and its stable isotope ^{3}He, on the Earth, is a rarity. Upon reaching the atmosphere, it escapes the terrestrial gravity on a timescale of ~10^6 years. In contrast with the age of the Earth, this span is very short. Therefore, the availability of ^{3}He arises either from the mantle derived primordial deposition, or through initiated nuclear reactions in the upper atmosphere due to the collision of galactic cosmic rays and solar wind with the magnetosphere. The overall terrestrial ^{3}He budget attributes to a steady state between the incoming ^{3}He fluxes from the Earth, extraterrestrial contribution and ^{3}He escaping to the outer space. In essence, the entire ^{3}He repository in the terrestrial atmosphere accounts for about 5000 tons which is less than 1 part in 10^{12} of the total atmosphere by mass (Kulcinski & Schmitt, 1988; Swindle et al., 1990). The retrieval of the ^{3}He content, hence, is evidently infeasible for terrestrial environments. Moreover, the fluence of ^{3}He ions into the atmosphere is estimated to be ~10 kg per annum, with the majority of that proportion originating from mid-oceanic ridges and auroral precipitation (Ozima & Podosek, 1983). Owing to this, the subduction of the denser oceanic plate below the continental plate serves as a probe into the mantle, thereby exposing the potentially rich zones of ^{3}He (Wittenberg et al., 1991). However, due to the increased temperature and accretion, the volatile materials including ^{3}He vaporizes to escape from the terrestrial atmosphere. In addition, some of the ^{3}He contents are evolved due to the emitted neutrons during the spontaneous fission reaction of ^{235}U with ^{6}Li in the soil (Ozima & Podosek, 1983). By considering the contribution of tritium decay during the maintenance of thermonuclear weapons and mining activities of the United States natural gas reserves, the total available ^{3}He repository could be assumed to be more than the currently estimated quantity (20 kg/year) (Kulcinski & Schmitt, 1988). Nevertheless, at the suggested one ton per annum level, this supply is insufficient to provide service to the desired nuclear fusion operations.

2.1.2. Solar Wind Plasma

In the solar system, one of the enormous reserves of ^{3}He resides in the Sun itself. Quantitatively, the estimated ^{4}He isotope in the Sun is produced during the nuclear fusion of hydrogen nuclei into helium and constitutes about 24% of the total solar composition by weight (Kulcinski & Schmitt, 1988;

Wittenberg et al., 1991). Furthermore, the ratio of ^{3}He to ^{4}He is considered to be ~4 × 10^{-4}, suggestive of the total ^{3}He repository of ~70 ppm (1.4 × 10^{29} g, about 24 times the mass of the Earth) (Swindle, 1992). The fetching of the ^{3}He fuel from installing devices near the Sun is beyond present-day technological limits. However, the recently launched NASA Parker Solar Probe initiates the effort of establishing the closest approach, until now in the history of mankind, to the Sun (Garner, 2017). In order to facilitate the ^{3}He supply, the Sun releases a steady flow of hot particles from its upper atmosphere as solar wind plasma. The flux contains 0.005 g of ^{3}He per km^2 per annum at a distance of 1 AU and decreases with inverse square distance of the plasma from the Sun.

The airless and non-magnetized bodies, like Moon and asteroids, enable the incoming solar plasma to interact with the surface, thereby implanting into retentive mineral grains. As compared to the asteroids, the Moon is an ideal candidate for carrying out in-situ ^{3}He exploration due to its relatively bigger size and closer vicinity to the Sun. Moreover, the ^{3}He abundance, in the case of non-lunar meteorite, is lower than 5% of that in the Apollo 11 lunar soils (Wittenberg et al., 1991). Evidently, the orbit of the Moon intercepts the solar wind 30 times more than the 27 largest asteroids combined (Housen et al., 1979; Swindle et al., 1990). In addition, some of the Earth-approaching asteroids with orbits relatively closer to the Sun might have more considerable deposition of ^{3}He as compared to the Moon. However, there is a lesser number of approaching asteroids to the Earth, which have the diameter even not 1% of the total lunar diameter. This directly implies that the surface area is of the order 10^4 smaller than that of the Moon, thereby resulting in the least retention within few meters depth of asteroid's regolith depending on the model simulations (Housen et al., 1979).

The Earth's magnetic field deflects the incoming solar wind fluence, resulting in the negligible concentrations of ^{3}He. Similarly, none of the typical planets owing to the presence of atmosphere or magnetic field or both receive much of the ^{3}He from the solar wind. However, a disparity arises in the case of Mercury, which has no atmosphere, insignificant magnetic field and closer proximity to the Sun. In this context, the Mercurian surface might retain a comparable amount of ^{3}He as that of the lunar regolith (Hood & Williams, 1989). Yet, as of now, no effective mining logistics for Mercury exist, thereby highlighting the importance of lunar in-situ resource utilization technologies.

2.1.3. Atmospheres of the Outer Gas Giants

An alternative source of ^{3}He inheres within the atmospheres of outer, gas giant planets. With the compositions similar to that of the Sun, a Jovian atmosphere contains much higher ^{3}He content than the other planetary systems (Conrath et al., 1987). For instance, if 1 bar level of the atmosphere is examined, then a box of 684 m side encompasses 1 ton of ^{3}He (Swindle et al., 1990). In principle, the total content of ^{3}He that the Jupiter holds is ~10^{26} g while assuming the atmosphere to be suggestive of the entire planet, thereby surpassing the upper limit of the lunar inventory by 10^{14} times. Essentially, the lunar mining operations for ^{3}He can contribute towards fulfilling the energy demands of the Earth for a decade. This attributes to the need of long term supply through extracting from the outer planets like Jupiter, Saturn and Uranus. Although the surplus quantity of ^{3}He comes from these regions of the solar system, there exist obvious difficulties in exploring such outer atmospheres. These include longer expedition period, stronger gravitational influence, and absence of solid surface. Ultimately, it may be an excellent opportunity to consider for future mining activities provided adequate technology and lack of dependency on lunar ^{3}He (Swindle et al., 1990). The selection of the best possible candidate for this operation is still under process. Situated in the nearby vicinity comparing to other outer planets from the Earth, Jupiter proves to be a reliable source as it contains an immense amount of ^{3}He by weight. But the limitation arises in the technology lag as the stronger gravity field would not virtually allow the scientific instruments to escape. On the contrary, much less escape velocity is observed in the case of Saturn with nearly half of that in Jupiter. However, the lower abundance of ^{3}He in its atmosphere and distant proximity restricts the scope of mining (Swindle et al., 1990). The successful mission of Cassini, dedicated to observing Saturn, shows the potential of future long-run and sustainable spaceflight missions (Greicius, 2015). Apart from this, Uranus facilitates an even more intriguing statistics in terms of ^{3}He concentration close to that of the Jupiter and escape velocity of 40% lower than that of the Saturn (Conrath et al., 1987). Hence, considering the prospective mining options at the Uranus, a possible travel distance of 20 AU from the Earth could be substantially beneficial for future energy prospects.

2.2. Understanding the Lunar ^{3}He Retention Scenario

Among all the possible sources of ^{3}He, the Moon serves as a keystone of concentrating the solar wind plasma depending on the retentive characteristics of the regolith. This provides new insights into in-situ resource utilization schemes essential for a potential human outpost. Prior to exploring lunar mining strategies, the retention framework of the solar wind ^{3}He is required to be critically examined by employing the measurements from returned Apollo and Luna samples. This will improve the understanding of the regolith properties responsible for trapping the loose ^{3}He ions into the grains.

2.2.1. Effect of Grain Size

The implantation of ^{3}He in lunar soil is mainly associated with the interaction of low energy solar wind. This attributes to lower penetration capabilities, thereby attenuating the ^{3}He concentration with increasing distance from the surface of grains. As demonstrated in Figure 2, the evaluation of the Apollo and Luna samples suggests an inverse correlation of ^{3}He abundance with grain size. Several studies on surficial etching and laser induced extraction of gases reveal the surface correlated nature of ^{3}He with deposition up to 0.2 microns of the outermost layer (Eberhardt et al., 1970; Kiko et al., 1978; Swindle et al., 1990). This exhibits strong agreement with terrestrial mining techniques.

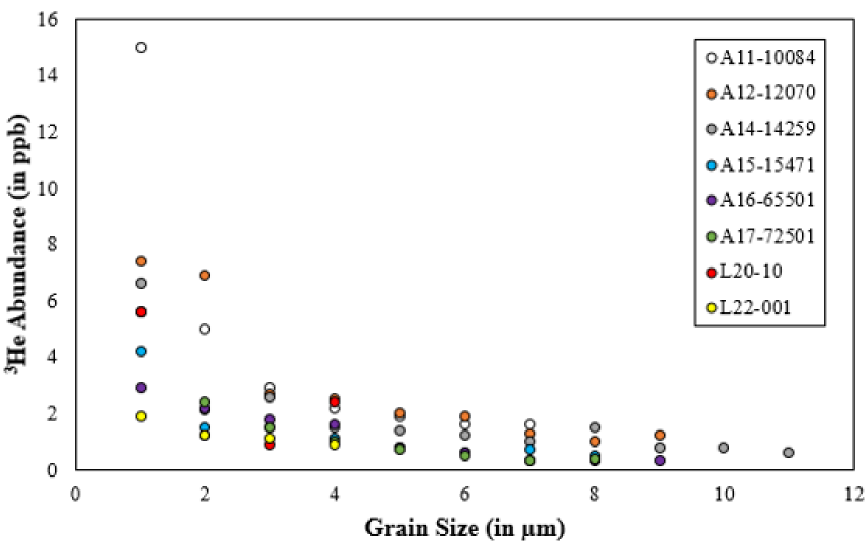

Figure 2: The variability of ^{3}He content with respect to the grain size of several returned samples from the Apollo and Luna missions. Note the overall decreasing exponential trend with the increase in the size, thereby reflecting efficient retention by a mature regolith.

The dependence of grain size on the solar wind implanted ^{3}He is twofold. First, the production of richer ^{3}He sample through assessing the grain size of the soil (sieving), suggestive of mining finest fraction of the lunar regolith (Cameron, 1987; Kulcinski & Schmitt, 1988). This evaluates the retention of ^{3}He into different sized grains depending on the influence of space weathering. According to this, the most mature regolith of grain sizes less than 50 μ accommodates about 80% of the total ^{3}He. Swindle et al. (1990) suggested the possible dissipation of three-fifth fraction of the ^{3}He throughout the sieving operation. The beneficiation from grain size sorting highly depends on the suitability of the mining scheme. Second, there could be more than one extraction technique through simple heating of either solar or microwave source (Kulcinski & Schmitt, 1988; Meek et al., 1985). The ^{3}He mining from regolith grains by abrasion or acid etching of the grain surfaces could also be considered. In essence, the higher surface area to volumetric ratio attributes to an increased ^{3}He deposition into the finer and crystalline grains. The retentiveness of the grains towards solar wind fluence is also governed by geotechnical properties of the regolith like porosity, bulk density and the void ratio (Horz et al., 1991). This provides a newer dimension with respect to minute granular voids which may hold the solar wind gases physically depending on the compaction of the regolith. Moreover, the remote observations enable the estimation of these parameters by assessing the in-situ bulk repositories of Apollo and Luna samples (Horz et al., 1991). However, the evaluation of space weathering processes would further expand the research scope of the regolith evolution in conjunction with the adopted ^{3}He mining framework.

2.2.2. Influence of Regolith Depth on the ^{3}He Distribution

The gardening of the regolith from several depths by continuous meteorite/micrometeorite impacts results in the comminution, melting and stirring of surface materials. This distributes the implanted ^{3}He to a depth of several meters, even though the retention occurs only in the upper micron layer (Horz et al., 1991). The outcome of any bombardment varies largely depending on the size and velocity of the projectile. Moreover, the type of the target (i.e. regolith or bedrock) also plays an important role in defining the aftermath of impact collision. The excavation of lunar basins led by large-sized impactors increases the depth of the regolith while smaller impacts stir the incoherent and broken rock fragments. Owing to this stochastic impact cratering process, the variation in the regolith is substantial for different regions and depths. The surficial implantation of ^{3}He mixed with regolith at depths is observed clearly in the returned Apollo and Luna samples along with regional variability. According to Swindle et al. (1990), the probable exposure of a given grain on the surface attenuates with depth, thereby reducing the concentration of ^{3}He. A study on regolith evolution further demonstrates this through Monte Carlo model, wherein the grains at a depth of 2 to 4 m possess a higher mean density of radiation damage trails than that of the surficial grains within 30 cm by 36% (Arnold, 1975). Moreover, the employment of deepest drill cores in the Apollo 15, 16 and 17 missions exhibits similar results, thereby affirming the aforementioned model outcomes. This also presents randomness in the variations of ^{3}He content with respect to a systematic decrease in depth. Based on this, Swindle et al. (1990) estimated the distribution of ^{3}He by assuming two different conditions. The first assumption derives the upper limit by taking the constant concentration of ^{3}He while the lower limit assumes the exponential decay of the surficial ^{3}He concentration (C_0 in ppb) with depth (z in m), as $C_0 \exp(-0.347z)$. This leads to a reduction in the ^{3}He abundance by a factor of two in every two meters.

The validation for such distributions can, however, not be performed for regolith depths as the Apollo drill core goes up to 3 m. Several techniques have been utilized for determining the approximate estimates of the total depth through either crater morphological measures or available data of performed seismic experiments at the Apollo landing sites (Oberbeck & Quaide, 1967; Quaide & Oberbeck, 1968; Slyuta et al., 2007; Swindle, 1992). The typical thickness of dark, low lying basaltic floodplains (Mare) is found to be ~5 m while the high albedo rugged terrains (highlands) exhibit a comparatively thicker regolith (Swindle, 1992; Swindle et al., 1990). Moreover, the crater morphological estimates suggest a variability ranging from less than 1 m to greater than 10 m for sampled sites. These approaches offer a localised viewpoint, thereby requiring the need for satellite remote sensing data for a quantitative retrieval of global regolith thickness. The deposition of ^{3}He is likely to follow a declining trend with depth. However, there are some contradictory sites, wherein deeper regolith accommodates higher ^{3}He abundance than the typical surface concentrations. Evidently, the samples from the Apollo 17 drill core display such opposing characteristics (Kulcinski & Schmitt, 1988). A more detailed understanding of the contribution of space weathering agents on the regolith dynamics could provide new insights into this anomaly. From a mining perspective, any strategy that follows a uniform excavation of the regolith is likely to either reduce much of the ^{3}He concentration or experience inoperable condition of the excavator in the regions with larger rock accumulation nearer to the regolith.

2.2.3. Locational Variability of the ^{3}He Abundant Soil

The profusion of ^{3}He in the lunar regolith is mainly governed by two factors: the amount of incoming solar wind ^{3}He and the retentive agents responsible for its implantation. This overviews the contribution of space weathering agents on geochemical characteristics of the lunar material for assessing the bulk repository of ^{3}He. The remote observations for both of these parameters are well established as part of developing a retention model based on the locational variables.

2.2.3.1. Compositional Variations

The solar wind implanted ^{3}He into regolith grains diffuses at a rate that is strongly dependent on surface exposed minerals. Among all the lunar minerals, ilmenite furnishes a strong retentive behaviour towards ^{3}He. One of the studies shows the enhancement of ^{3}He concentrations in lunar ilmenite crystal as compared to olivine, pyroxene and plagioclase (Swindle et al., 1990; Taylor, 1994). Although the regolith grain is of the same size from the same soil, the percentage of solar wind gases is found to be comparable for all minerals, in case of Argon. Significantly, the proportion of the ^{3}He in the ilmenite mineral has a sharp incremental trend of 10 to 100 times as compared to other minerals (Taylor, 1994). It is also observed that most of the titanium enrichments come from ilmenite, thereby proving it to be a good indicator of ^{3}He. Apart from this, the higher profusion of Ti and ^{3}He in the agglutinitic glasses is suggestive of the inclusion of ilmenite mineral fragments. Figure 3 suggests a linear relationship between ^{3}He and Ti content, with 1 wt% TiO_2 containing approximately 1 ppb of ^{3}He. All these measurements are acquired from the in-situ analysis of returned Apollo and Luna samples (Taylor, 1994).

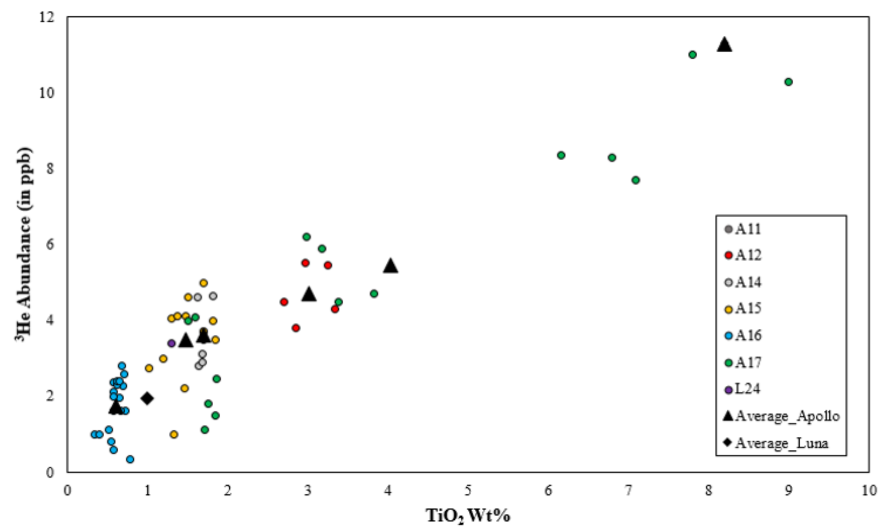

Figure 3: The relationship of the measured ^{3}He as a function of Ti content for all the lunar soils where both the estimates are available. The averages of the individual landing site are also illustrated.

The proportion of Ti content in the lunar soil can be estimated through remote observations of either gamma-ray spectrometers on board Apollo orbiters or ground-based telescopic instruments. Moreover, the outcomes of the techniques mentioned above fall within the computed statistical uncertainties (Metzger et al., 1979). The abundance of Ti in the Mare regions is higher than that of the highlands, thereby averaging to 3.7 and 1.6 wt% TiO_2 respectively (Davis, 1980). However, there are some localised deposits with enhanced Ti proportions in the regions of Mare Tranquillitatis, Oceanus Procellarum, and Aristarchus Plateau. Hence, these lunar locations are preferably considered for performing large scale ^3He mining operations. It should be noted that the refinement in the ^3He extraction framework by separating ilmenite from regolith is unrealistic in the current state of technology due to the rarity of single lunar ilmenite grain (Heiken & Vaniman, 1990). This further provides the initial criteria for adopting suitable mining scheme without any of the major loss in the retrieval of ^3He.

2.2.3.2. Local Maturation

The retention scenario of the solar wind ^3He is influenced by the variations caused due to the amount of time the grain is exposed to the space environment, termed as maturation. Such exposure attributes to the production of agglutinates, radiation damage tracks from highly charged particles, nanophase iron and comminution of grains, alongside implantation of solar wind species. Interestingly, all the effects tend to correlate with each other. In order to quantify this relation, Morris (1976) examined the lunar samples for determining the ratio of reduced metallic iron to oxidized iron (Is/FeO) through ferromagnetic resonance theory. Thus, the reliable estimation of maturity is provided as the ratio is unaffected by the saturation effect (Morris, 1976, 1978). One of the important parameters observable by means of remote sensing techniques is the agglutinate abundance, which alters the spectral characteristics of the soil (Charette et al., 1976). However, the saturation is inherently induced in the spectra with no dependency on soil composition. The agglutination is a product of micrometeorite impact, which contradicts the surface correlated products as ^3He and H are implanted through solar wind fluence. Hence, there is a need for characterizing space weathering events to assess large scale variations in the regolith grains. This can also be demonstrated by correlating the in-situ ^3He with the product of Is/FeO and Ti content, which is illustrated in Figure 4.

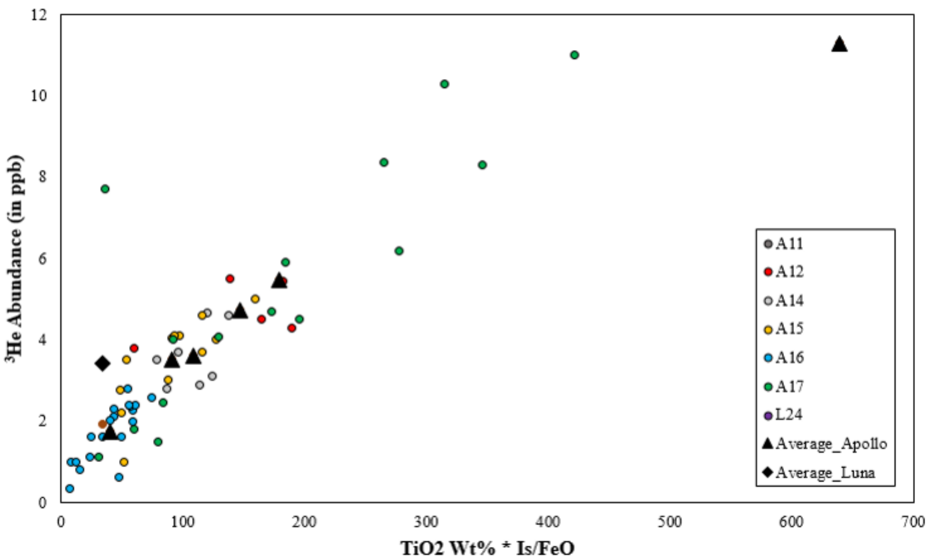

Figure 4: The observed variability trend of retained ^3He with the combined properties of Ti content and maturity (Is/FeO) for all the soils where the estimates are available. Note that the scatter of the points are less as compared to Figure 3, attributing to an increased correlation.

Most of the local variations in maturity could be mapped by utilizing the remote sensing approaches. This is suggestive of evaluating alterations in the length of exposure time for a given regolith, composed of different sized grains. In essence, the smaller grains (mature) could retain higher amounts of ^{3}He as compared to larger ones (Wittenberg et al., 1991). Since the factors are independently contributing towards retention of solar wind ^{3}He, the combined product could enhance the correlation. This attributes to identify the sites with mature and Ti-rich regolith for subsequent mining of ^{3}He.

2.2.3.3. Solar Wind Fluence

The incident solar wind plasma distribution depends on the location of the lunar site, wherein the higher latitude regions receive lower flux as compared to the equatorial. This can be elucidated, in Figure 1, by the radial flow of solar wind from the Sun, rather following a straight line trajectory to the Moon. The solar magnetic flux twisting defines the spiral structure of the proliferating solar wind ions. These ionic particles interact with the lunar regolith at an approximate angle of 45º (Wittenberg et al., 1991). Moreover, the revolution of the Moon about its ecliptic axis is the same as the rotation around the Earth, thereby exposing any lunar material to the solar wind plasma only half the time. Evidently, the polar regions are expected to exhibit lower affinity towards solar wind interaction due to the higher incidence angle of the flow (Fa & Jin, 2007; Johnson et al., 1999; Slyuta et al., 2007; Swindle, 1992). Additionally, the shielding mechanism of the Moon is governed by the Earth's magnetotail, thereby resulting in a complete blackout against solar wind particle flux for 4 to 8 days per lunar cycle (Johnson et al., 1999; Swindle, 1992; Wittenberg et al., 1991). During this period, a lower amount of solar wind particles are incident on the centre of the lunar near side, which is always in the visual range of the Earth. Subsequently, the regoliths of the lunar farside and limbs have a comparatively higher proportion of solar wind particle enrichment. However, the regolith samples from the Apollo missions come only from a limited selenographic range of the Moon.

One of the significant effects that alter the solar wind composition is the saturation of the lunar grains. It has been concluded that it takes around ten years for grain in free space to saturate under direct solar wind exposure (Futagami et al., 1990). This corresponds to an unshielded exposure of nearly a few decades on the Moon. The enhanced saturation of ^{3}He in the lunar samples occurs for a considerable fragment of the grains (Wieler et al., 1980). Furthermore, some of the samples are analyzed to have Argon saturation. However, due to the similarities in the correlation of Argon with C and N, higher abundances seemingly attribute to negligible saturation. In order to capture saturation effects, the volatile abundances need to be compared for the regions having the range of solar wind fluence (Slyuta et al., 2007; Swindle, 1992; Swindle et al., 1990). This implies investigating the samples from the center of the lunar farside with the probable prediction of highest fluence. Ideally, none of the returned samples is from that side, but the locality of the Russian Luna samples in the eastern limb of nearside makes it unique for such analysis. Hence, these are expected to have an estimate of higher solar wind fluence as the average Apollo samples.

Apart from this, another prominent factor that alters the solar wind volatile distribution is ion focussing. The increased crustal magnetic fields in certain lunar sites produce regional mini-magnetospheres, thereby deflecting the incoming solar wind flow (Swindle et al., 1990). Since these regions have larger coverage, there may be areas with virtually no ^{3}He as compared to nearby vicinity with above normal ^{3}He concentrations (Hood & Williams, 1989). The anomalies are further associated with the evolution of enigmatic swirl features, easily identifiable from Earth-based remote observations. In this context, the highly abundant ^{3}He regions within the swirls appear to be promising for future mining operations.

2.3. Advances in Remote Sensing: Lunar Perspective

With the increased utilization of remote sensing practices, the understanding of the present lunar repository through Apollo/Luna samples and lunar meteorites could be broadened into a global context (Dunkin & Heather, 2000). This enables significant comparison of different lunar terrains from nearside and farside in terms of habitability, thereby initiating efforts for potential human outpost prior to space exploration. The improvisation of remote sensing techniques can be done more precisely on an airless lunar platform without any complications of dynamically evolving surface processes (Horz et al., 1991). This provides new insights into testing and calibrating novel remote approaches on the Moon before exploring it for the other active planetary bodies. Even though many instruments have been sent to the lunar surface, a large volume of remote sensing data is often required. This higher demand results in designing sophisticated instruments dedicated to specific operations. In essence, some of the elusive lunar reality that remains a mystery needs to be answered with distinctive sensor characteristics on board remote sensing instruments.

2.3.1. Imaging Spectroscopy

The received insolation by the surface is mainly characterized by reflection and absorption. When the incoming solar radiation interacts with lunar regolith, a significant portion of the light is reflected back to the instrument sensor (Goetz et al., 1985). The intensity measurements of each wavelength of the received radiation are converted into a reflectance spectrum, wherein the diagnostic absorptions of different lunar materials are related (Bellucci & Formisano, 1997). Moreover, the strength of these absorption features exhibits a strong criterion to differentiate the composition of the regolith. As part of validation, the laboratory measurements of known lunar samples are utilized to characterize the surficial presence of absorption signatures in remotely sensed data (Dunkin & Heather, 2000; Taylor, 1982). Quantitatively, the spectroscopic measurements investigate the interaction mechanisms of energy with regolith. The imaging term further attributes to the data specific quality of each pixel corresponding to a spectrum of energy for signature information retrieval.

The extensive utilization of planetary spectroscopy in the 1970s has revolutionized the quest for remotely examining the geophysical characteristics of the Moon. This further involved telescopes for acquiring the compositional reflectance signatures from the nearside. The analytical aspects of this data resulted in the accurate estimation of specific mafic mineral abundances (like olivine and pyroxene) across the surface (Bellucci & Formisano, 1997; Dunkin & Heather, 2000). Moreover, the telescopic reflectance data provided large scale variations in the geochemical properties between different features like large impact basins and pyroclastic depositions. In essence, these observations have facilitated the scientific community with a general compositional perspective of the crust and lunar mare far away from the Apollo/Luna sampling sites. Subsequently, the spectroscopic datasets of the lunar farside have been captured, for the first time, by the Galileo spacecraft in 1990 and 1992 Earth-Moon flybys (NASA STI, 1992). Although the majority of the data came from the western hemisphere, significant research activities were conducted in retrieving the chemical composition for the other half. Following this, a dedicated lunar mission of Clementine was launched in 1994 for promoting the use of spectroscopic data (Isbell et al., 1999). The returned lunar samples have been analyzed to unravel the absorptions of common minerals upon which the filter design of the cameras was based. The Clementine data have displayed better spatial resolution in contrast to the telescopic data for mapping small-scale compositional differences of the regolith (Eliason et al., 1999). However, the absence of wide spectrum filters has increased the dependence on other telescopic data for reviewing the detailed identification of lunar geologic features. The emergence of the Moon Mineralogy Mapper (M^3) instrument onboard Chandrayaan-1 has solved the criticalities in terms of wider spectral coverage (Pieters et al., 2009). This provides a newer dimension of mapping lunar mineralogy, maturation and geochemical constraints for envisaging the evolution of the Earth-Moon system.

2.3.1.1. Insights into Lunar Maturity Algorithms

The most widely used maturity parameter for assessing the exposure time of a particular lunar feature is OMAT, which aligns well with other indices like Is/FeO, agglutinate abundance, etc. (Lucey et al., 2000). This utilizes the spectral reflectance data of UVVIS camera on board Clementine spacecraft (Lucey et al., 1995). From Figure 5 it is observed that most mature soils tend to appear at the redder (high ratio) and darker end (low reflectance) of the linear trend formed by plotting the in-situ measurements of lunar samples in the Clementine two parameter space. Moreover, the observed trend with varying iron contents converges at a hypothetical hypermature origin (Lucey et al., 1995). This defines an angular iron sensitive parameter, thereby complementing the corresponding maturity measures. Essentially, the algorithm eliminates the association of maturity from the estimates of iron content (Lucey et al., 1998, 1995). It is noteworthy that the observed maturity and iron trends seem mutually perpendicular to each other, as in Figure 5. Hence, the separation of the maturity from the first order compositional differences can be performed by computing the Euclidean distance between the hypermature origin and sample point (Lucey et al., 2000). This presents a quantitative maturity parameter, named as Optical Maturity (OMAT).

$$\mathrm{OMAT} = \sqrt{(R_{750} - x_0)^2 + \left(\left(\frac{R_{950}}{R_{750}}\right) - y_0\right)^2} \tag{2.1}$$

where $(x_0\,, y_0)$ is the origin representing the reflectance and the ratio value respectively and R_λ is the spectral reflectance at λ nm wavelength. The origin is optimized for the Clementine data only and found to be (0.08, 1.19), whilst using the spectral library of the U.S. Geological Survey (USGS) (Eliason et al., 1999; Isbell et al., 1999). However, employing the algorithm for other remotely sensed data involves recalibration of the origin with respect to the corresponding spectral reflectance. Also, the variations in the regional mineralogy are not fully captured by the parameters, thereby introducing uncertainties in the maturity measurements (Clark & McFadden, 2000; Elphic et al., 2000; Staid & Pieters, 2000). For instance, the enrichment of pyroxene and opaque minerals (Fe-spinel and ilmenite) in the Mare soils influences the position of the absolute OMAT index. This also induces the parallel effect in the observed Mare trends rather than the radial pattern of the Lucey maturity model (Staid & Pieters, 2000). In order to compensate the effect, Wilcox et al. (2005) developed a new algorithm for determining optical maturity of the Mare regions (OMAT_m) by rotating the coordinate axis of the Clementine two parameter space, thereby producing an improved indicator of iron content. Following a similar approach, the complementary parameter of FeO attributes to maturity and hence, the equation is given as

$$\mathrm{OMAT}_m = R_{750}\cos\theta - \frac{R_{950}}{R_{750}}\sin\theta \tag{2.2}$$

where θ is the average slope of the mare soil weathering trends (1.3885 rad, for Clementine). According to this, the values range from -1.05 (most mature) to -0.65 (most immature). The applicability of this improved algorithm has not been tested for any sample site, rather derived from intensively verified FeO approach. Instead of solely relying on UVVIS bands, Le Mouélic et al. (2002) employed an alternative method of spectral parameters, i.e. band ratios, for generating iron content maps. This technique is mainly valid for middle to high latitude regions where there are brightness variations due to local topography. Apart from this, the potential of Chandrayaan-1 M^3 data has been assessed by examining the optical maturity trends for regional regoliths (Nettles et al., 2011). This can be qualitatively described in terms of nanophase iron induced spectral effects. Furthermore, the scatterplots of the associated parameters reveal the space weathering trends for crystalline inclusions of ejecta and fresh craters (Nettles et al., 2011). In principle, three spectral parameters are derived representing the impacts of space weathering on lunar soil. The albedo at 1579 nm wavelength depicts the darkening effect while the increasing redness is denoted by the simple ratio of 1508 nm and 703 nm. Moreover, the reducing mafic absorption band depth is a good realisation of integrated band depth at 1000 nm wavelength. In addition, an attempt has been made to include the strength of 2000 nm absorption band parameters for improving the iron estimation algorithm (Bhatt, 2012). This multisensor approach has observed a high correlation of the estimated abundances by integrating 1000 nm and 2000 nm absorption with the laboratory measured values of Apollo/Luna samples. Hence, there is always a scope for improvement of optimizing the maturity algorithm based on available spectroscopic data parameters.

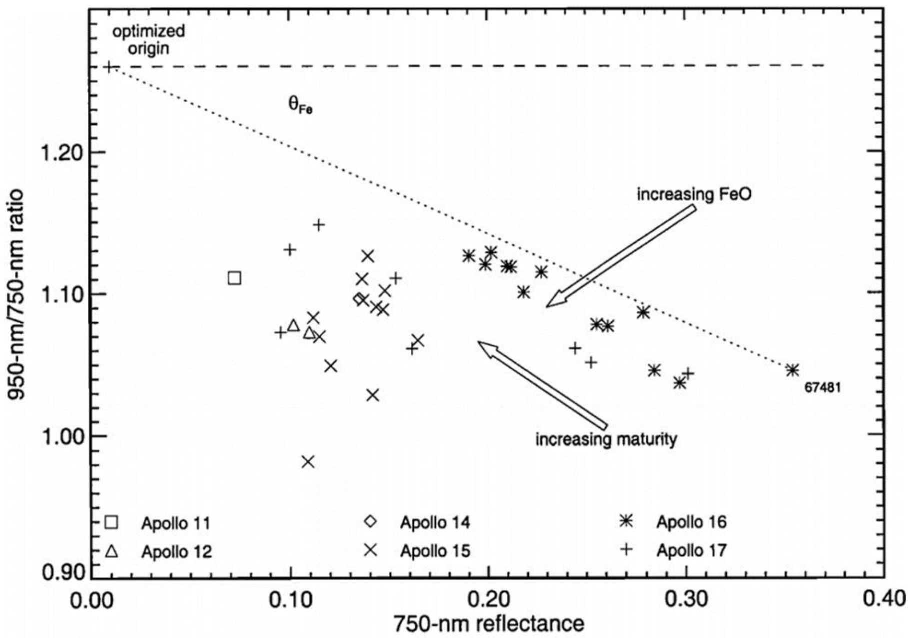

Figure 5: The plot suggestive of hypothetical optimized origin estimates by considering the NIR ratio and reflectance values of the returned Apollo samples from Adams spectral library. The FeO content is strongly aligned with the angular sensitive parameter while the optical maturity increases radially inwards Source: (Lucey et al., 2000).

2.3.1.2. Lunar Ilmenite Abundance Mapping

Ilmenite is one of the most abundant minerals on the Moon, acting as an antecedent to the assessment of prospective lunar base sites. Hence, the spatial distribution of ilmenite across the regolith must be clearly known. Evidently, the concentration of titanium dioxide (TiO_2) in ilmenite is greater than 50 wt%, thereby making ilmenite a dominant source of TiO_2. This implicates the understanding of surface distribution for titanium that can be used as a valuable asset towards mapping potential high ilmenite-rich zones.

The returned lunar samples have been tested for TiO_2 contents by making a comparison with their laboratory measured spectral reflectances (Charette et al., 1974). Moreover, an empirical relationship has been formulated between TiO_2 wt% and the 400-560 nm reflectance slope. It has also been observed that the presence of Fe and Ti absorption features, due to agglutination products, affects the slope. In essence, the applicability of this relation holds only for mature soils. Pieters (1978) utilized the telescopic spectral reflectance data for deriving the correlation of several parameters (band ratio, albedo, band depth) with mare basaltic units. In this, an integrated approach has been adopted for producing TiO_2 and FeO maps. Compared to the earlier method, the absorbing effects of Fe and Ti are obscured from other inclusions like non-opaque glasses for values of less than 4 wt% TiO_2. Furthermore, the "Charette relation" has been refined by introducing a more sensitive parameter, i.e. 400-730 nm slope, to the TiO_2 content (Johnson et al., 1991). With advances in space technology, the multispectral data acquired from Galileo flybys and Clementine UVVIS camera have provided a significant opportunity for investigating the spectral dynamics of the Moon. This has enabled colour visualizations of lunar features by incorporating photometric corrections, which presented new perspectives of Ti-mapping algorithms (Blewett et al., 1997; Lucey et al., 1998). Besides this, an alternative study has been carried out for estimating the relationship between FeO and TiO_2 in order to produce a correlation diagram of the lunar nearside (Shkuratov et al., 1999). In this, the correlation coefficient is observed to be 0.81. Similar to the FeO algorithm, Lucey et al. (2000) have calculated a hypothetical origin in the Clementine two parameter space by considering a low albedo (415 nm) and a high reflectance ratio (415/750 nm) value. Moreover, an angular parameter for Ti has been defined with larger angle values corresponding to the ilmenite proximity. This also has negligible influence from maturity variations. Hence, the presence of an opaque mineral (ilmenite) strongly aligns with the spectral properties in the wavelength region (415-750 nm). The spectral angle θ_{Ti} is defined as

$$\theta_{Ti} = \tan^{-1}\left(\frac{\left(\frac{R_{415}}{R_{750}}\right) - 0.42}{R_{750}}\right) \quad (2.3)$$

where (0.00, 0.42) is the optimized origin, for Clementine UVVIS data, representing UV/VIS ratio and 750 nm albedo values respectively (Lucey et al., 2000). Subsequently, the data have been fitted with the laboratory measured TiO_2 wt% (ω) of the Apollo and Luna samples as

$$\omega = 3.708\theta_{Ti}{}^{5.979} \quad (2.4)$$

The global TiO_2 abundance mapping could, therefore, be performed by using equation (2.4). It has to be noted that this equation is empirical and only valid for Clementine data, thereby requires recalibrating of the optimized origin for other spectral reflectance data. However, Gillis et al. (2003) refined the Lucey algorithm by employing two distinct sets of regression parameters for retrieving accurate TiO_2 contents from regolith. This modification has been made in order to effectively correlate the soil compositions from Apollo/Luna sampling sites with the Clementine data based estimates. Furthermore, the spectral reflectance information from the Chandrayaan-1 M^3 data have mainly employed the recalibration approach of the traditional Lucey algorithm for lunar Ti content retrieval (Shukla et al., 2017; Zhang, 2014; Zhang & Bowles, 2013). Additionally, multiple remote sensing methods have been adopted for extracting the compositional and geophysical properties of the regolith (Bishop, 2011; Staid et al., 2011). This provides new insights into utilizing multisensor integration techniques for unravelling the geological viewpoint of the Moon.

2.3.2. A Brief Overview on Radar Systems

The microwave interactions of the distant astronomical objects have presented a unique exploration strategy in characterizing the physical processes. The sensitivity of the surface/subsurface roughness is attributed to the polarization capabilities of the radar signal. Traditionally, the polarization of an EM wave is determined by the behaviour of the electric field vector in terms of orientation, ellipticity and amplitude (Cloude, 2009). Moreover, these parameters are essential for depicting the scattering variants and directionality of the wave. The transmission and reception of different polarizations provide significant information for designing the radar systems. Since the behaviour of the target governs the polarization of the backscattered echo, more than one polarization is generally induced (Cloude, 2009; Cloude et al., 2012). This results in producing four possible polarization combinations of transmit and receive channels by the radar antennas. In this context, the antenna can only transmit either horizontal or vertical polarization, while receiving different polarizations. A fully polarimetric system has the capability of receiving all the combinations, thereby facilitating maximum backscattering information about the target (Cloude, 2009). Consequently, a dual-polarimetric configuration receives any of the two, while the reception of only one polarization is represented by a single polarimetric system. These can be categorized under compact polarimetry. However, in radar astronomy, the transmission of circularly polarized echo results in a prominent extraction of surface properties by receiving either the same sensed or opposite sensed polarizations.

2.3.2.1. Hybrid Polarimetry

A recently developed concept of compact circular polarimetry is hybrid polarimetry, which offers an improved data acquisition in the radar astronomy. This system produces circular transmit linear receive (CTLR) data with unique self-calibration capabilities and lower susceptibility to cross channel errors (Raney et al., 2011). The advantages over fully polarimetric systems include larger swath width due to reduced pulse repetition frequency, less complexity in terms of system dynamics and decreasing power demands. Essentially, the hybrid polarimetric configuration is highly suited to planetary exploration, thereby contributing to a new radar paradigm. Basically, the transmission of linear polarizations (horizontal and vertical) with a phase difference of $\pi/2$ generates a circular polarized echo, which interacts with the surface (Raney et al., 2011). Furthermore, the polarization is broken depending on the target characteristics, wherein the major portion of the EM wave vibrates in horizontal and vertical directions. In essence, the mutually orthogonal linear backscattered echoes are captured at the receiver end, thereby completing the data acquisition. This choice of architecture has been primarily utilized for lunar radars, i.e. mini-SAR and mini-RF systems. The polarized EM wave can be represented by four Stokes parameters, as in equation (2.5). The importance of these parameters is strongly aligned with an alternative realization of partially polarized waves, along with a fully polarized case (Cloude et al., 2012). Moreover, the angular variables associated with the locus generated by the tip of the electric field vector (polarization ellipse) are related to the parameters as

$$\begin{bmatrix} S_1 \\ S_2 \\ S_3 \\ S_4 \end{bmatrix} = \begin{bmatrix} S_1 \\ S_1 \cos 2\psi \cos 2\chi \\ S_1 \sin 2\psi \cos 2\chi \\ S_1 \sin 2\chi \end{bmatrix} \tag{2.5}$$

where the first term (S_1) corresponds to the total power of the wave and is, indeed, dependent on all other parameters, S_2 outlines the polarizability of the wave, S_3 and S_4 represents the phase information of the wave and (ψ, χ) attributes to the orientation and ellipticity of the polarized wave. The condition that holds for partially polarized wave can be described as

$$S_1^2 = \sum_{i=2}^{4} S_i^2 \tag{2.6}$$

The Stokes parameters are the primary products derived from hybrid polarimetric data, thereby providing better computation and interpretability of the parameters of polarization ellipse through basis invariant approach (Cloude, 2009). However, the response from an entity may exhibit mixed scenarios of scattering mechanisms due to the distributed nature of the target and inherent characteristics of the incident radar beam. Hence, in order to adequately characterize such complex responses, a coherency matrix is utilized. The backscattering information of a target along with the nature of the EM wave can also be known through coherency matrix, which comprises of averaged second-order statistical parameters (mostly variance) (Cloude, 2009; Cloude et al., 2012). This proves to be vital for modelling associated physical processes such as dielectric constant, soil moisture, etc. The received polarizations, in the case of hybrid systems, result in constructing a 2×2 coherency matrix $[J]$, also known as Wolf's coherency matrix (Cloude, 2009). Moreover, the elements of the matrix from the Stokes condition of partially polarization are expressed in terms of intensities. The matrix can be written as

$$[J] = \begin{bmatrix} \langle E_{LH} E_{LH}^* \rangle & \langle E_{LH} E_{LV}^* \rangle \\ \langle E_{LV} E_{LH}^* \rangle & \langle E_{LV} E_{LV}^* \rangle \end{bmatrix} \tag{2.7}$$

where E_{LR} denotes the left circular polarization transmission (*L*) followed by the reception (*R*) of either horizontal (*H*) or vertical (*V*) polarization, $\langle \bullet \rangle$ represents ensemble averaging operator with a suitable kernel and A^* is the conjugate of A. The coherency matrix can also be defined on the basis of Stokes parameters as

$$[J] = \frac{1}{2} \begin{bmatrix} S_1 + S_2 & S_3 + iS_4 \\ S_3 - iS_4 & S_1 - S_2 \end{bmatrix} \tag{2.8}$$

where i is the imaginary unit. In this context, the polarization behaviour of an EM wave attributing to the target's characteristics can be quantitatively examined by coherency matrix. This further demonstrates the potentiality of different polarimetric systems in determining the dimension of the coherency matrix.

2.3.2.2. Miniature Radar Observation: From Monostatic to Bistatic Configuration

The primary objective of miniature radio frequency (MiniRF) instrument onboard LRO constitutes microwave imaging of permanently shadowed regions (PSRs) of the Moon by acquiring data in a monostatic mode, i.e. the same antenna acts as a transmitter and receiver. This side looking system is based on hybrid polarimetry and has both S-/X-band data collection capabilities (Chin et al., 2007; Nozette et al., 2010). The monostatic scattering model facilitates the identification of water ice in at least 80 PSR craters, thereby providing resource evidence for potential human outpost (Spudis et al., 2010, 2013). However, one of the factors that permit the observation is enhancements in the circular polarization ratio (CPR) for some regions. This ratio can be defined to be an essential parameter for water ice detection as

$$\mathrm{CPR} = \frac{S_1 - S_4}{S_1 + S_4} \tag{2.9}$$

The inclusion of S_4 in the equation (2.9) describes the handedness of the polarization and numerator is suggestive of higher value compared to denominator during increased volumetric scattering scenarios, mainly due to the presence of anisotropic particles like water ice. In principle, the active lunar events such as mass wasting, fallback breccias, and impact melt flows produce decimetre scale roughness, which is responsible for inducing such CPR enhancements (Fa et al., 2011). Due to the technical malfunctionalities of the MiniRF transmitter, the mission has been extended for acquiring data as part of the bistatic campaign. This utilized the high energy radio signals from a 305 meter antenna of Arecibo Observatory, Puerto Rico as a transmitter while the backscattered echoes from the Moon end up at MiniRF receiver (Raney, 2007; Raney et al., 2011). Figure 6 shows the comparison of the monostatic and bistatic architecture, thereby signifying the importance of bistatic angle in the lunar context. Similar bistatic observations were performed for Clementine high gain antenna in conjunction with 70 m Deep Space Network (DSN) ground station (Nozette et al., 1996). This experiment reported enhanced CPR values at a bistatic angle of 0° near Shackleton crater, indicative of water ice, without any opposition effect observed in the North Pole. However, subsequent ground based radar imaging of the crater suggests the increased roughness near the inner rims responsible for exhibiting opposition signatures. Moreover, the measurements acquired from this bistatic architecture were Doppler based, while the employment of MiniRF bistatic campaign utilized both range and Doppler for data capturing (Nozette et al., 1996; Raney, 2007). Out of several chosen lunar features, the MiniRF experiment has shown an increased response to the opposition effect by the ejecta of Copernican aged craters and floor of the Cabeus south polar crater (Patterson et al., 2017). This provides new insights into deposition of near surface water ice, in case of PSRs, and dehydrated (dry) inclusions in the ejecta of equatorial craters. The physical properties of the lunar surface, however, are still under investigation for any dependency on the varying bistatic angle. This can be further demonstrated by associating the radar backscatter with regolith parameters.

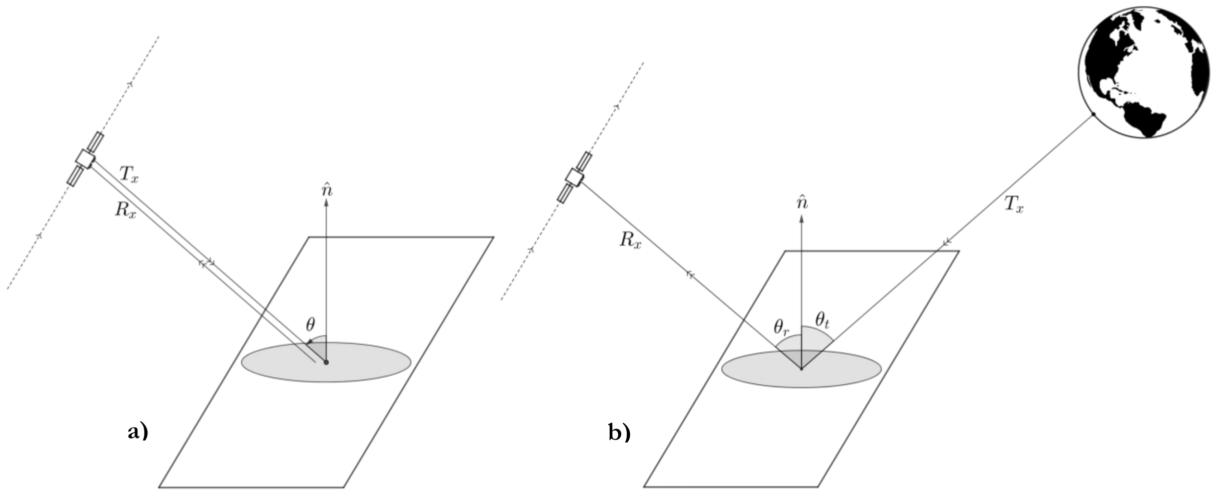

Figure 6: Radar architecture for a) Monostatic systems and b) Bistatic system, in the lunar perspective. The bistatic measurements are performed in coordination with Arecibo Observatory. In this diagram, the conventions are as follows: ñ is the surface normal, T_x and R_x are the transmitter and receiver antennas respectively, θ is the Radar incidence angle, in case of (a) and (θ_t, θ_r) represents the bistatic angle.

2.3.2.3. Radar Physical Backscattering Model

The interaction of EM wave with the surface can be modelled by estimating radar cross section (RCS), which is the measure of the reflected radar signals. Several studies have determined the relationship of RCS with surface parameters, i.e. roughness, dielectric permittivity and soil moisture, and technical configuration, i.e. wavelength, incidence angle and polarization (Beckmann & Spizzichino, 1963; Schmugge, 1983; Ulaby et al., 1982, 1986). In this context, two approaches are mainly followed to establish the correlation between RCS and other dependent variables. The former involves calibration of empirical/semi-empirical models for deriving a statistical basis in conjunction with experimental field data (Dubois et al., 1995; Oh et al., 1992, 1994). This directly links the measured backscatter in different polarizations (HH or VV) with surface roughness and soil moisture. However, in order to improve the empirical relationship, a sufficiently large amount of data are typically required, thereby making it site-dependent. The latter utilizes the physics-based theoretical models derived specifically for understanding the fundamental scattering mechanisms from different media (Beckmann & Spizzichino, 1963; Fung et al., 1992; Ulaby et al., 1986). Moreover, the strong theoretical background of microwave interactions enables the foundation of these models to be applicable for any site while taking into account different roughness domains and radar configurations.

One of the widely used physical models in simulating the RCS is the Integral Equation Model (IEM) (Fung et al., 1992). In principle, the diffraction theory for rough surfaces is employed to derive the theoretical model, thereby reconstructing the target's backscatter. This approach is preferable for extraterrestrial regoliths as compared to other empirical models due to its site-independent nature and larger validity range of the surface roughness. As part of considerations in this model, the entire surface is statistically resolved into two components: correlation length and root mean squared (RMS) height. The former represents the horizontal profile of the surface by modelling the correlation function (maybe Gaussian or exponential) while the latter is the standard deviation of the surface height, thereby exhibiting the vertical profile. Evidently, there are different theoretical models with different validation range based on simplifying assumptions for both high and low frequency regions. In this, the standard models are regarded as Kirchhoff (physical optics and geometrical optics) and small perturbation approximation (SPA) (Beckmann & Spizzichino, 1963; Ulaby et al., 1986). However, the theoretical basis of IEM is implemented by unifying both of the standard models and hence, its applicability to varying roughness scale is further expanded. This approach comprises of the randomly oriented rough bare surface, which behaves as an ideal platform for incident radar echo, without any acting constraints of roughness and frequency variations. Due to the complexity of the model, its complete version is computationally intensive, thereby deploying the approximate solutions with respect to the application.

Generally, the IEM is potentially effective for small to moderate roughness (low to medium frequencies) in applications involving surface parameter retrieval (Fung et al., 1992). The model is valid in the range $k\sigma_h < 3$, where k is the wavenumber $\left(k = {}^{2\pi}/_{\lambda_0}\right)$, λ_0 is the wavelength and σ_h is the RMS height. The RCS (σ^0) at pp polarization is given by

(2.10)

$$\sigma_{pp}^0 = \frac{k^2}{2} e^{-2k_z^2\sigma_h^2} \sum_{n=1}^{\infty} \frac{\sigma_h^{2n} \left|I_{pp}^n\right|^2 W^n(-2k_x, 0)}{n!} \quad \dots \text{a}$$

where

$$I_{pp}^n = (2k_z)^n f_{pp} e^{-\sigma_h^2 k_z^2} + \frac{k_z^n \left[F_{pp}(-k_x, 0) + F_{pp}(k_x, 0)\right]}{2} \quad \dots \text{b}$$

p : horizontal (h) or vertical (v) polarization

$$f_{vv} = 2R_v / \cos\theta \ , f_{hh} = -2R_h / \cos\theta \quad \dots \text{c}$$

$$[F_{vv}(-k_x, 0) + F_{vv}(k_x, 0)] = \frac{2\sin^2\theta\,(1 + R_v)^2}{\cos\theta} \left[\left(1 - \frac{1}{\varepsilon}\right) + \frac{\varepsilon - \sin^2\theta - \varepsilon\cos^2\theta}{\varepsilon^2 \cos^2\theta}\right] \quad \dots \text{d}$$

$$[F_{hh}(-k_x, 0) + F_{hh}(k_x, 0)] = -\frac{2\sin^2\theta\,(1 + R_h)^2}{\cos\theta} \left[\frac{\varepsilon - 1}{\cos^2\theta}\right] \quad \dots \text{e}$$

R_h and R_v : Fresnel reflection coefficients for horizontal and vertical polarizations respectively at an angle of incidence θ for slightly rough surface (low frequency)

$$R_h = \frac{\cos\theta - \sqrt{\varepsilon - \sin^2\theta}}{\cos\theta + \sqrt{\varepsilon - \sin^2\theta}} \quad \dots \text{f}$$

$$R_v = \frac{\varepsilon \cos\theta - \sqrt{\varepsilon - \sin^2\theta}}{\varepsilon \cos\theta + \sqrt{\varepsilon - \sin^2\theta}} \quad \dots g$$

ε : complex dielectric permittivity, $k_z = k\cos\theta$, $k_x = k\sin\theta$

$W^n(u,v)$: Fourier transform of the nth power of surface correlation function $\rho(x,y)$

$$W^n(u,v) = \frac{1}{2\pi}\int_{-\infty}^{\infty} \rho^n(x,y) e^{-jux-jvy} dx\, dy \quad \dots h$$

Further assumptions are made in regards to the estimation of RCS as a function of dielectric constant, incidence angle, frequency, correlation function, RMS height and correlation length (Fung et al., 1992). The surface correlation function (assumed to be isotropic) is represented as

$$\rho(x,y) = e^{-\frac{x^2}{L_x^2}-\frac{y^2}{L_y^2}} \text{ (Gaussian)}$$

$$\rho(x,y) = e^{-\frac{|x|}{L_x}-\frac{|y|}{L_y}} \text{ (Exponential)} \quad (2.11)$$

where L_x and L_y denote the correlation length in the x and y direction, respectively.

The sensitivity of the RCS to the surface parameters is simulated, as per equations (2.10) and (2.11), and carefully examined before implementing the inversion modelling. The sensitivity plots are also analyzed to evaluate the behaviour of the incoming radar wave with respect to different topographic conditions and radar configurations. Hence, the IEM serves as a precursor to the prediction of unknown electrical and roughness parameters of the soil, thereby aiding to the potential of theoretical forward simulation practices in petrophysical content retrieval.

2.3.2.4. Physical Properties of the Regolith: Dielectric and Geotechnical Characterization

Owing to the space weathering processes, the modelling of the regolith evolution in conjunction with alterations in the physical properties remains a quest among many researchers. The penetration capabilities of the microwave backscatter facilitate a new perspective in envisaging the surface, near surface and subsurface characterization. This further attempts to redesign the retention framework of the implanted volatiles based on the knowledge of electrical and geotechnical variants. Some of these include complex dielectric response, bulk density, porosity, void ratio and relative density of the regolith.

The dielectric content of the regolith is associated with the subsequent attenuation of the electric field due to the polarization of molecules within the medium (Olhoeft & Strangway, 1975). This can be further explained in terms of the regolith response to the interaction of the EM wave. The attenuation factor (A_F) represents the weakening of the transmitted radar signal through the regolith and hence, decreases as the depth increases. This parameter is strongly aligned with the penetration depth of the electric field, which can be represented as

$$A_F = \exp\left(\frac{4\pi f \varepsilon'' d}{c\sqrt{\varepsilon'}}\right) \quad (2.12)$$

where f is the frequency of the incident wave, d is the regolith thickness, c is the speed of light and ε represents the complex dielectric permittivity with $(\varepsilon', \varepsilon'')$ as the real and imaginary components respectively. The real and imaginary dielectric parts are used to estimate the loss tangent, wherein the phase shift of the dielectric polarization is estimated relative to the transmitted wave. Moreover, the real part is dependent on the bulk density (ρ in g/cm^3) of the regolith as (Olhoeft & Strangway, 1975)

$$\varepsilon' = (1.93 \pm 0.17)^{\rho} \tag{2.13}$$

Hence, the measure of dielectric permittivity and bulk density of the uppermost regolith can be expressed in the form of an empiric relationship. Due to the attenuation, loss tangent ($\tan\delta$) is directly related to bulk density and ilmenite content (S). The estimated uncertainty of the measure is ± 0.0035 (Olhoeft et al., 1974; Olhoeft & Strangway, 1975). Furthermore, the penetration depth for S-band microwave varies from 0.5 to > 5 m based on the ilmenite concentration in the regolith (Fa & Wieczorek, 2012; Fa et al., 2011). This can be modelled with a power law function of loss tangent as

$$\tan\delta = 10^{0.038S + 0.312\rho - 3.26} \tag{2.14}$$

Several studies have been carried out in estimating the complex dielectric constant of the regolith. The in situ electrical experiments, performed at the Apollo 17 landing site, and laboratory assessment of the returned lunar samples have provided a benchmark for validating the remote sensing based algorithms (Chung et al., 1970; Gold et al., 1976; Olhoeft et al., 1974). An attempt has been made to utilize the thermal radio emissions from the regolith for retrieving the polarization variability and hence, dielectric properties (Soboleva & Pariiskii, 1964). Another effective dielectric estimate of 3.0 ± 0.2 has been observed based on the acquisition of oblique scattering characteristics of the regolith through quasi-specular bistatic radar system (Tyler, 1968). Moreover, Hagfors (1970) has employed radar observations of the regolith to determine the lunar dielectric permittivity of 2.7 ± 0.7. Additionally, Campbell et al. (2002) have proposed to extract the backscattering properties from the Fresnel coefficients and incidence angle, thereby estimating the minimum real component of dielectric constant for a rock poor regolith. This method has been further verified through airborne SAR campaigns over terrestrial Martian analogues. An improved simulation approach has been presented by revaluating the returned regolith samples from the Apollo/Luna missions and deriving an empirical relation through vector radiative transfer theory (Fa & Wieczorek, 2012; Fa et al., 2011). Specific to the MiniRF data, the utilization of a roll invariant anisotropy parameter has been employed to the dielectric inversion modelling near the regolith of Apollo 17 landing site (Bhattacharya et al., 2015). However, it works only with the bounding limits of the anisotropy, rather than the spatial variability within the range. In recent times, Liu et al. (2017) have modified the Campbell inversion model by incorporating the effect of local topography on the polarization base, wherein the co-pol backscattering coefficients are derived using a two-layer model.

Apart from this, increased applicability of machine learning approaches, particularly neural networks, in microwave remote sensing for surface parameter retrieval provides a unique modelling perspective (Atkinson & Tatnall, 2010; Kohonen, 1988). The forward relation of backscattering coefficients with dielectric property and surface roughness profile is usually envisaged through simulation over a realistic range of dependent variables. Upon establishing a reliable model, one parameter can be fixed, say roughness, and others could be retrieved inversely and vice-versa (Dawson et al., 1993). In this, one of the promising approaches is multi-layer perceptron (MLP) neural networks, which consists of one input and output layer with a number of hidden layers in between (Rumelhart et al., 1986). The description of the typical regression model is elaborated in Appendix A. This technique is well tested in the Earth-based applications concerning the retrieval of soil moisture from SAR (Baghdadi et al., 2002; Dawson et al., 1993). Interestingly, the lack of ground data for the lunar regolith, and even other planetary bodies makes this inversion technique most suitable compared to other minimization practices. Moreover, there is also no initial assumption on the distribution of data, proving it to be flexible over a variety of roughness and incidence angle ranges. The efficiency of the inversion framework could be tested by analyzing the accuracy-related statistical parameters for both the training and testing data. In essence, the retrieved dielectric constant from the model is further utilized for deriving the variations in the regolith characteristics, thereby classifying different lunar terrains.

The geotechnical variants of the regolith mainly evaluate the compaction of the grains. This is represented by the number of voids present in the granular space. Moreover, the emergence of such voids attributes to the crystallographic defects of the constituent grains (Carrier III et al., 1991). One of the parameters that define the void spaces is the porosity (n). It is the volume ratio of the voids to the grain and hence, can be derived as

$$n = 1 - \rho/G\rho_w = 1 - \rho/3.1 \tag{2.15}$$

where G is the specific gravity of the regolith grain, ρ is the bulk density and ρ_w is the density of water (expressed in 1 g/cm^3). The specific gravity strongly depends on the nature of the lunar material and hence, a typical basaltic regolith feature exhibit a value greater than 3.32. However, for scientific purposes, the recommended measurement is 3.1, as in equation (2.15) (Carrier III et al., 1991). This relationship has been established based on the correlation analysis of the returned lunar samples. Additionally, due to the influx of space weathering agents, the crystal structure undergoes several deformations. This can be quantitatively estimated by the void spaces between the grain particles, thereby providing a complementary parameter of the void ratio (v) to the porosity.

$$v = n/(1 - n) \tag{2.16}$$

These geotechnical parameters present a unique viewpoint in the stability of the regolith, thermal conductivity and penetration of the ionizing radiations like solar wind and galactic cosmic rays. Another critical parameter responsible for defining the degree of particle packing within a regolith grain is relative density (D_R) (Carrier III et al., 1991). This can be estimated for granular soils as

$$D_R = (v_{max} - v)/(v_{max} - v_{min}) \tag{2.17}$$

where v_{max} is the maximum void ratio of the soil (corresponding to maximum porosity and minimum bulk density) and v_{min} is the minimum void ratio of the soil (corresponding to minimum porosity and maximum bulk density). An ordinal classification of lunar soils has been tabulated based on the compaction characteristics denoted by relative density, as in Table 1. The physical properties of the lunar regolith are strongly aligned with the estimates of absolute bulk density and relative density. For instance, two regolith samples may have different relative densities for the same bulk density and vice versa. The in situ experiments of the Apollo missions have provided an approximate measure for a relative density of 65% in the top 15 cm (Carrier III et al., 1991). However, it becomes denser (about 90%) as the depth increases after 30 cm. Evidently, the practical bounding limits of relative terrestrial soil density are in the range of 65% to 75%, thereby showcasing the highly profound nature of the lunar compaction measurements. This can be further demonstrated by the extensive gardening and densification of the lunar soil, probably due to the generated shock waves from large impact events.

Table 1: Characterization of regolith based on the relative density (Carrier III et al., 1991).

Relative Density (in %)	Description
0 – 15	Very loose
15 – 35	Loose
35 – 65	Medium
65 – 85	Dense
85 – 100	Very dense

2.4. Summary

In this chapter, a detailed discussion on the technicalities of ^{3}He sources along with its implantation scenarios, specific to the lunar case, has been described. Moreover, several constraints of the regolith have been associated with the ^{3}He retentivity, thereby facilitating an elaborative framework for performing further studies in solar system science. Along with this, the remote sensing perspectives in the context of solar wind dynamics for lunar regolith characterization have been mentioned. These include imaging spectroscopy and radar astronomy, which are essential for defining the mineralogical, electrical and geotechnical attributes of the regolith and hence, provide significant insights into the retention physics of solar wind implanted ^{3}He. Furthermore, the subsequent chapters focus on the integration of the aforementioned approaches to put the thesis objectives in traction.

3. STUDY AREA AND DATASETS

This chapter highlights the geological significance of the test site in resembling the local pyroclastic eruptions to that of the traditional Hawaiian lava fountaining events, illustrates the potential of the site for future landing missions by revisiting its sequential formation hypothesis, and presents a brief overview on multi-sensor datasets used for further processing, analysis and interpretation.

3.1. Vallis Schroteri, Aristarchus Plateau, Lunar Nearside: Geological Background

Vallis Schroteri forms the largest sinuous lunar rille, emerging in the vicinity of the craters Aristarchus and Herodotus with its morphologic features spreading across the plateau on the nearside of the Moon (Lucey et al., 1986; McEwen et al., 1994; Zisk et al., 1977). The plateau is known for its geological diversity in exhibiting the regolith depositions of volcanic and impact-related origin (Campbell et al., 2008; Chevrel et al., 2009; Weitz et al., 1998; Whitford-Stark, 1982). The presence of crustal-anorthositic materials mantled by iron-rich pyroclasts and basaltic lava flows displays a complex stratigraphic relationship between different features in the plateau (Whitford-Stark, 1982; Zisk et al., 1977). Due to the lava emplacement of the crustal layers intermixed with fresh ejecta and dark glassy enrichment, the plateau resembles a topographically elevated terrain (~2 km) relative to that of the surrounding mare regions (Zisk et al., 1977). The gradual depression near the margins of the plateau is marked by mantling of lava from Oceanus Procellarum, associated with some of the youngest volcanic flows on the surface (Hiesinger et al., 2003). The cross-sectional stratigraphy of the eastern margin is highlighted by the dominance of two large impact craters, namely Herodotus and Aristarchus (Chevrel et al., 2009; Zisk et al., 1977). Along the northwestern margin, the plateau is separated from the Agricola peaks of 150 km long by mare filled straits. Throughout the plateau, there exists a significant number of rilles without the inclusion of topographical shielding near the source vent as compared to that of the Vallis Schroteri (Chen et al., 2008). The ubiquitous rille segments in the region attribute to the involvement of pronounced localized volcanic activity in the evolution of the Aristarchus plateau. Significantly, the complex morphology of the Vallis Schroteri rille allows the possible inclusion of local pre-eruption stratigraphy for orienting the structure of bimodal lava flow through the surface (Figure 1). Therefore, this region is of great interest in deriving the final flow morphology from revealing the stratigraphic evolution of the Aristarchus plateau.

The primary formation of sinuous rilles remains a mystery in terms of determining the morphological origin of the volcanic substrate. Previous investigations have led to the discovery of lava flow hypothesis for the emergence of Hadley Rille near the Apollo 15 landing site with exposed layers of basaltic content in the walls of the rille (Heiken et al., 1991; NASA Manned Spacecraft Center, 1971). The volcanic flow from a source erodes the surface by a large proportion of blocks in a matrix of aphanitic rocks and mineral fragments (Cameron, 1964). In the case of the eruption of gas-rich lava, the fractures along the surface provide the fluidization of escaping gas (McCall, 1970). The possible rille evolution also results from a roof collapsed lava tube, wherein the inside of the tube is exposed to the space environment. There are evidence for the intense erosional activity of the underlying bedrock by the unstable flow of lava, as observed from the terrestrial volcanic analogues (Williams et al., 2000). The geomorphology of the rille typically evolves into a well-developed meander patterns with the representation of the head as the potential source of the volcanic vent (Head & Wilson, 1980). In some instances, the volcanic origin of mechanical and thermal erosion is not solely responsible for the rille formation. The crest of the ridges also contributes to the lava overflow events, thereby resulting in the construction of channels by exhibiting the distributary flow of lava away from the central rille (NASA Manned Spacecraft Center, 1971; Zisk et al., 1977). In essence, the sinuous rilles are originated by either of these aforementioned processes or the combination of both. Precise identification of the geomorphological parameters for the estimation of probable formation event could provide a deeper understanding of the lunar emplacement scenarios and past volcanic environments.

The sequential processes required for examining the formation of Vallis Schroteri rille in the Aristarchus plateau have not been well formulated. The key morphologic components of the Vallis Schroteri rille are: a) Primary rille, b) Inner rille, and c) Cobra head. The source vent of the rille, Cobra head, comprises of a 10 km wide topographic depression surrounded by a low shield of 900 m relief (Zisk et al., 1977). The combination of rock-free regolith and hummocky terrain characterizes the flanks of the shield. Moreover, an additional source of volcanic features responsible for the possible formation of Cobra head construct are mounds and lava fan (Chen et al., 2008). The mounds are situated at the base of the shield while the lava fan is observed to be extending to the crater floor along the wall of the mare-filled, Imbrian-aged crater Herodotus (Head & Wilson, 1980). These morphological features are indicative of the presence of multiple vents of volcanic origin along with possible breaching of the northern rim of the crater Herodotus by the lava flow from the outside. The formation of the Cobra head has been associated with the eruptions during the lava fountaining events, wherein ash flow, volcanic spatter and tephra aid in constructing the source vent (Garry & Bleacher, 2011). This initiates a sheet of lava flow influenced by the initial topography, thereby evolving a foundation channel of a 155 km long primary rille within the sheet. The turbulent flow of lava further results in an enhanced rate of thermomechanical and construction erosion, attributing to the deepening of the channel depth (Williams et al., 2000). Moreover, the U-shaped floor of the primary rille accommodates the inner rille with tight gooseneck meanders. The scarp at the distal end of the primary rille undergoes the active lava overflow event, thus extending the inner rille up to the Oceanus Procellarum.

Comparing to the terrestrial volcanic construct of the Mauna Loa eruption, similar emplacement scenarios of lava backup and redirection have been observed (Zisk et al., 1977). This allows to compare the eruption dynamics of the volcanic features with similar morphologies on different planetary bodies with the terrestrial analogues. Apart from this, the region of the plateau is also characterized by thick pyroclastic deposits (~20 m), commonly referred to as dark mantled deposits (DMDs) (Campbell et al., 2008; Horz et al., 1991). It is a low albedo stratigraphic unit of glassy spheroids with possible emplacement in the Imbrian period (3.7 Ga – 3.6 Ga) through a large localized lava fountaining event (Cameron, 1964; Campbell et al., 2008). This is aligned with the formation processes of the Vallis Schroteri rille. Previous studies have shown the potential of DMDs to preserve up to 300 ppm of indigenous water and these primitive samples could provide new insights into the magmatic evolution associated with lunar mantle (Campbell et al., 2008; Chen et al., 2008; Chevrel et al., 2009; Zisk et al., 1977). The diversity of the Aristarchus plateau, with a special emphasis on the association of the possible bimodal volcanism of the Cobra head and presence of pyroclastic deposits, makes it a significant nearside landing site candidate for testing the in-situ resource utilization (ISRU) technologies.

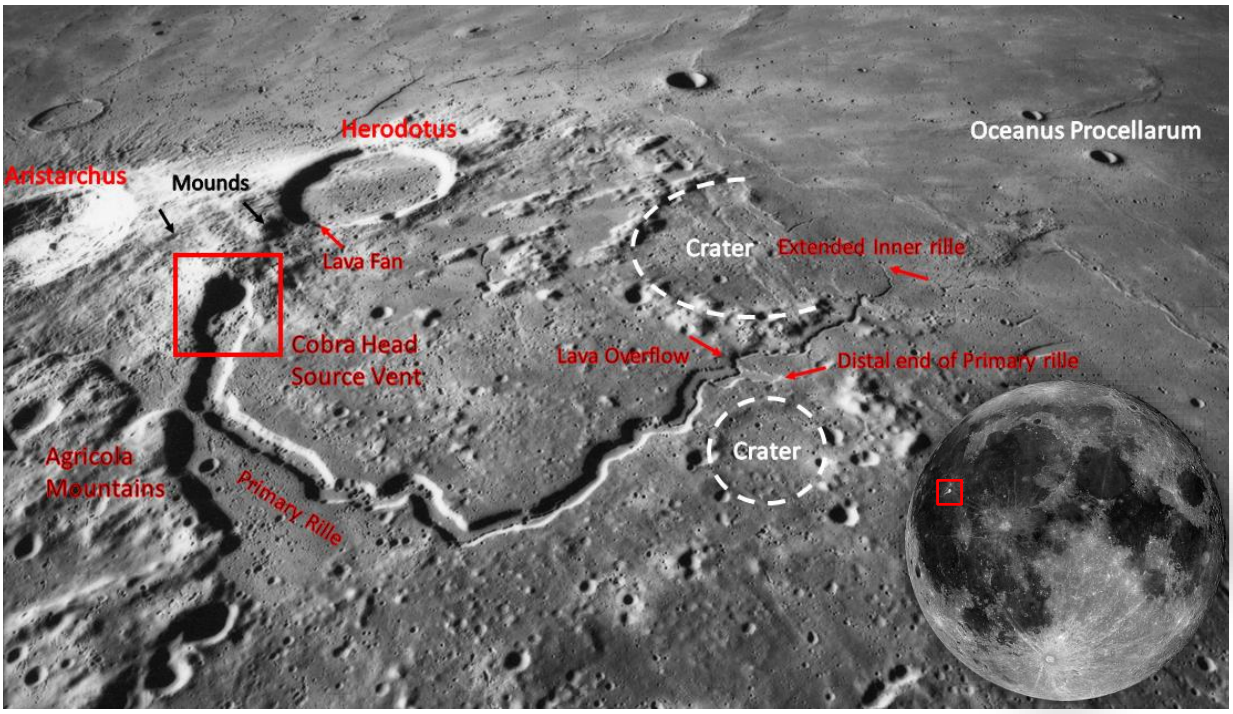

Figure 7: Geological Perspective of the Vallis Schroteri over Aristarchus Plateau (Base Image: Apollo 15 Camera). The location of the plateau is depicted by the red box in the Clementine mosaic of the Moon in the bottom right.

3.2. Lunar Datasets

The distribution of solar wind implanted ^3He can be mapped efficiently by utilizing the high spectral coverage of the Moon Mineralogy Mapper (M^3) instrument onboard Chandrayaan-1. Moreover, the physical properties of the regolith are extracted by processing the Miniature Radio Frequency (MiniRF) data, thereby testing the applicability of the retrieval algorithm. In addition, the topographic information from Global Lunar DEM (GLD) provides new insights into estimating the spatial orientation of ^3He content with depth. This DEM is of 100 m spatial resolution, with a vertical accuracy of 10-30 m, prepared through stereophotogrammetric processing of LRO Wide Angle Camera (WAC) images (Scholten et al., 2012). In essence, this proves to be a better estimate as compared to the lunar orbiter laser altimeter (LOLA) product as the interpolation of elevation values in the non-footprint regions of the laser beam may yield inaccurate results due to the presence of data gores (Bray et al., 2012).

3.2.1. Chandrayaan – 1 Moon Mineralogy Mapper (M^3)

Chandrayaan–1 Moon Mineralogy Mapper (M^3) is a push-broom imaging spectrometer having the visible to near-infrared coverage of 0.42 – 3.0 µm in 85 spectral bands. In principle, the data acquisition of lunar regolith through M^3 is carried out in two modes: target and global (Pieters et al., 2009). The former is preferred to capture priority regions from 100 km orbit with a higher spatial resolution of 70 m/pixel. In contrast, the latter provides full coverage of the Moon operating majority of the time, at a spatial resolution of 140 m/pixel. The scientific objective behind this instrument involves a detailed mineralogical assessment for understanding the geological evolution of lunar crustal processes and deep-seated lithologies. As part of data products, the M^3 repository is organized into three planetary data system (PDS) labels: NASA Level 0 (raw data in digital number), NASA Level 1B (calibrated data in radiance) and NASA Level 2 (calibrated data in reflectance) (Pieters et al., 2009). In this research, thermally and photometrically corrected reflectance data (PDS Level 2) is used. The advantage of employing M^3 data over traditional Clementine data is its higher spectral coverage which could potentially delineate the effects of space weathering more precisely while preserving the spatial resolution element. Moreover, the impact of incoming solar wind plasma on the regolith could be well understood by carefully examining the behaviour of associated space weathering agents. The variations in the spectral content of different minerals can be clearly seen in Figure 8(a), wherein the blue colour represents the abundance of olivine and pyroxene assemblages, reddish tint signifies the dominance of nanophase iron deposition in the existing pyroxene lithology and green colour is the region unaffected by the influence of 1000 nm and 2000 nm absorption channels.

3.2.2. Lunar Reconnaissance Orbiter Miniature Radio Frequency (MiniRF)

MiniRF instrument onboard LRO operates in both S- and X-band frequency for retrieving the backscattering response of the lunar regolith at an incidence angle of ~49^0. The linear receive data is generally acquired in either baseline SAR mode or zoom mode by transmitting circularly polarized wave from ~50 km altitude (Nozette et al., 2010). As per PDS standards, the hybrid polarimetric data products are provided in a multilooked format for both monostatic and bistatic acquisitions. Following the failure of the transmitter in collecting the radar images, the MiniRF team utilized the high power transmission at S-band wavelength from the Arecibo Observatory (AO) located in Puerto Rico. This has led scientific breakthroughs in identifying the coherent backscattering opposition effects (CBOE) from specific lunar regions (Patterson et al., 2017). In essence, the bistatic imaging provides physical insights into the nature of regolith grains, especially near the agglutinitic abundance of pyroclastic glass beads. The available bistatic data mainly comprises of three product labels: bistatic experimental data records (BSEDR), bistatic reduced data records (BSRDR) and bistatic derived data records (BSDDR). The present study uses the calibrated (both radiometrically and polarimetrically) data product of BSRDR, wherein the pixel size is resampled to 100 m. In addition, the angular dependence of the bistatic data can be found in BSDDR label, which captures the radar geometry related parameters (Patterson et al., 2017). In the MiniRF BSRDR data product, four Stokes parameters along with circular polarization ratio (CPR) image are stored. The total power of the received backscattered field is represented by the first Stokes parameter (S_1), as seen in Figure 8 (b). Quantitatively, the measure of the difference between the horizontal and vertical polarized radar echo is depicted by the second Stokes parameter (S_2). Moreover, the complex phase differences are captured by the third and fourth Stokes parameters (S_3 and S_4). The increased roughness of the surface and probable presence of water-ice can be exhibited in a dimensionless quantity of CPR, which is the ratio of $(S_1 – S_4) / (S_1 + S_4)$. Apart from this, the BSDDR data product comprises of latitude, longitude, bistatic angle, incidence angle, emission angle, and range (assuming the Moon to be a sphere of radius 1734.4 km).

3.3. Software

In the accomplishment of the research, the following softwares are required:

ENVI IDL, for spatial referencing and image processing of the multi-sensor datasets.

R Programming Environment, for estimating the directional spatial orientation of the ^3He with respect to depth (R Core Team, 2018).

Python, for performing a simulation of the IEM and inverse modelling associated with dielectric content retrieval.

ArcScene, for 3D Visualization of the generated output results with the GLDEM100.

ArcMap, for assessing the topographical information and analysis of the final ^3He abundance map.

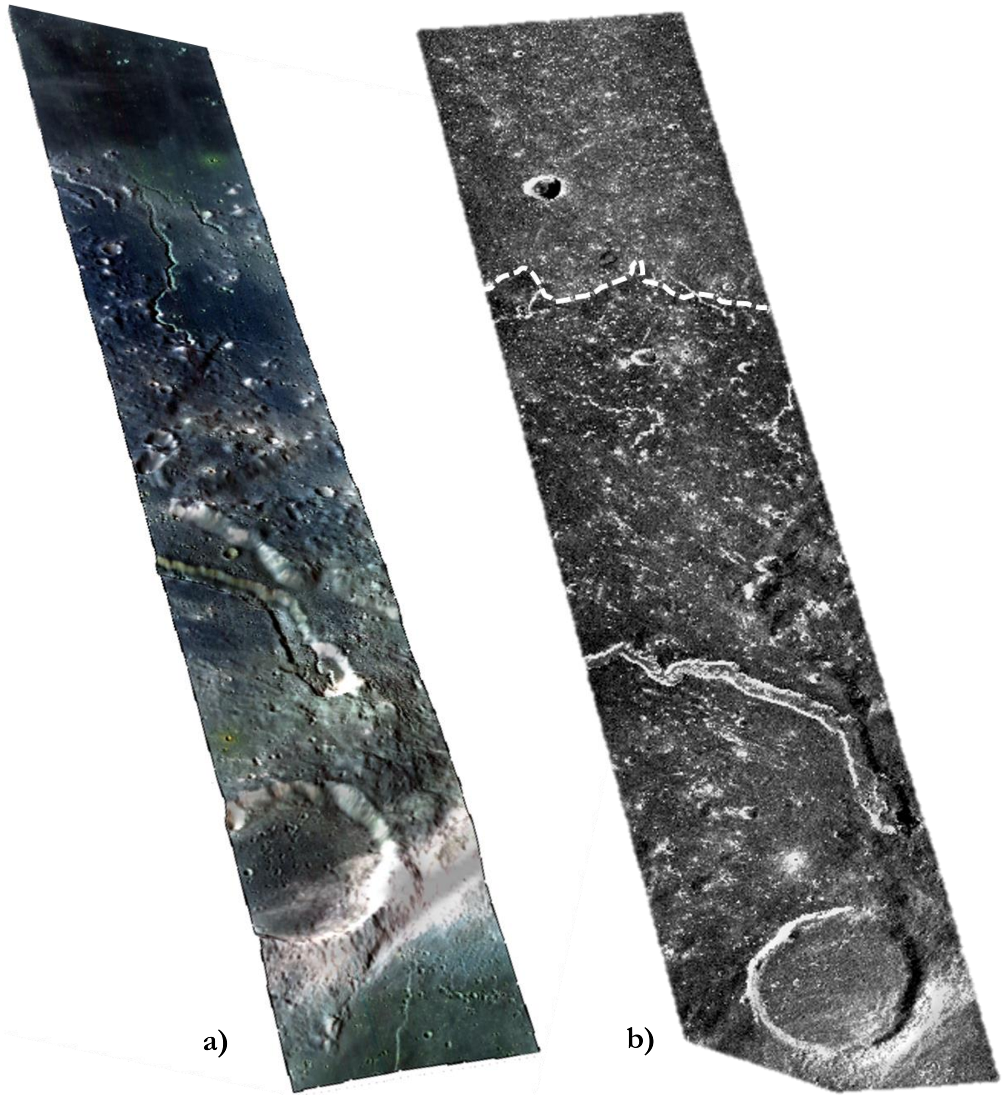

Figure 8: a) M³ False Colour Composite (FCC) of Vallis Schroteri region (Red: 1000 nm, Green: 1578 nm, Blue: 2000 nm). b) MiniRF S1 Image of Vallis Schroteri, with a separation between dark space (pyroclastic region) and cloudy space (non-pyroclastic region) by the white dotted line.

3.4. Summary

This chapter overviews the geological context related to the study site of Vallis Schroteri in the diverse Aristarchus Plateau. The availability of different types of geomorphological features enables the vicinity to be critically explored for the abundance of solar wind implanted ^{3}He. Moreover, the association of the plateau with pyroclastic deposits enhances its importance in terms of prospective resource intensive landing site. The behaviour of this regolith towards the ^{3}He retention could provide new insights into strategizing suitable site selection criterion for future robotic-armed/manned landing mission, thereby aiding to the remote sensing advances in the ISRU technologies. In addition, the chapter also highlights the utilization of multi-sensor datasets and software for understanding the spatial distribution of ^{3}He, correlated with regolith dynamics, across the scene.

4. METHODOLOGY

This chapter facilitates the reader an understanding of the entire research in regards of methods and overviews different techniques adopted for estimating the implanted ^{3}He content within the regolith, characterizing the directional orientation of the repository in conjunction with depth profile, and simulating the radar backscatter for efficient retrieval of petrophysical properties using inversion approach.

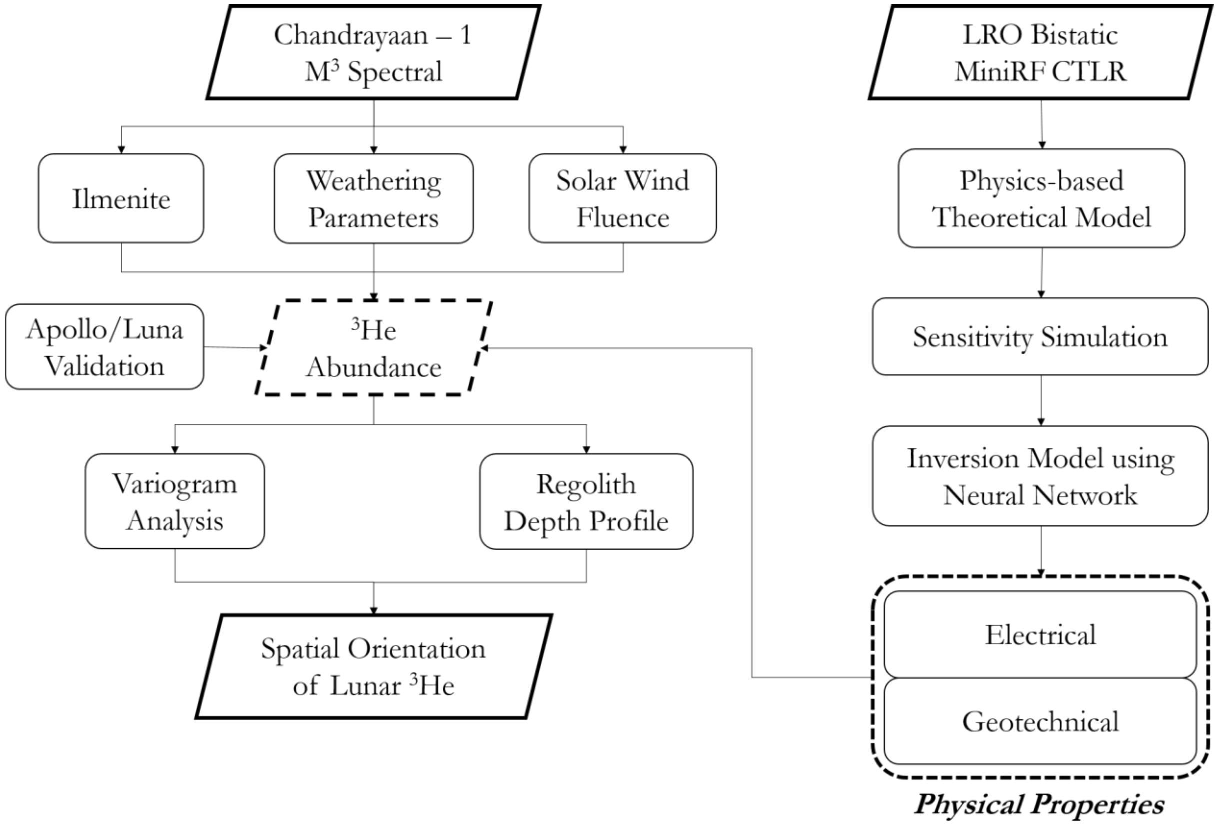

Figure 9: Flowchart of the adopted methodology in the research.

4.1. Data Preprocessing

The multi-sensor datasets are subjected to initial pre-processing stage, which consists of spatial referencing and co-registration. The Moon has a well-defined standard spheroid of 1737.4 km radius and datum, named GCS_Moon_2000 and D_Moon_2000, respectively with different map projection conventions under the planetocentric system (Synder, 1987). In general, the mid-latitude lunar regions are assigned the Equirectangular projection, wherein all the lines of latitude and longitude are parallel to each other. This study utilizes the map locations of the associated pixels for generating the geographical look-up table (GLT). As part of the approach, the conventional polynomial warping with ground control points (GCPs) is neglected, thereby making it superior over others in the planetary environments. Upon spatially referencing the data onto a standard map projection, co-registration is performed to align the overlapping regions of interest geometrically. This is done by typically obtaining a relationship between the warped image and base image through a number of GCPs, wherein the registered pixels extract the spatial attributes of the analogous features. However, due to the lack of specific identical traits, a semi-supervised marking of the GCPs is implemented in this study. This utilizes the area-based matching to compare the grayscale values of two images, thereby identifying the conjugate locations by taking into account the similarity index of the grayscale patterns. Despite this, certain locations do exhibit a miss-matched scenario due to the lack of significant features on the Moon. Hence, the re-identification of the equivalent sets of structure in the overlapping area is made by integrating the visual interpretation aspect. A total of 26 GCPs are selected by assigning the base image as M^3 data and warp image as MiniRF data. The warped image further utilizes the first order polynomial transformation model to match the base image. Meanwhile, the ground resolution cell size of the MiniRF data (100 m) resamples to 151.7 m. The reason for down-sampling resides in the fundamental understanding of the resolution cell. This states the incapability of the low resolution pixel, i.e. M^3 (151.7 m), to accommodate for the information corresponding to a higher resolution cell, whereby the spatial quality of the data suffers a significant degradation. In this research, the adopted resampling scheme is the nearest neighbour as it does not modify the data after transformation. However, the linear features may appear jagged in the output resampled image, but this is not much of a concern for the lunar study sites (Parker et al., 1983). The other methods, like bilinear and cubic, involving the weighted average of the nearby pixels strongly influence the estimation of polarization parameters like entropy, alpha angle and anisotropy inherently (Cloude, 2009). These resampling approaches are, thus, not recommendable for the applications of MiniRF data processing. The adopted co-registration framework incorporates only the 2D spatial information without considering the topographical variants. Therefore, the present study employs a quantitative error estimate by integrating the elevation content for the considered swath of images, as elaborated in Appendix B.

4.2. Retention Hypothesis of Solar Wind ^{3}He

The incident hot ions, directed along the magnetic field lines, of the solar wind plasma, interact with the regolith, thereby implanting the volatiles. This proves to be efficient in terms of monitoring the solar wind flux, which indeed provides a framework for quantifying the overall surficial repository. The regolith processes can be modelled by incorporating the spectral characteristics of the Chandrayaan – 1 M^3 data. Moreover, the inherit factors responsible for altering the content of the soil are envisioned, wherein the quality of the retention is focused upon. The sequential formulation of this research for achieving the insights above is clearly stated in Figure 9.

4.2.1. Theoretical Modelling of Normalized Solar Wind Plasma Distribution

The present study emphasizes the influence of topography on the relative measurements of the integrated solar wind plasma flux distributed across the regolith, as illustrated in Figure 10. The variations in the shielding, due to the Earth's magnetotail, are quantitatively considered for a synodic month of 29.53 days. Since the revolution of the Moon around the Earth is the same as that of the rotation about its axis, all the regions of the regolith receive only half of the total solar wind plasma. Due to this reason, the nearside is comparatively less exposed than the farside. Also, the impact of the Moon's axial tilt (~1.5^0) on the plasma distribution is found to be least significant, thereby neglecting this segment in the current approach (Johnson et al., 1999). In this regard, the relative estimation of the solar wind fluence involves the quantification of local incidence to account for the topographical variations in the model. This, however, can be eliminated for the global assessment of the plasma flux distribution, as in Johnson et al. (1999) and Fa & Jin (2007).

As part of derivation, consider the incidence angle (θ_0) of the solar wind to be 45° with an assumed direction of near parallel to the Moon's rotation plane. The surface slopes, in x and y direction, are taken as $\alpha = \tan\omega$ and $\beta = \tan\gamma$, respectively (from GLDEM100). Due to the differences in the regional topographical setting, the incidence angle of the plasma flux changes locally with surface slopes as (Cloude, 2009)

$$\theta_{0l} = \cos^{-1}\left(\frac{\cos\omega\cos(\gamma-\theta_0)}{\sqrt{(\cos\gamma)^2(\sin\omega)^2+(\cos\omega)^2}}\right) \tag{4.1}$$

Following the estimation of the local incidence angle, the solar wind flux can be computed for any location based on the selenographic latitude (λ) and longitude (φ). Let δ be the angular distance from the subsolar point, varying with respect to different sun angle conditions ($\delta < 90°$). It is assumed that the solar wind ions impact the regolith at a local variable angle of θ_{0l} and hence, the maximum fluence is considered along the direction of the ions (F_0). This causes the incoming fluence at the subsolar point to become $F_0 \cos\theta_{0l}$, thereby providing a new perspective in the plasma flux alterations due to the mechanical influences. Thus, the solar wind plasma fluence at any specific location (λ, φ) is represented by incorporating a topographic dimension of θ_{0l} as

$$F(\lambda, \varphi, \theta_{0l}) = F_0 \cos\theta_{0l} \cos\delta \tag{4.2}$$

This can be further evaluated by implementing the shielding variations as described in the modified solar wind fluence model, wherein the theoretical correction of the absolute longitudinal error is accounted (Fa & Jin, 2007). However, the aforementioned model provides a relativistic monthly estimate of the global parameter, thereby completely ignoring the local topography. In this study, a generic solar wind fluence model is proposed, which includes the terrain variations. The previously developed model can, therefore, be improved for efficient retrieval of ³He especially in the vicinities with abrupt topographical changes. The monthly solar wind fluence is predicted as

$$F(\lambda, \varphi, \theta_{0l}) = F_0 \cos\lambda \cos\theta_{0l} \begin{cases} 2+\sin(\varphi - f\pi) - \sin(\varphi + f\pi), & |\varphi| \le \pi(0.5-f) \\ 1+\sin(|\varphi| - f\pi), & \pi(0.5-f) \le |\varphi| \le \pi(0.5+f) \\ 2, & \pi(0.5+f) \le |\varphi| \le \pi \end{cases} \tag{4.3}$$

In this, the uncertain proportion of the magnetotail shielding is considered, thereby quantifying the most probable amount of plasma flux apt for all the conditions. The days for which the Moon is in the Earth's magnetotail lies somewhere between 4 and 8 every month. So, this model is theoretically implemented for all possible number of days, i.e. $f = 0.14,\ 0.17,\ 0.20,\ 0.24,\ 0.27$, with f being the fraction of the Moon's orbit for which it is shielded. Hence, the averaged measurement of the ³He abundance is retrieved for characterizing the solar wind fluence in conjunction with its local incidence.

4.2.2. Spectral Insights of Lunar ³He Abundance

One of the significant influences of the solar wind is the weathering of the regolith. This alters the geophysical and spectral characteristics of the regolith grains significantly. The present study introduces a spectral parametric space for determining the retention hypothesis of the ³He, thereby ruling out the conventional optical maturity based practices (as shown in Figure 10). The advantage of this proposed technique incorporates the contribution of individual space weathering effect on the retained ³He species. Moreover, this provides valuable insights into the proportion of the regolith responsible for engaging the directed ³He ions through either geochemical or physical enrichment bonding process. The spectral trends for modelling the vulnerability of the regolith grains to the space weathering agents are revisited and improved in concordance with reframing the retention terminology. In order to accomplish this, three parameters are utilized: 1578 nm reflectance band (for reduced albedo), continuum slope (for increased reddening), and integrated band depth ratio (for attenuation of diagnostic absorption band depth).

Contrary to employing simple ratio as in Nettles et al. (2011), the present study integrates the UVVIS and NIR spectra of the M^3 data and scales the slope of the straight line passing through them as

$$\mathrm{CS} = \left(\frac{1}{R_{750}}\right)\left(\frac{R_{1500} - R_{750}}{1.5 - 0.75}\right) \tag{4.4}$$

The quantitative measure of continuum slope (CS, in μm^{-1}) for a regolith grain increases with the enhanced exposure time to the space environment. This reflects the inclusion of nanophase metallic iron fragments influencing the spectral behaviour of the grain. Similar to this, another parameter which regulates the reduced Fe^{2+} content and maturation of the regolith is the integrated band depth ratio (IBDR). The utilization of this variable leads to the enhancements of the regions with significant mafic absorptions and hence, in close agreement with one of the space weathering effects. As compared to the conventional single parameter band depth, this ratio facilitates an improved perspective of estimating the mafic absorption band strength as a function of dependent mineral characteristics like composition, grain sizes, abundance and type. The expression of the IBDR is as follows

$$\mathrm{IBDR} = \frac{\mathrm{IBD}_{2000}}{\mathrm{IBD}_{1000}}$$

where

$$\mathrm{IBD}_{1000} = \sum_{n=0}^{38} 1 - \frac{R_{730+20n}}{R_{c_{730+20n}}} \tag{4.5}$$

$$\mathrm{IBD}_{2000} = \sum_{n=0}^{21} 1 - \frac{R_{1658+40n}}{R_{c_{1658+40n}}}$$

In equation (4.4) and (4.5), $R_{c\lambda}$ and IBD_λ represents the continuum reflectance, and integrated band depth at a particular λ nm wavelength of the M^3 data respectively. The reason of selecting 1578 nm albedo band is its capability to exclude the region of space dominated by the ferrous absorptions in both olivine and pyroxene. In addition to the optical properties, the presence of ilmenite governs the retention scenario of the solar wind driven ^3He. This is dominantly mapped in the regions with high TiO_2 content, which can be effectively retrieved by utilizing the correlation algorithm of Shkuratov et al. (1999). The inversion of TiO_2 is quite straightforward in terms of formulating a simple relationship between UV/VIS (415/750 nm) and actual laboratory measurements of the returned lunar samples (Lucey et al., 2000). However, there exists no 415 nm band in the M^3 data, as it starts from 540 nm. Attributing to this, the present study exploits the higher correlation coefficient of the FeO-TiO_2 diagram, specifically meant for the lunar nearside (Shkuratov et al., 1999). The regression equation is given by

$$\log(\omega) = 0.06(\mathrm{FeO}) - 0.54 \tag{4.6}$$

In this, FeO denotes the overall abundance of FeO in wt%, which can be computed by following the traditional origin optimization based approach as stated in Lucey et al. (2000). As part of ^3He mapping, Fa & Jin (2007) have evaluated the ^3He abundance (H in ppb) by associating the OMAT, TiO_2 wt% and solar wind flux (F) with the corresponding data measurements of 25 returned Apollo samples. This yields a linear relation of all the variables, with R^2 of 0.8798, given as

$$H = 0.56 \frac{F\omega}{\mathrm{OMAT}} + 1.62 \tag{4.7}$$

The equation (4.7) is the only basis for comparing and evaluating any newly developed remote sensing algorithm on lunar ^{3}He. Before this, Johnson et al. (1999) have analyzed nine Apollo samples for formulating the global ^{3}He abundance with similar linear regression based relationship as

$$H = 0.000559 \frac{F\omega}{\mathrm{OMAT}} + 2.213 \tag{4.8}$$

Both these studies involve the utility of Clementine derived optical maturity by Lucey et al. (2000) without considering the spectral effects of space weathering. However, the present study focuses on estimating the retained ^{3}He by taking into account the synergistic integration of the discussed aforementioned spectral parameters. This utilizes the high spatial and spectral resolution capabilities of the M^3 data by correlating 61 Apollo and Luna sample measurements of the ^{3}He content. The decrease in albedo (A), spectral contrast and increase in continuum slope attributes to an enhanced deposition of nanophase metallic iron, thereby linking the geological perspective with theoretical retention modelling. Despite this, there is a lack of appropriate knowledge regarding the interrelationship between the individual space weathering parameter and incoming ^{3}He flux. In essence, an attempt is made to assign a particular weight to each of the spectral parameters depending on the achieved correlation with ^{3}He. This can be written in the form of a linear combination as

$$F\omega \left[w_1 \mathrm{CS} + w_2 \left(\frac{1}{\mathrm{IBDR}} \right) + w_3 \left(\frac{1}{A} \right) \right]$$

where

$$\begin{aligned} w_1 &= \frac{R_{\mathrm{CS}}}{R_{\mathrm{CS}} + R_{\frac{1}{\mathrm{IBDR}}} + R_{\frac{1}{A}}} \\ w_2 &= \frac{R_{\frac{1}{\mathrm{IBDR}}}}{R_{\mathrm{CS}} + R_{\frac{1}{\mathrm{IBDR}}} + R_{\frac{1}{A}}} \\ w_3 &= \frac{R_{\frac{1}{A}}}{R_{\mathrm{CS}} + R_{\frac{1}{\mathrm{IBDR}}} + R_{\frac{1}{A}}} \end{aligned} \tag{4.9}$$

where R_{CS}, $R_{\frac{1}{\mathrm{IBDR}}}$ and $R_{\frac{1}{A}}$ are the correlation coefficients of CS, $\frac{1}{\mathrm{IBDR}}$ and $\frac{1}{A}$ respectively, with respect to the ^{3}He measurements of the returned Apollo and Luna samples.

This technique improves the retention framework significantly and hence, could update by itself upon inputting more estimations of the ^{3}He from the future robotic sample return or manned lunar missions. Furthermore, the inclusion of subtle spectral variations provides new insights into the behaviour of retained ^{3}He towards the content of the submicroscopic metallic iron in the agglutinated regolith.

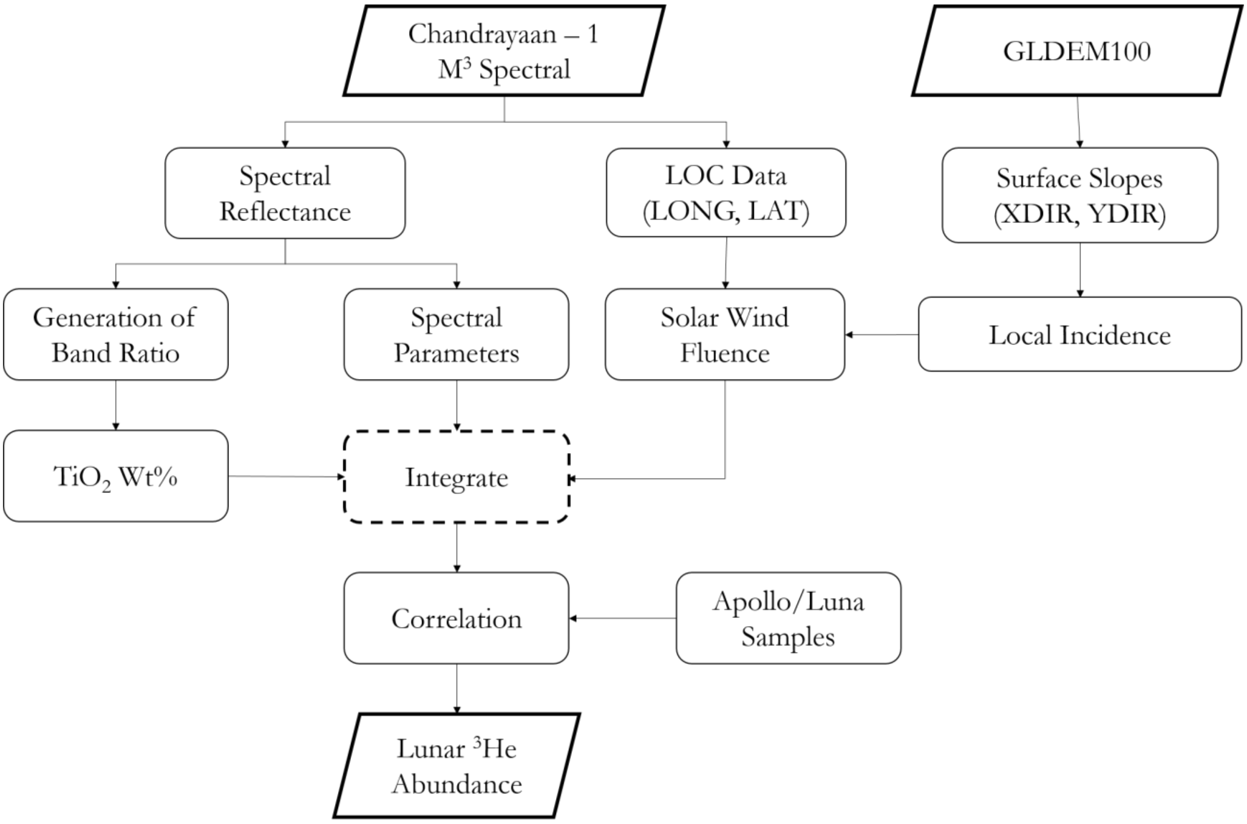

Figure 10: Flowchart of the Chandrayaan - 1 M3 Data Processing.

4.3. Petrophysical Characterization of Lunar Regolith

The interaction of the EM wave with the regolith can be evaluated for subsequent extraction of physical properties, whereby backscattering power is carefully analyzed. This requires an effective utilization of decomposition algorithms for retrieving different scattering patterns from surface/subsurface scatterers. Moreover, the return radar echo also acquires significant information on the electrical and geotechnical properties of the nature of the soil. This further characterizes the radar response based on bistatic angles other than 0°, in case of bistatic radar architecture, thereby deepening the evidence about coherent backscattering opposition effect. The adopted methodology for performing radar data processing is shown in Figure 11.

4.3.1. Retrieval of Scattering Responses: *m-Chi* Decomposition

The decomposition of the radar signal is usually done in order to provide clear discrimination between different scattering patterns occurring within a resolution cell. Moreover, this offers an added advantage of understanding the structural and physical behaviour of individual scatterer to the incoming EM wave. The shape, size, structure and orientation of the scatterer govern the type of the radar response upon interaction. In the lunar context, the gardened and weathered regolith combined with coherent inclusions (like water-ice) offer additional information on the vertical profile of the distribution using polarimetric radar data. The present study utilizes the m-Chi decomposition approach due to its effective characterization of odd bounce and even bounce scattering mechanisms as compared to m-Delta (Raney et al., 2012). In this, the sign of Chi varies for different scattering powers while taking into consideration the handedness of the radar backscatter. The description is given as

$$R = \sqrt{mS_1\left(\frac{1+\sin 2\chi}{2}\right)}$$

$$G = \sqrt{S_1(1-m)} \tag{4.10}$$

$$B = \sqrt{mS_1\left(\frac{1-\sin 2\chi}{2}\right)}$$

where R, G, B represents the even-bounce, volume and odd-bounce scattering mechanisms respectively, S_1 is the first Stokes parameter, m is the degree of polarization and χ is the ellipticity parameter of the polarization ellipse (Raney et al., 2012).

4.3.2. Electrical and Geotechnical Properties

In addition to the scattering component, the polarimetric information also captures the observed physical properties of the regolith grains quantitatively. The sensitivity of the S-band radar signal towards surface roughness and physical parameters is utilized to model the dielectric permittivity and geotechnical features of the lunar soil. This is performed by simulating the radar backscattering coefficient as a function of dielectric constant, RMS height, incidence angle, and correlation length. Moreover, the established quantitative relationship subject to the parametrization of the IEM is evaluated, as per equations (2.10) and (2.11). In this study, the performance of the simulation is assisted by using both Gaussian and exponential correlation functions. It is assumed that the correlation length is equal to the wavelength of the incident radar echo, which is 12.6 cm, due to the unavailable ground data (Fa et al., 2011). The sensitivity analysis is carried out between simulated radar backscatter and physical parameters. This forward simulation trend is used as the training data for the subsequent MLP neural network based inversion. An attempt is made to incorporate the applicability of machine learning algorithm for solving the complex dielectric inversion problem. Usually, the selection of input training data proves to be an important setup for establishing the model. The unnecessary and misleading data is normally discarded in order to avoid confusion for the model while training. Thus, the sensitive parameters to the radar backscatter are carefully examined and extracted for further processing.

The input configuration of the neural network model in remote sensing studies is generally determined as: single frequency multiangle (SFMA), multifrequency single angle (MFSA) and single frequency single angle (SFSA). It is noteworthy that the performance of SFMA and MFSA proves to be better than that of SFSA with no observable difference between both. In this study, the SFMA configuration is adopted for retrieving the angular trend of the data, which is dependent on the surface parameters. However, due to the lack of multifrequency bistatic data for the study site, MFSA is not used. Apart from this, the network topology consists of three input parameters as horizontal, vertical polarized backscattering coefficient (σ_{hh}, σ_{vv}) and incidence angle (θ), one output parameter as dielectric constant (ε), and two hidden layers with 64 nodes each. The choice of the size of hidden layers is made on the trial and error basis with no further network optimization for the current dielectric inversion problem. Moreover, the activation function used is $\tanh$ due to its capability of handling negative inputs and the gradient-based stochasticity of the ADAM optimizer is adopted. The range of parameters (dielectric constant ε, RMS height σ_h, and incidence angle θ) is indicated in Table 2, upon which the sensitivity analysis is performed for generating the training data. The limits are selected based on the typical lunar observation. In the model, 80% of the entire simulated data is used for training while the testing is done on the rest. The performance of the

Table 2: Sensitivity Range of Parameters for IEM and MLP Neural Network based Inversion Modelling.

Parameters	Lower Range	Upper Range	Step Size
ε	1.5	12	0.05
σ_h cm	0.05	5	0.05
θ deg	0	85	5

model is evaluated on the basis of the achieved coefficient of determination (R^2). Furthermore, upon achieving satisfactory results from the simulated data, the horizontal and vertical components of the MiniRF S-band bistatic CTLR data are fed into the network. Before the operation, the images are normalized with respect to the local incidence angle in order to accommodate the topographical changes. The local incidence angle is estimated for the acquired incidence angle of 57.5°, as per equation (4.1). Essentially, the conversion of fully polarimetric quad pol scattering matrix into the Stokes parameters for circular transmit, and dual linear receive polarizations results in the identical derivation of hybrid pol Stokes parameters (Raney et al., 2011). Hence, this approach is followed to include the horizontal and vertical components, from MiniRF Stokes parameters, as the testing data. The retrieved dielectric constant of the regolith is used for estimating the geotechnical properties, which includes bulk density, loss tangent, porosity, void ratio, and relative density, as per described equations (2.13)-(2.17), respectively. All these petrophysical properties are later analyzed and integrated with the abundant solar wind ^{3}He deposits, thereby providing a unique perspective of reformulating the retention hypothesis.

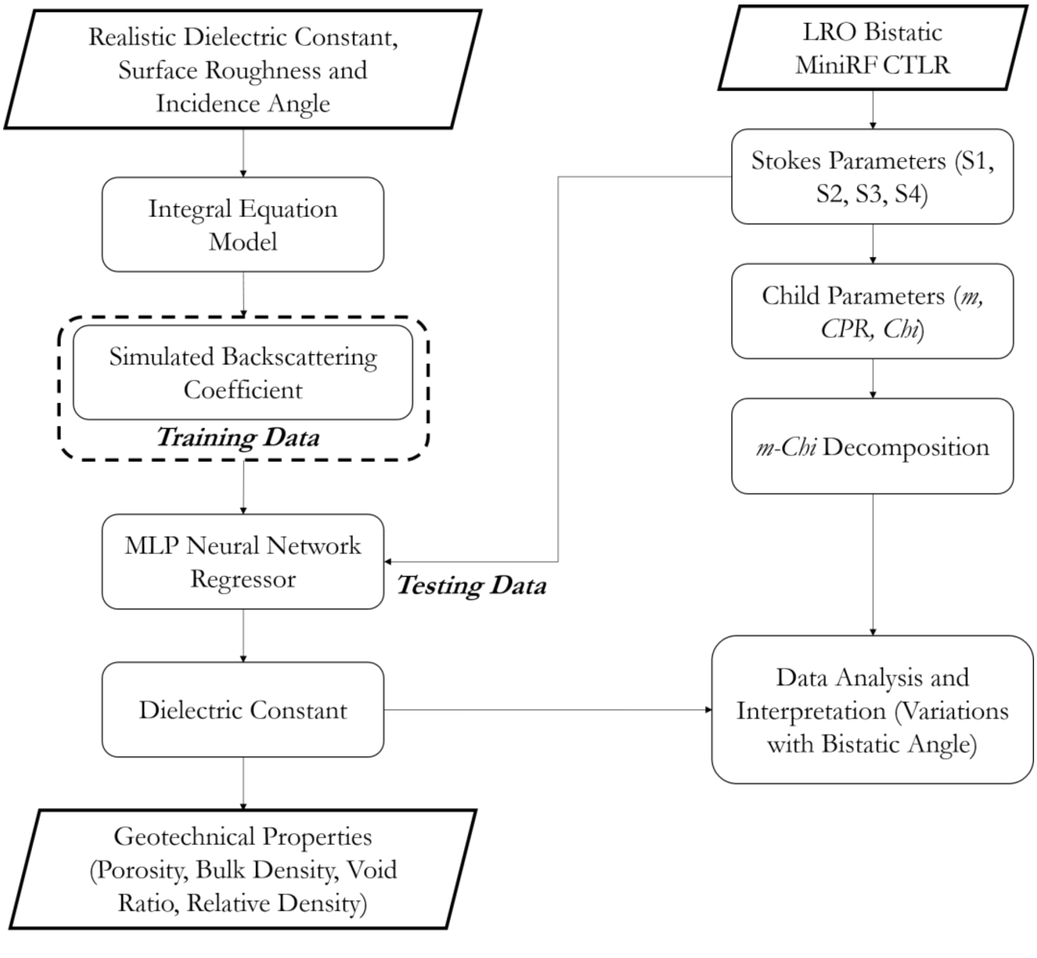

Figure 11: Flowchart of the LRO MiniRF Data Processing.

4.4. Multisensor Data Analysis, Interpretation and Validation

The quantitative retention framework is established by performing the multi-sensor data analysis in terms of integrating the solar wind implanted ^{3}He contents and petrophysical characteristics of the lunar regolith. This observation is further subjected to qualitative interpretation based on the existing geological manifestations of the associated space weathering impacts on the Moon. In essence, the detailed understanding of each segment in the research would provide a future mining perspective of the accurately geo-located ^{3}He reserves.

4.4.1. Modelling Spatial Orientation: Variogram Analysis

The concentration of the ^{3}He content with respect to the depth profile can be assessed by incorporating the regolith thickness from elevation h. Assuming the thickness of the mare and highland as 8 m and 15 m, the global vertically distributed ^{3}He content is found to be 4.5×10^8 kg following an exponential depth profile (Swindle et al., 1990). Similar to this, another estimate suggests the distribution of ^{3}He to be uniform with respect to depth with an overall global repository of 8.4×10^8 kg (Fegley & Swindle, 1993). The gardened regolith accommodates the implanted ^{3}He up to several depths due to the blending of the regolith grains with actual surficial retention. This leads to the enrichment of the solar wind ^{3}He into the deeper regolith. Essentially, the regolith is more intensive near the surface due to the agglutinated grains and impact melt deposits, which gradually decreases with depth. This further illustrates the exponential decaying ^{3}He profile with respect to depth, $C(z)$, as described in section 2.2.2. Quantitatively, the distribution of ^{3}He at a given location (H_d) is a function of regolith thickness (d) and bulk density of the regolith with depth, $\rho(z)$ as

$$H_d = \int_0^d \rho(z)C(z)\,dz$$

Where

$$\rho(z) = 1.92\frac{z + 12.2}{z + 18} \tag{4.11}$$

$$d = 9.5 + 8.5\tanh\left(\frac{h + 1200}{1632.5}\right)$$

In addition to the decaying function, the uniform vertical distribution can also be assumed by negating the exponential function of the $C(z)$. Subsequently, the spatial component is added by determining the orientation of ^{3}He. This provides an estimate for spatial variability between the sampled points at various ranges in the form of variogram analysis. Depending on the samples, empirical variogram is generated for the spatial distribution of derived solar wind ^{3}He per unit area. In total, 8000 spatially referenced points are randomly selected from various locations, covering the entire image. All these samples along with their geographical locations, in Equirectangular map projection, are converted into data frame before using it for further analysis. Since the Moon projection system is not supported in the spatial data frame, the selenographic coordinates are manually provided in the customized data frame. Moreover, the directional component is introduced in the analysis by considering the variability of the ^{3}He samples along 0°, 45°, 90° and 135°. Along with this, an interactive map is produced for qualitatively evaluating the directional orientation of the spread. The analysis further utilizes different variogram models to ensure the most appropriate fit to the empirical variogram, thereby facilitating the directional ^{3}He abundances for future lunar mining operations.

4.4.2. Comparison of Multisensor Data

The random sampling strategy is adopted for the research based on characterizing the ^{3}He abundance and petrophysical content of the regolith. The prime focus is on the Aristarchus plateau signifying various features ranging from ejecta cover to pyroclastic deposits. Moreover, different samples of 250 pixels each are selected from two particular zones: High ^{3}He and Low ^{3}He. Along with this, distinct sets of samples are attributed to the pyroclastic/non-pyroclastic deposits north of the Cobra head and the extended ejecta cover mantling the Herodotus crater floor. Based on the sample sets, transects are created by plotting the petrophysical contents and corresponding ^{3}He measurements for observing any dependability of the former on later. This also predicts the behaviour of the weathered soil towards the retention scenario of the ^{3}He. In addition, the comparison of multi-sensor data products is carried out by graphically portraying the spatial site and variability of the retrieved features. An attempt is also made to quantify the spatial variability of the dependent variables (^{3}He and petrophysical properties) in terms of modelling cross-variograms. Such analysis could provide new insights into the possible association of the regolith characteristics with chemically/physically retained ^{3}He for performing future mining operations.

4.4.3. Validation

The processed results are supported by correlating with the procured laboratory assisted in-situ documentation of ^{3}He measured for the returned Apollo and Luna samples. The readings of the estimated ^{3}He content (in ppb) are analyzed with the corresponding data derived measurements of the Apollo and Luna landing sites. The quantitative representation is through estimating the coefficient of determination (R^2), root mean squared error (RMSE), mean absolute error (MAE), and index of agreement (d_i). The aforementioned statistical indices are explained as follows

$$\mathrm{RMSE} = \sqrt{\frac{1}{N}\sum_{i=1}^{N}(x_p - x_o)^2} \tag{4.12}$$

$$\mathrm{MAE} = \frac{1}{N}\sum_{i=1}^{N}\left|x_p - x_o\right| \tag{4.13}$$

$$d_i = 1 - \left[\frac{\sum_{i=1}^{N}(x_p - x_o)^2}{\sum_{i=1}^{N}\left(\left|x_p - \frac{1}{N}\sum_{i=1}^{N}x_o\right| + \left|x_o - \frac{1}{N}\sum_{i=1}^{N}x_o\right|\right)^2}\right] \tag{4.14}$$

where N is the number of observations, x_p is the predicted variable and x_o is the observed variable. In (4.14), d is expressed from 0 to 1, representing the least match or no agreement between the predicted and observed entities for the former whilst perfect match for the latter (Willmott, 1982). Despite this, the simulation of the radar backscatter using IEM and inverted dielectric content are validated with the MiniRF and published in-situ data, respectively.

4.5. Summary

This chapter summarizes the adopted methodology of the research in conjunction with data processing, analysis and interpretation techniques. The retention hypothesis of the solar wind implanted ^3He is formulated based on the spectral parametric model, thereby capturing subtle details of the weathered spectra influenced by the local maturation and chemistry. On the contrary, the sensitivity of the radar backscatter is simulated from IEM, which is fed as the training data in the MLP Neural Network inversion model. This is tested upon the MiniRF bistatic data, through which geotechnical properties are retrieved. Finally, the chapter provides an overview of the multi-sensor data comparison by adopting variogram and transect analysis along with validation methods.

5. RESULTS AND DISCUSSION

This chapter deals with processed results and corresponding analysis of the multi-sensor data for revisiting the retention hypothesis of the ^{3}He, which depends on the observed space weathering effects, spatial orientation and petrophysical content of the lunar regolith. The significance of the chapter provides new insights into data processing and validation techniques for retrieving the desired ^{3}He content at the study site, thereby aiding pre-sampling strategies for ISRU technologies.

5.1. Estimation of Solar Wind Implanted ^{3}He: Implications for In-situ Lunar Mining Operations

The spectral data of the Chandrayaan-1 M^3 instrument is utilized for retrieving the ^{3}He content and hence, contribute to the understanding of complex space weathering processes. The adopted methods are implemented for modelling the normalized solar wind flux, ilmenite abundance, and spectral parametric space involving the weathering effects on the lunar soil. This further explains the possible quantification of ^{3}He reserves while critically examining the spectral behaviour of the regolith. The validation is carried out by correlating the estimated ^{3}He from the proposed technique and in-situ laboratory measurements. In this regard, the spatial distribution of the retained ^{3}He could specifically identify prospective mining candidates in the nearby vicinity of the study site.

5.1.1. Distribution of Normalized Solar Wind Plasma

The variations in the solar wind plasma distribution across the lunar regolith are theoretically modelled using equations (4.1)-(4.3). According to the model, the flux substantially increases from higher latitude regions to midlatitude equatorial areas due to the higher incidence angle of the solar wind plasma near the poles. Moreover, the Earth's magnetotail shielding avoids the nearside to receive more plasma flux than the farside. Considering the plasma fluence on a local scale, the mechanical influences, like directional slope component and varying regional topography, play a key role in reducing the model uncertainties. This further quantifies the flux to a realistic estimation, thereby increasing the reliability of the model.

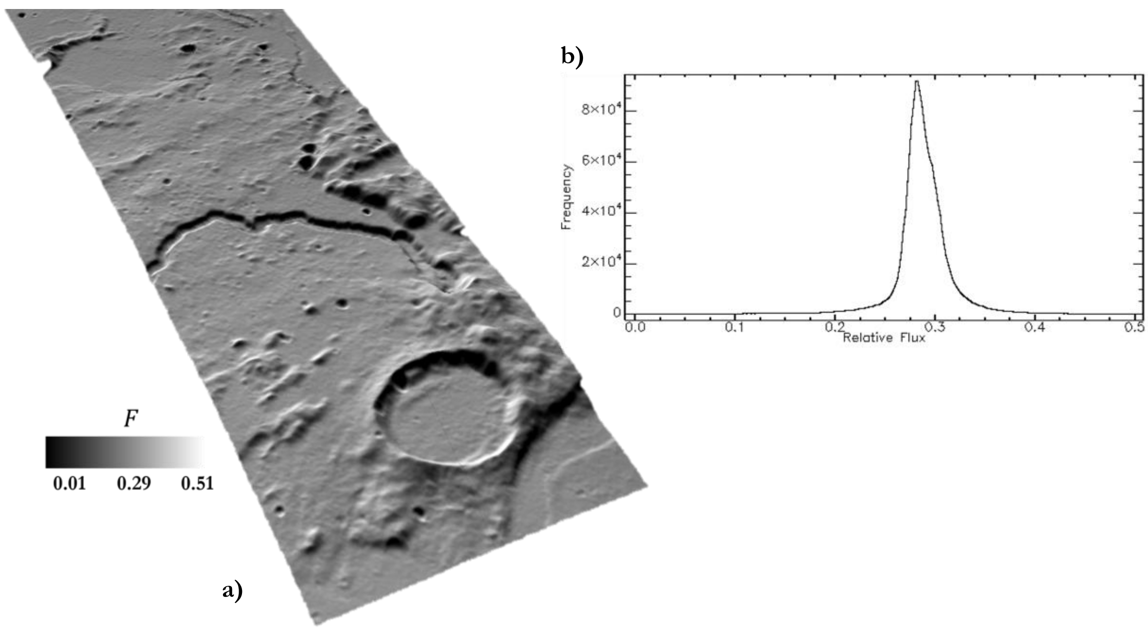

Figure 12: a) Solar wind plasma flux, normalized with respect to local incidence angle, in the Vallis Schroteri region, and b) Frequency distribution of the plasma fluence.

The estimation of the plasma flux is, therefore, normalized to the local incidence angle of the nearly parallel solar wind plasma flow along with considering all possible number of shielding days. This averaged product essentially represents the most probable estimates of the normalized plasma flux occurring at a particular region, wherein the magnetosheath effects are incorporated in detail. From Figure 12(a) the sites near the Cobra Head feature and Herodotus crater receive an increased fluence of about 40%, thereby marking the regolith resources for subsequent ^3He mapping. Several highly sloped terrains exhibit reduced plasma flux content adjacent to the areas having relatively larger accumulation. This may be possible due to the opposite orientation of the slope facet with respect to the incident solar wind flow, thereby making it deficient of the flux particles. Moreover, the floor of the bowl-shaped microcraters near the vicinity depicts almost negligible flux amounts than the walls. This attributes to the higher glancing of the plasma while interacting with the regolith, whereby the particles escape the floor and hit the walls directly. Also, the minimum proportion of the reported plasma flux for a particular resolution cell is always received for any of the possible shielding scenarios.

In addition, the estimated plasma flux across the plateau appears to be normally distributed, wherein the associated uncertainty is represented by a standard deviation of 0.03. Moreover, the most probable relative flux value in the frequency distribution is found to be 0.29. The concerned histogram of the plasma fluence is shown in Figure 12(b). Upon emphasizing on the influence of local topography on the flux distribution, significant findings are drawn. The percent change of the modelled flux reading with and without topographical constraint is somewhat surprising: a region tends to receive more than 47.34% of the modal plasma flux when the local incidence is not considered. This trend provides an overestimation of the relative flux, thereby associating inaccurate retained ^3He measurements. The normally distributed percent change exhibits the standard deviation of 5.47%, which defines the uncertainty. In principle, the plasma particles incident on the surface with an effective velocity, which in turn depends on the orientation of the surface facet. The more the angle of orientation, the lower the chances of particles getting accumulated behind the facet. Hence, the inclusion of the local topographic effect needs to be accounted for producing realistic retention maps of the ^3He. It seems logical to assume the prospective ^3He sites near the Cobra head feature based on the higher exposure of solar wind plasma. However, the concentration of the ^3He may reach a saturation point, wherein the uncertainty is introduced in the measured abundance. In essence, other key proxies are to be evaluated for understanding the effective retention of solar wind ^3He along with ground measurements of the Apollo and Luna landing sites.

Generally, the distribution of the solar wind volatiles, other than ^3He, is directly proportional to the solar wind exposure, provided the random large-scale variations in the local impact history is assumed. This is mainly because the retention of these species is independent of soil chemistry. In Figure 12(a), the soils receiving higher flux nearly represent the abundant non-^3He solar wind volatiles, without accounting the saturation effect. However, for effectively mapping the ^3He reserves, local soil characteristics are to be considered.

5.1.2. Abundance Mapping of Ilmenite Mineral

One of the most important factors towards defining the amount of implanted ^3He that can be retained is the ilmenite mineral abundance. It can be appropriately mapped by determining the TiO_2 content of the lunar soil. The high spectral and spatial resolution capabilities of the Chandrayaan-1 M^3 data is utilized to quantify the TiO_2 mineral abundance in wt%. The spatial distribution of the TiO_2 is estimated by using the equation (4.6), thereby eliminating the usage of 415 nm band. As shown in Figure 13, the entire region is characterized by low Ti content between 0.07 to 2.08 wt%. This trend nearly follows a normal distribution with a standard deviation of 0.09 wt% and modal abundance of 1.75 wt%. The lower proportions of Ti may attribute to extensive mantling of the regolith by mafic pyroclastic glass beads.

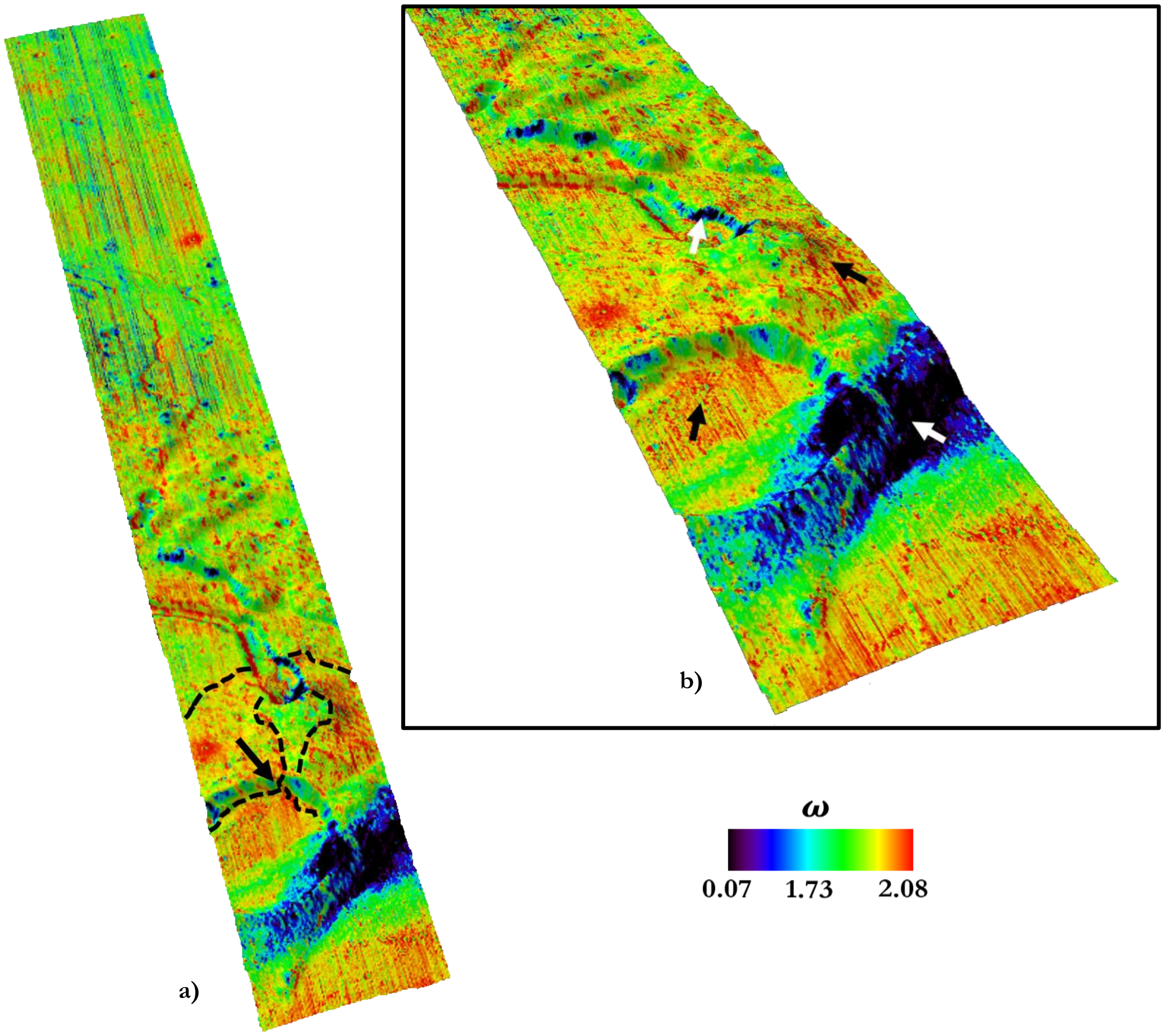

Figure 13: TiO_2 Mapping of the Vallis Schroteri region. a) Black arrow represents the possible lava fan location, while the black dotted line shows the possible spatial distribution of the Ti content. b) White arrows depict the low TiO_2 content (in wt%), while black arrows represent high TiO_2 region.

In the vicinity of the Cobra head feature, the regolith is mainly composed of iron-rich orange glass with a much lower content of TiO_2, which is indicative of a pyroclastic fountaining event in the past. The resemblance of the glassy and crystalline beads with Apollo 17 soils is significant, thereby attributing to the intrinsic variations across the regolith. These pyroclastic deposits are found to be associated with primary source vent of the region, i.e. Cobra head. Moreover, the fine-grained and quenched spheroids produced during the early release of gas-rich magma from the vent result in possible accumulation of low Ti regoliths. In the regional context, the white arrows are an evident source of very low Ti content, while the relatively higher concentrations are denoted by black arrows, as shown in Figure 13(b). The dominant part in the former category is the complex ejecta of the Aristarchus crater, which attributes to mixed proportions of the mare and highland composition along with impact melt deposits. This produces a distinctive spectral contrast with the background, wherein the intermediate grade surrounds these deposits. The medium TiO_2 level in the floor, represented in cyan to green colour, is found to be created through impact mixing of the low Ti and high Ti basalts. Moreover, the higher Ti content of the Herodotus crater floor is emplaced by the ejecta cover, thereby possibly explaining the early formation process of the crater. From Figure 13(a) the near-radial spatial trend of the high Ti content from the source vent follows a downward distribution pattern with the black arrow representing the possible inflow of the eruptive magma through the lava fan into the crater floor. The intermediate phase of the TiO_2 encircled within the black dotted lines may be caused due to the dilution of the Ti levels from the emplaced low Ti pyroclastic glass beads and breccias during the eruption. The pyroclasts further preserve the volatiles by encompassing within its granular structure and hence, proves to be prospective candidates in retaining ^3He. However, the association of such behaviour with the less mature Apollo 17 soil depicts lower ^3He abundances. This is supportive of using local maturity measure in conjunction with TiO_2 content for improving the correlation, as evident in Figure 4.

5.1.3. Incorporating Space Weathering Trends into Optical Maturation

Following the discussion in the previous section, the study site now features the pyroclastic regions as the most suitable mining candidates. The maturity variations across the regolith are however left for further examination. In this regard, the spectral parameters are computed based on their applicability towards quantifying the three individual space weathering effects of the lunar soil. As per equations (4.4) and (4.5), the alterations in the reflectance spectra are modelled and compared for determining the maturity trends of the soil. Figure 14 shows three prominent spectral attributes for exhibiting the darkening, reddening and reduced spectral contrast of the regolith. The CS image provides evidence of agglutinates during the interaction of space weathering agents with the surface, thereby indicating an increased reduction of Fe^{2+} into nanophase metallic iron particles. It is found that the maximum slope occurs in the pyroclastic regions, depicted by red colour. The pyroclasts are widely interpreted as volatile-rich glasses, which usually alters the recorded spectra similar to that of the mature soils. Moreover, the walls of the Herodotus crater and Vallis Schroteri appears similar to have low values of CS. Several other features over the Agricola Mountains and those lying within proximity to the rilles also represent significant decrement in the continuum slope parameter.

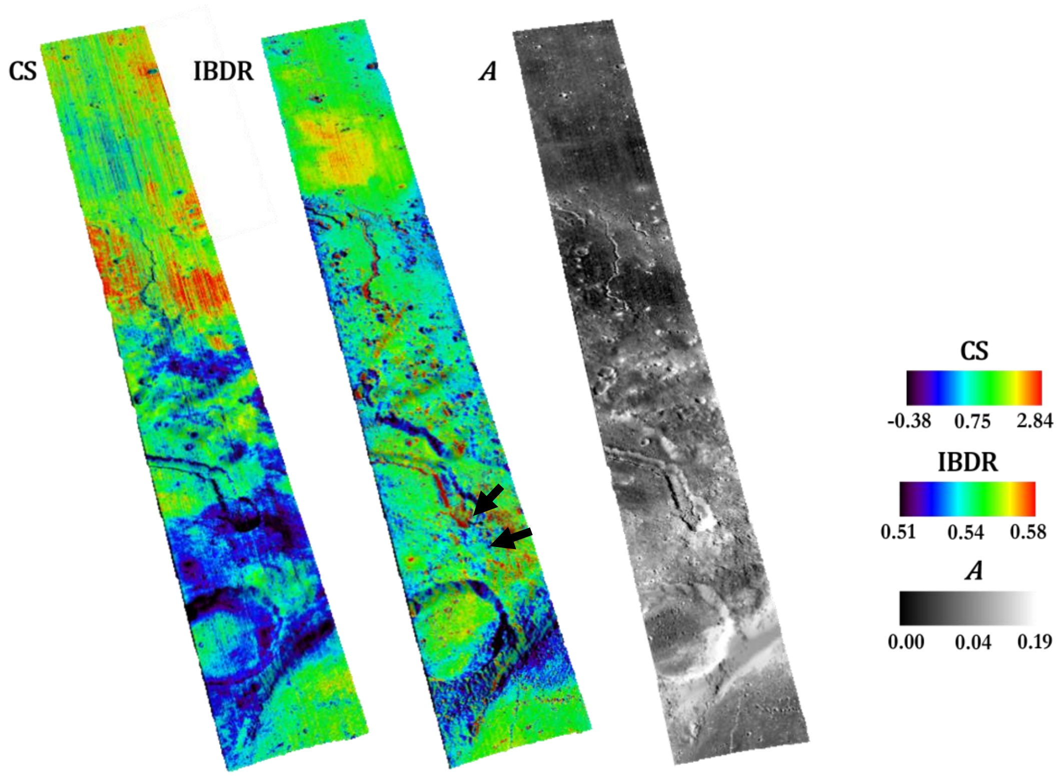

Figure 14: Spectral representation of the space weathering effects. CS, IBDR, and A denotes Continuum Slope, Integrated Band Depth Ratio, and Albedo respectively.

This usually occurs due to the deposition of the immature material on the surface by either mass wasting or local impact events. Hence, both local maturity and pyroclastic content in the soil govern the CS measure. Meanwhile, the shadowed walls of the Vallis Schroteri (marked by black arrows in IBDR image) appears to show erratic behaviour towards 1000 nm and 2000 nm absorption. In this way, it overestimates the absorption content, thereby implicating reserves of mafic minerals. The spectra, however, supports this random occurrence as it differs significantly from the surrounding regions. Also, the floor of the Herodotus crater is characterized with medium to high level of IBDR, which accounts for 37.74% in the spectral alteration process of the soil by space weathering agents. Moreover, the least dominant factor contributing to the production of nanophase iron is CS with 24.59%. This has a broader implication of the weathered regolith to be directly linked with the presence of mafic lithologies. Looking at the spectra, there is an absorption dip at 1000 nm associated with minor absorption features at 2800 nm. This is indicative of olivine deposits subject to hydration; however, the spectral dip of the unweathered olivine-rich regolith grain appears to be more prominent at 1000 nm. Due to the major contribution of IBDR in the Herodotus floor, the absorption dip of olivine deposits is found to be suppressed than usual. Similarly, a major portion of the ejecta blanket is devoid of mafic signatures. The distribution of the ejecta regolith proximal to the Herodotus crater appears to contain hydrated olivine inclusions within the grain, especially E3 and E8 in Figure 15. This attributes to the gradual increase of olivine content towards the crater. Interestingly, notable absorption features are found near 2800 nm, which confirms probable deposits of hydroxyl ions in the nearby vicinity of the ejecta cover. The association of the nominally anhydrous olivine mineral with hydroxyl signatures attributes to the possible magmatic origin of the hydration of subsurface affinity.

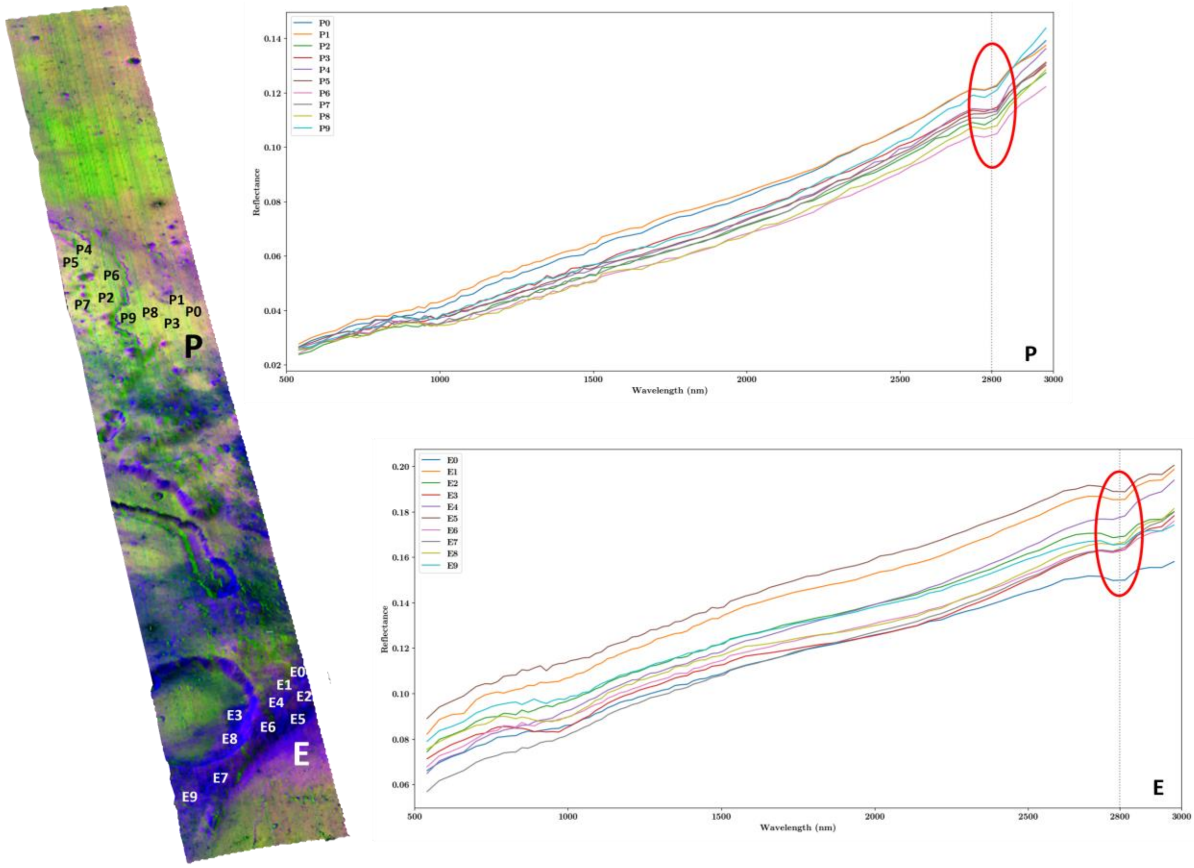

Figure 15: False Colour Composite of the Vallis Schroteri Region. R: CS, G: A, B: IBDR, with G and B inverted. In the image, P is representing the Pyroclastic Region and E is the ejecta blanket. Associated spectra are depicted for the corresponding marked regions. Red circles denote 2800 nm absorption feature in the spectra.

However, the role of exogenic factors comes into play while examining strong 2800 nm absorptions in the spectra extracted from the anorthositic regoliths and pyroclastic glasses, as shown in Figure 15. The darker tone of the lunar features reveal the immature nature of the soil, which is evidently delineated in the ejecta cover, patches surrounding the Cobra head, and several microcraters. This trend essentially showcases the dominance of albedo channel relative to others (as the green band is inverted). Moreover, smaller variations in the reddening of the soil induced with larger changes in the albedo and IBDR are denoted in magenta colour. The combination appears to be surprisingly high in the floor of the Vallis Schroteri, suggestive of intense Fe^{2+} content in the granular wall of the grains. This also relatively makes the surface slightly mature as the crystallographic structure of the grain enlarges. Such behaviour can attribute to the misclassification of the minerals as the absorption band depths tend to alter significantly. In addition, the yellow tones are indicating the higher band depth ratios as compared to albedo and continuum slopes. The pyroclastic region (P) captures most of this effect with 48.11% contributing to the attenuation of mafic absorption band depths. In certain sub-regions, there are prominent deposits, denoted in green tints mixed with yellow colour, exhibiting the strong signature of nanophase iron particles produced during the vaporization of iron-bearing mafic minerals. This is further confirmed by the proportion of CS in the regional pyroclastic soils, which is 40.18% along with others. As evident from the spectra, the pyroclasts appear to show strong hydroxyl presence, which may signal towards endogenic sources. It is believed that the pyroclastic regoliths contain tiny patches of water in the glass beads of deep mantle affinity and hence, provides a unique exploration site as compared to the immediate surroundings. However, along with ^{3}He, the solar wind also carries abundant protons that interact with the electrons in the lunar soil, thereby producing a neutral hydrogen atom. Subsequently, the atom often gets latched to the free oxygen atom from either silicic regolith or concomitant release during reduction of Fe^{2+}. Hence, the quantitative estimates of the combined three spectral parameters could be utilized for determining the amount of oxygen produced in conjunction with solar wind proton implantation.

The equal contribution of the continuum slope and band depth ratios towards weathering of the soil are prominently visible in green colour. Several regions surrounding the source vent depict such behaviour, attributing to the pronounced decrement in the absorption feature near 1000 nm. Due to the past explosive pyroclastic eruptions near the vicinity, there is a slightly decreasing absorption trend near 2800 nm in the anhydrous and weathered olivine spectra. Moreover, the top portion of the image depicts a larger area with evident signs of greenish yellow colour. This indicates that the influence of IBDR is comparatively higher than CS in affecting the local maturity trends due to micrometeorite impact, solar wind, and galactic cosmic rays. From the spectral analysis, it is established that the maturity trends in the lunar features are not uniform, instead tend to change with respect to each of the individual weathering effects. Furthermore, the magnetospheric shielding of the study site from the solar wind provides lower proportions of spectral alterations caused due to solely plasma particles. It can be, thus, concluded to mark another region of interest, i.e. ejecta cover due to hydration features, along with pyroclastic regoliths for subsequent solar wind ^{3}He mapping and future mining operations.

5.1.4. Retention of Solar Wind ^{3}He: Implications for Lunar Outposts

The distribution of ^{3}He across the regolith depends on the incident solar wind plasma supply and local chemical variations of the soil. Generally, the Lucey OMAT parameter is used for defining the optical maturity relative to the exposure age of different regolith features. However, the present study employs the spectral characteristics of the soil for understanding the contribution of a particular space weathering trend toward ^{3}He retention. This critically reviews the observed local maturity variations while capturing the subtleties present in the regolith grains. Moreover, the retention hypothesis of the ^{3}He can be well elaborated based on specific soil behaviour and reduced Fe^{2+} content. The demarking of the regions with ^{3}He abundance could provide new insights into potential weathered entities of the soil responsible for solar wind volatile retention. This could also develop a conceptual framework of distinct spectral alterations originating from the implanted solar wind species.

From section 2.2.3, it is established that there is a statistical significance between ^3He, maturity, ilmenite content, and solar wind fluence based on the returned Apollo/Luna samples. In this, the spectral indices are utilized to redesign and associate the complicated space weathering processes with incoming plasma stream and local ilmenite proportions. The production of nanophase iron particles within the accreted granular rims and agglutinates enhances with the decrease in albedo and spectral contrast. However, the prolonged exposure of the regolith to the space environment increases the redness of the soil, i.e. continuum slope. During the micrometeorite impacts, the sputtered products from the nearby regolith grains undergo re-deposition, thereby increasing the size of an individual grain. Moreover, the implantation of the solar wind gases into the soil could be strongly linked to an already occurring space weathering process. This leads to developing an effective retention framework, as mentioned in section 4.2, wherein the influence of an underlying surface process is considered. Following the correlation with ^3He, the spectral parameters are extracted from all the available 61 Apollo/Luna sample sites through astronaut traverse maps. Additionally, the corresponding measurements of the modelled plasma flux and TiO_2 wt% are retrieved. Subsequently, a new hybrid parameter FTC/IA is generated based on the sequential space weathering processes in concordance with ^3He retention. Figure 16(b) describes two scenarios: fitting the regression line with and without averaging of the samples. The analysis of the former shows a significant correlation between the hybrid parameter and in-situ ^3He, as compared to the latter. The spatial extent of the returned samples from a landing site is necessarily small, wherein the ^3He variations could be assumed minimal.

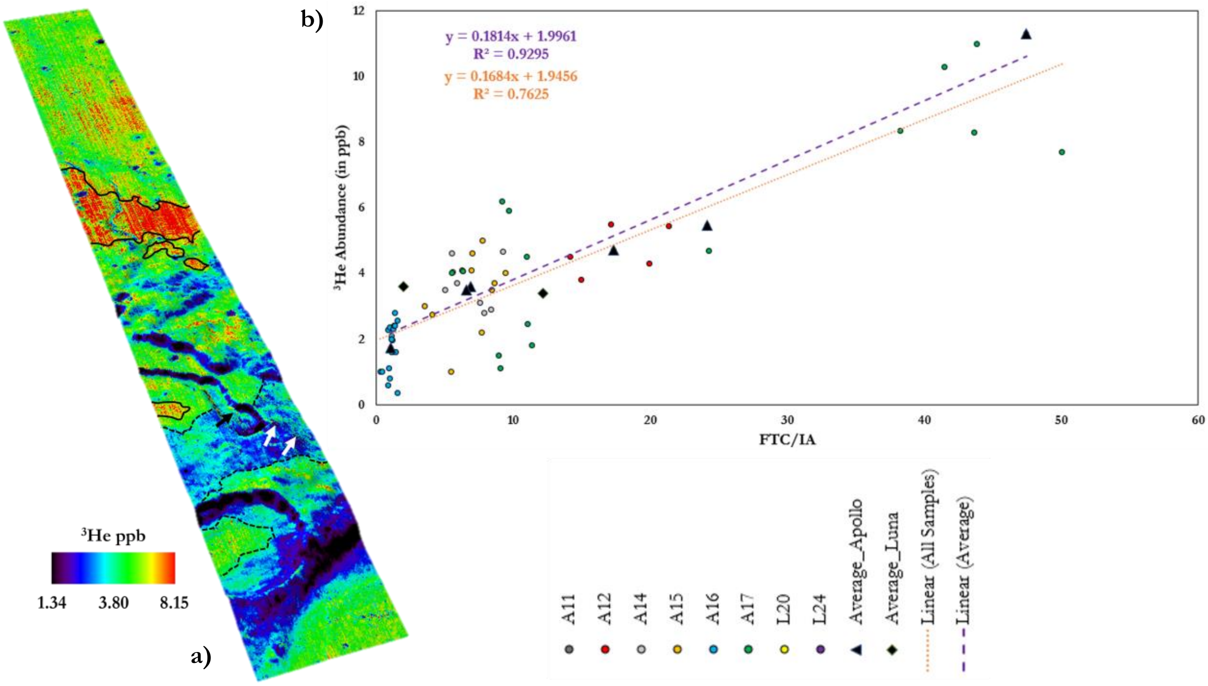

Figure 16: a) Retained ^3He in the Vallis Schroteri Region. The solid black line is denoting the high ^3He abundance whilst the dotted black line is delineating the medium ^3He abundant regions. b) Comparison of FTC/IA with in-situ ^3He content. The purple fitted regression line represents the averaged sample measurements whilst the orange line is fitted to all 61 samples. Note that no dependency between the space weathering processes is considered.

Hence, the irregular distribution of the samples in the plot may attribute to the possibility of measurement bias. In order to minimize this, averaging of the samples within each site is performed, which reflects a higher correlation coefficient of 0.93. The obtained regression equation is applied to the study site under investigation. Figure 16(b) depicts the characterization of the regolith for solar wind implanted ^{3}He. The most abundant regions come out to be pyroclasts with >7.3 ppb of ^{3}He in concentration. Moreover, the floor of the Herodotus crater shows significant diversity in the ^{3}He abundance. The central portion observes medium to high concentration while the spatial extent mantled by ejecta cover essentially represents a much lower content of ^{3}He. Few hotpots of higher abundance are marked, which are strongly associated with reduced mafic absorption band depths compared to the unweathered regolith grains. Also, the sites over the top of the Agricola Mountains exhibit the higher redness of the continuum slope. An interesting trend is observed in the distribution: the soils with sufficiently larger band depth ratios and continuum slopes retain most of the implanted ^{3}He. This is evident in the outer vicinity of the Cobra head feature with about 57.92% of albedo, wherein the presence of irregular-shaped mineral fragments reduces the retention capabilities of the soil. Furthermore, in such cases, the size of the welded aggregates tends to be larger, implicating to a much smaller surface area for an incoming solar wind ^{3}He to get retained. Despite relatively higher ilmenite content, the albedo trends suppress the regolith and makes it less retentive. It is also observed that the ejecta cover represents the lowest amount of ^{3}He, about <1.45 ppb, mainly because of the highland materials in the immature grains mixed with impact glasses and sufficiently lower ilmenite content. Quantitatively, about 68.42% of the weathering processes contribute to the gradual darkening of the ejecta regolith. As reddening spectral effect is controlled by pyroclastic estimates, the regoliths with significant CS value retains higher ^{3}He content.

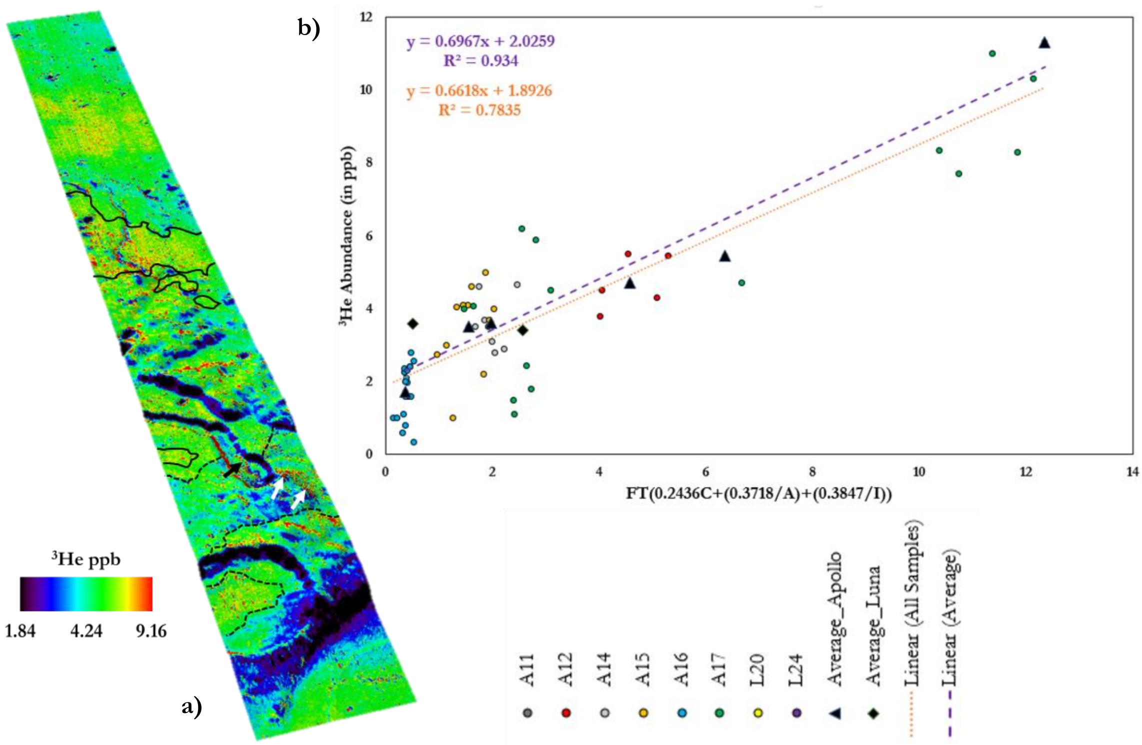

Figure 17: a) Retained ^{3}He in the Vallis Schroteri region. The black line is denoting the moderate to high ^{3}He abundance. b) Comparison of weighted averaged hybrid parameter with in-situ ^{3}He content. The purple fitted regression line represents the averaged sample measurements whilst the orange line is fitted to all 61 samples. Note that inter-dependency between the space weathering processes is considered.

In the aforementioned retention framework, it is assumed that the space weathering effects are independent to each other and hence, contribute no cross-dependency between them. However, in a practical case, this doesn't hold. Following the weighted average approach as described in section 4.2.2, the quantification of the retained ^{3}He is made by assuming the inter-dependency of the spectral alterations. The achieved correlation coefficients of the spectral indices with in-situ ^{3}He measurements are as follows

$$R_{\mathrm{CS}} = 0.3962$$

$$R_{\frac{1}{\mathrm{IBDR}}} = 0.6299 \tag{5.1}$$

$$R_{\frac{1}{A}} = 0.6083$$

In linear combination, the primary condition is that the sum of the weights should be equal to 1. Hence, the respective weights are computed from the correlation coefficients and inserted in the equation (4.9) as

$$F\omega\left[0.2424\mathrm{CS} + 0.3854\left(\frac{1}{\mathrm{IBDR}}\right) + 0.3722\left(\frac{1}{A}\right)\right] \tag{5.2}$$

where

$$w_1 = \frac{0.3962}{1.6344} = 0.2424$$

$$w_2 = \frac{0.6299}{1.6344} = 0.3854 \tag{5.3}$$

$$w_3 = \frac{0.6083}{1.6344} = 0.3722$$

This provides a new perspective on the dependent contribution of the complicated space weathering trends. In principle, about 24% of the lunar soil with enhanced reddening is responsible for the retention of loose ^{3}He ions. The decrease in the mafic absorption band depth and albedo is strongly aligned with the ^{3}He implantation. Similar to the previous approach, the correlation between equation (5.2) and in-situ ^{3}He measurements is performed. This yields a higher correlation than the earlier version, as shown in Figure 17(b), thereby highlighting the interdependent weathering component in lunar ^{3}He estimation. Moreover, the weights get updated for each of the returned samples, improving the mapping criterion. After applying the regression equation to the study site, the region is found to be characterized by a modal ^{3}He abundance of 5.365 ppb. The pyroclastic regoliths of higher ^{3}He concentration show an underestimated local trend for specific sub-regions in the weighted average approach. It is seen that the abundance avoids the abrupt shift of values in the regions separated by solid black lines. In such vicinity, the contribution of weathering processes becomes additive in nature with a particular assigned correlation weight. However, the product of spectral parameters in the previous approach introduces a negation factor that could be important when any of the processes undermine the retention. The problem is more evidently marked near the Cobra head where the relatively immature regolith accommodates higher albedo relative to CS and IBDR. This gives overall reduced retention since it is inversely proportional to the ^{3}He abundance and other contributions are negated somewhat. Moreover, the distinct dotted black boundary separating the lower abundant regions is exhibiting the change of the regolith composition in terms of Fe^{2+} content. If the agglutinates are formed more frequently associated with soil grains, the retention of ^3He is likely to be influenced and hence, lessens the concentration. Therefore, the diverse variability of the weathering trends is linearized for incorporating the suppressed effects other than the predominating factor for the corresponding soil. This provides a new image with more regularly distributed ^3He across the regolith. Figure 17(a) illustrates the possible implanted zones with higher abundance near the Cobra head feature and pyroclastic deposits. The white arrows reveal localized hotspots, which are decidedly less distinguishable in Figure 16(a). One of the reasons is the ubiquitously scattered bright-highland materials governing the regolith without taking into account the attenuated mafic absorption band depths and reddened continuum slopes. However, there are few regions enhanced in IBDR image with red colour possibly representing additional mounds near the source vents and hence, captures the olivine signature of mantle affinity. These features are also found to be ilmenite-rich, thereby complying ^3He-rich regolith. Therefore, the almost equal contribution of CS and IBDR is improved due to the inclusion of correlation weights.

The ejecta blanket mantling the olivine-rich regolith of the Herodotus crater shows a similar response of lower ^3He abundance in both models. Apart from this, the floor of the primary rille proximal to the Cobra head depicts a surge in abundance (black arrow). This is probably due to the alterations in the strength of absorption dip near 1000 nm between the inner rille and primary rille. The associated mafic band depth ratio is increased near the inner rille, as shown in Figure 14, with strong signatures of ilmenite. Moreover, the least significant effect is the reddening of the slope, which contributes about 31.77% in total. The lower abundance of retained ^3He, particularly near the inner rille, is attributed to unsurprising high albedo and immature regolith in Figure 16(a). However, the minor subtleties due to other weathering effects are incorporated to resolve the quantitative solar wind ^3He mapping in linear combination approach. In addition, all the shadowed regions tend to essentially overestimate the measurements as the linearization of weathering elements becomes unpredictable. This yields higher values of ^3He, i.e. >8.67 ppb, thereby limiting the usage of the model in such constraints. From the statistical viewpoint, a comparative analysis is carried out between the predicted values and observed values of the ^3He abundance at the Apollo/Luna landing sites. The linear combination approach facilitates lower RMSE of 1.12 ppb as compared to the traditional method. Also, the MAE is found to be lower in the former with a high index of agreement. Referring to Table 3, the correlation is significantly improved when the averaging of site-dependent samples is implemented and hence, resolves the observed bias to some extent.

Table 3: Statistical measures of the solar wind ^3He concentration.

Methods	$\mathbf{R^2}$	**RMSE (in ppb)**	**MAE (in ppb)**	$\boldsymbol{d_i}$
Normal ^3He (61 Samples)	0.7625	1.1701	0.9443	0.9289
Normal ^3He (Average)	0.9295	0.7181	0.6522	0.9814
WA ^3He (61 Samples)	0.7835	1.1170	0.9092	0.9363
WA ^3He (Average)	0.9340	0.6947	0.6213	0.9826

Considering the reported ^3He abundances, the most promising sites are the pyroclastic deposits, regolith over the Agricola Mountains and unmantled floor of the Herodotus crater. In terms of economic feasibility and mining excavator capabilities, the fine-grained, volatile-rich pyroclasts emerge out to be suitable regolith for ISRU operations. The additional presence of hydroxyl ions encapsulated within the granular structure of the soil provides immediate attention for exploring the site.

5.1.4.1. Spatial Variations of Solar Wind Retained ^{3}He: Directional Variogram Analysis

The characterization of solar wind ^{3}He is indicative of the abundance within 1 μm weathered regolith. In order to quantitatively assess the retention budget, there is a requirement to incorporate the regolith depth for estimating the total ^{3}He inventory. From equation (4.11), the regolith thickness is computed using GLDEM100 and integrated with the weighted average ^{3}He profile. The unconsolidated nature of regolith gardens the retained ^{3}He significantly subject to micrometeorite impacts. Moreover, the exponential decay of ^{3}He-rich grains with respect to depth implicates orienting the mining excavator in a particular direction for subsequent extraction. Such modelling initiative also avoids the loss of ^{3}He ions while operating drilling rig straightaway.

In Figure 18(a), it is observed that the abundance of ^{3}He in the non-pyroclastic regoliths exhibits contradictory behaviour. The reported concentration from a weighted average approach provides higher estimates ranging from 6.59 ppb. This is also in concordance with the measurements carried out through the traditional algorithm. However, the relative spatial distribution after accommodating the regolith thickness profile suggests that there is an overall decrease of about 25% compared to the rest of the region, excluding the ejecta cover. Moreover, the increased ^{3}He content per unit area in a few localized vicinities indicates the diverse nature of the geochemical constraints present in the soil. It is argued that the effect of local weathering trends dominates the retention scenario of ^{3}He, wherein high band depth ratios and continuum slopes contribute the most. In this context, the ilmenite content significantly outweighs other proxies in determining the areal repository.

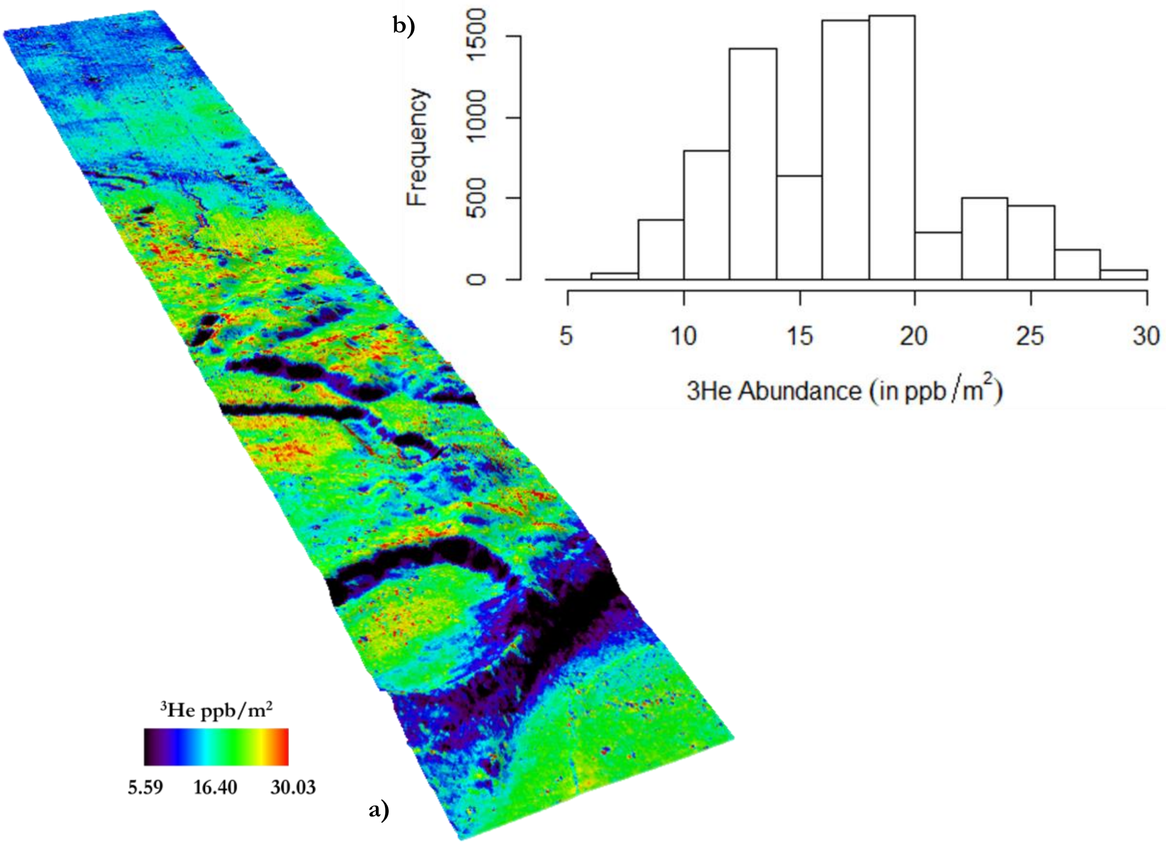

Figure 18: a) Spatial distribution of ^{3}He abundance per unit area for Vallis Schroteri region. b) Histogram plot of the corresponding areal concentrations. The bins are considered default.

From Figure 13(a) the basaltic regoliths containing non-pyroclasts attribute to lower amounts of Ti content, which is possibly associated with partial melting of cumulate piles from a hypothesized lunar magma ocean. The distinctness in the abundance is apparent for some concentrated sub-regions, whereby there is an equal contribution of CS and IBDR. Furthermore, the average regolith thickness of the region is comparatively less than the other part, suggestive of lower ^{3}He retention with Ti deficient soils. Referring to Figure 18(a), the green colour patches in the top portion of the image are the result of ilmenite dichotomy, wherein the effects of weathering processes are mostly found to be reduced. The quantitative abundance of the sub-region located parallel to the linear rille extent resembles the calculated proportions from the traditional algorithm (encircled with a solid black line in Figure 16(a)). Since it is known that the vertical distribution of ^{3}He tends to reduce at greater depths, the thicker regolith of Agricola Mountains doesn't seem to influence the abundance much. Thus, the mining strategies could be planned for extracting potential ^{3}He volatile from regoliths with higher ilmenite percentage and optimal thickness with respect to the bedrock. Additionally, the contribution of reddening and attenuated mafic band depth on the retention is significant in delineating the ^{3}He-rich soils. The directional component is also equally vital for determining the spatial variability of the abundance, thereby assisting in the mining excavation practices.

The frequency distribution of the areal concentration is depicted in Figure 18(b), with a mean of 16.40 ppb/m^2. The computed skewness and kurtosis of the distribution are found to be 0.3454 and -0.3789 respectively. Essentially, there is an acceptable limit for both parameters to follow the normal distribution: -0.5 to 0.5 for skewness and -1.96 to 1.96 for kurtosis. The measured parameters are, thus, in close agreement with the bounds. In order to make data more interpretable, this is necessary for subsequent variogram analysis of the estimated ^{3}He content. The retentive variations in the solar wind volatile distribution across the regolith are strongly aligned with the variogram observations. Figure 19(a) exhibits the empirical variogram of 8000 randomly sampled points from low, medium and high ^{3}He abundant zones. As part of the quantitative assessment, the spatial discontinuity of the data is marked at the origin representing the short scale variance or nugget effect. This is mainly caused due to the combination of microscale geological variations and induced measurement errors. The former is usually characterized by a negligible associated correlation of the space weathering alterations that cannot be captured within the resolution cell of ~151.7 m. Moreover, it is also inferred about the variability trends per unit area of the retained ^{3}He with respect to depth. The changes in the abundance are not pronounced in the form of mixed pixels, however, instances of significant variations are noticed for two adjacent sampling cells. Also, the uncertainty in the ^{3}He measurement corresponding to an assigned spatial extent can induce higher nugget. The observed nugget effect in the variogram is found to be consistent in all the direction from Figure 19(b). Hence, it proves to be an essential aspect for modelling the minute geological variations through which the retention is highly controlled. The sill is not reached in the variogram trend, thereby making the distribution highly fractal and subject to longer correlation length. This depicts the increased variance, closely monitoring the autocorrelated ^{3}He samples. Considering the intermediate-scale variance, there is a slightly cyclic pattern in the semivariance estimates relative to lag distances. The astrogeological events associated with lunar surface tend to be repetitive in occurrence. One of the most prominent evidence induces the weathering of the lunar soil, wherein meteorites/micrometeorites, solar wind and galactic cosmic rays interact with the surface periodically over a defined geologic time. The maturity of the regolith further reconfirms the cyclicity in the variogram: positive correlation followed by dampened negative correlation. The black arrow is suggestive of the irregular temporal cycle of the geologic events, wherein the variations essentially govern the ^{3}He retention. During this period, the semivariance is found to be constant for a particular lag distance, indicating a lower correlation of the abundance. Perhaps this is attributed to the intrinsic microscale changes in conjunction with non-retentive characteristics of the soil. Historically, such specific variogram trend is often referred to as the hole effect.

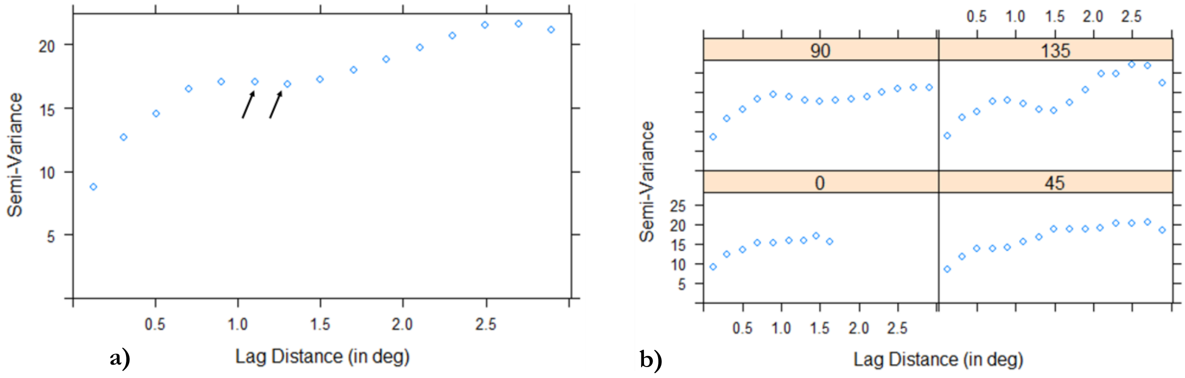

Figure 19: Spatial variability of the ^{3}He distribution. a) Empirical variogram representation of the Vallis Schroteri. b) Incorporation of directional component in the variogram analysis and interpretation. Cutoff is taken as 3.

The overall spatial variability of the abundance is however not seen in a specific direction. This is elaborated by considering the directional component. It can be found that the variance in horizontal direction follows an exponential trend, thereby exhibiting higher spatial autocorrelation within the lag distance of 0.5. Moreover, the pattern appears to replicate the deterministic implantation process with no correlation after 0.75. As the lunar regolith erodes in every 20 million years, the intensity and frequency of the cyclic pattern are not so strong. The smaller values of semivariance below theoretical sill impart higher correlation. It is also observed that there is a systematic increase in ^{3}He abundance from proximal to distal regions, oriented at 45°, of the Vallis Schroteri. This decreases the spatial correlation as the lag distance increases. The distribution in the vertical direction shows that the variogram reaches horizontal sill at ~1, with a slightly undulating shape. This provides evidence of small-scale periodic process influencing the retention scenario of ^{3}He. One such minor effect may be the sequential trap and release of weakly bound inter-grained ^{3}He due to its unstable behaviour towards temperature variations. Also, the sputtered ^{3}He ions from the less retentive soil tend to latch with the defects present in the crystallographic lattice. The vertical variogram captures the additional semivariance from the stratigraphic layering of the lunar surface. The small-scale petrological variations are often difficult to interpret compared to apparent large-scale stratigraphic differences. This gets prominent in the directional variogram trend, which is not likely to reach sill variance. Observing the spatial variations at 135°, there is a strong dominating geologic cyclicity associated with ^{3}He abundance. The periodic trend attributes to the harsh space environment governing the total retention based on local maturation and ilmenite variations. The regolith is believed to be containing broken fragments which garden the surficial ^{3}He-rich grains subject to micrometeorite impacts. During the time of its formation, the Moon has been associated with intense impact events, thereby leading to the evolved crater and basin structures. However, this rate has decreased to a significant level now. The sporadic gardening of the regolith with respect to depth, therefore, provides implications for the observed cyclic trend in the retained ^{3}He abundance.

In addition, the variogram images are generated in order to visualize the observed trend for different cutoff and width. The width is considered to be 1/15 of the cutoff and hence, computed accordingly. A general observation is that the spatial variation of estimated ^{3}He in ppb/m^2 decreases with the increase in the cutoff. The upper bound of the cutoff is 3 after which randomness is introduced in the ^{3}He distribution. From Figure 20 it is found that the retention of ^{3}He is least along the diagonal of the spatial extent, oriented at an angle of 45° with respect to the centre origin. As the cutoff is decreased from 3 to 0.5, the variogram illustrates an increase in the autocorrelation between the samples. This can be clearly distinguished from the surrounding in dark blue colour, which changes to yellow at 0.5 cutoff. Geologically, the spatial dependence of surface temperature on the unstable inter-grained ^{3}He deposits may lead to inappropriate semivariance trends of the stable ^{3}He.

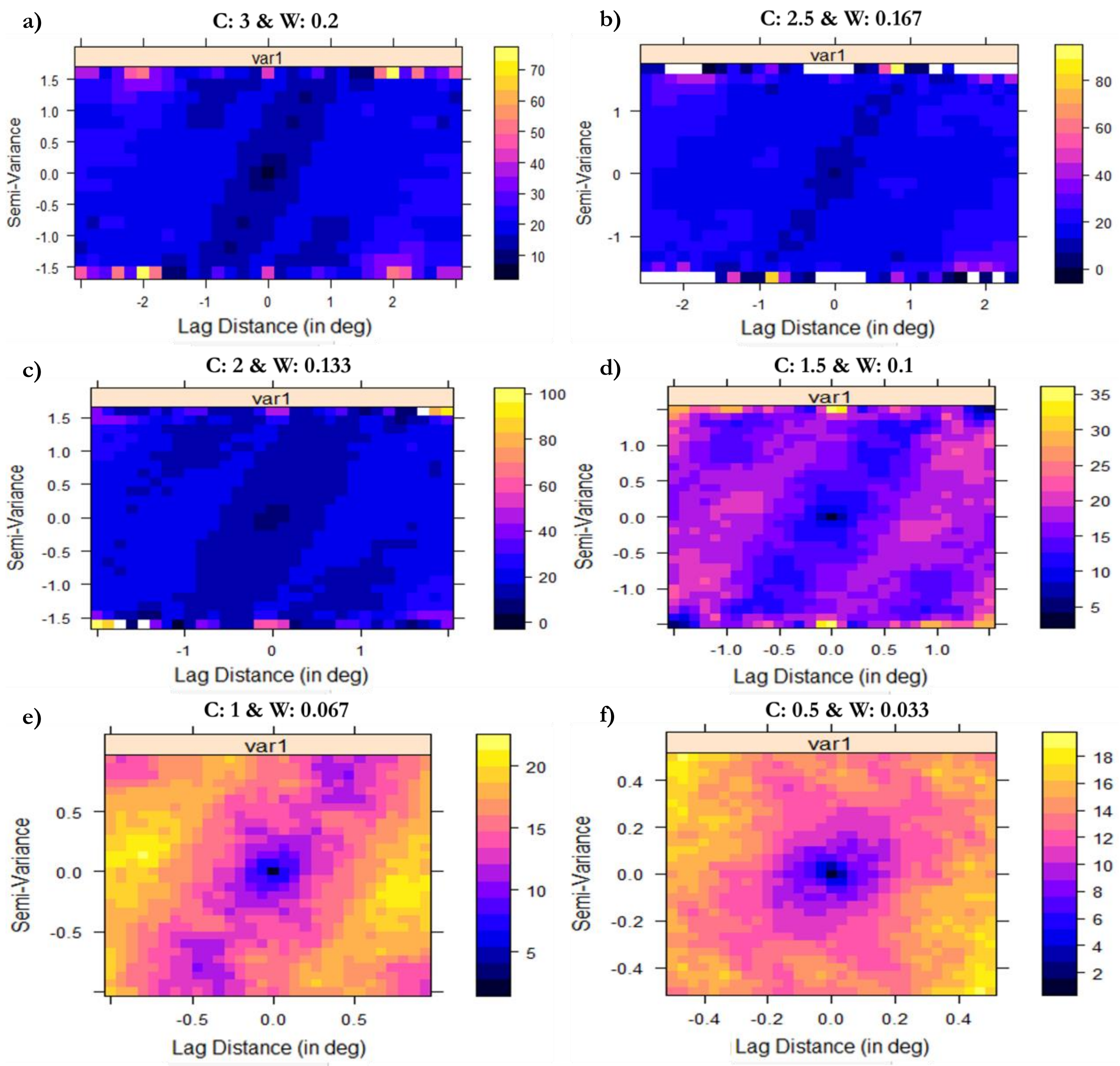

Figure 20: Effect of cutoff on spatial variability in terms of variogram image. C and W represent Cutoff and Width respectively. a) – f) depicting different variogram behaviours toward varying cutoff from 3 to 0.5.

The stable form of ^{3}He is strongly aligned with the space weathering variations and electroconductivity of the ilmenite mineral. However, there may be sputtering of unstable ^{3}He ions from the warmer regoliths. The estimated ^{3}He from the weighted average approach virtually eliminates the influence of loosely captured grained ^{3}He. Hence, the observed undulations in the variogram trend may provide insights into the thermal behaviour of the ^{3}He retention process. As seen in Figure 20(f), the reduced lag distance broadens the spatial correlation between the samples. Interestingly, the density of yellow colour is more in the diagonal oriented at around 135º, rather than the symmetrical representation. This gives a criterion for mining industries to plan the drilling operations accordingly. Moreover, the pink samples situated near highly correlated samples can be included for subsequent mining operations. In essence, the retained ^{3}He is more likely to be oriented towards 135º diagonal, considering the separation distance of less than 0.5. However, the less dense yellow colour is randomly distributed with observable patterns along 45º at 1 lag distance. This attributes to the different proportions of high ^{3}He abundance. The discrepancies in the random behavior are mainly caused due to the initial distribution of the data. Further investigations of petrophysical contents could provide new insights into the orientation of solar wind implanted ^{3}He.

5.2. Petrophysical Content Retrieval using Bistatic MiniRF Data Processing

In order to adequately understand the retentive properties of the regolith, the petrophysical content is an important parameter to retrieve. The scattering mechanisms are extracted for a strong polarimetric characterization of the soil. This is performed by utilizing the S-band data from MiniRF instrument onboard LRO under bistatic configuration with Arecibo Observatory, Puerto Rico. Moreover, the neural network based approach is implemented on the simulated data from standard physics-based backscattering model for retrieving the electrical properties of the lunar soil. The validation is carried out through statistical indicators for the available data of the Apollo landing site.

5.2.1. Extraction of Physical Scattering Mechanism

The associated physical processes of the regolith proximal to the Vallis Schroteri are modelled for retrieving the backscattering powers. After applying m-Chi decomposition to the CTLR data, the odd bounce scattering mechanism from moderately rough regoliths is characterized by blue colour in Figure 21(a). It is found that the typical regolith material predominately behaves as Bragg surface to the incident radar wave. The presence of larger aggregates in the soil eventually introduces even bounce scattering response to a pre-existing Bragg surface. Moreover, steep slopes over Agricola Mountains signify the double bounce geometry concerning a relatively smoother regolith. In such cases, the intensity of the backscatter signature depends on the composition and exposure age of the regolith. However, there are several occasions of mixed scattering behaviour, like the ejecta cover, a terraced wall of the Vallis Schroteri, and freshly formed microcraters. The yellow colour of the ejecta blanket is characterized with volume and double bounce scattering, possibly attributing to the randomly distributed anisotropic particles.

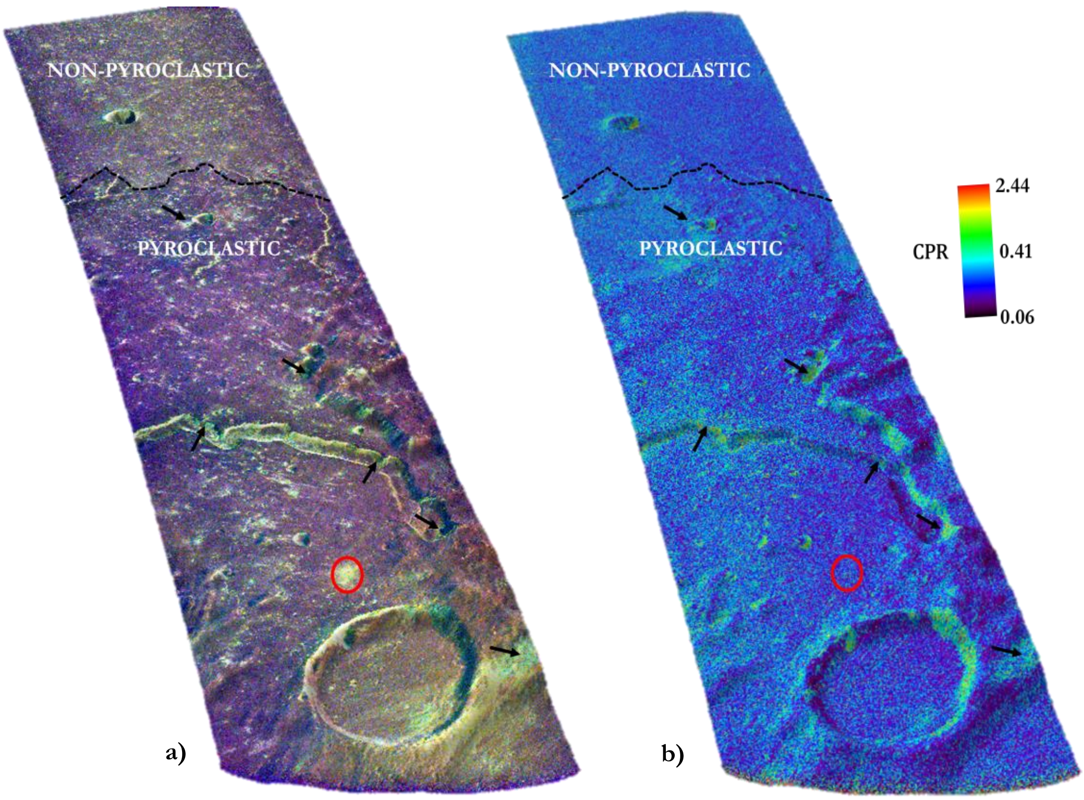

Figure 21: a) m-Chi decomposition image of the Vallis Schroteri region. R: Double Bounce Scattering, G: Volume Scattering and B: Surface Scattering. b) CPR image representing the surface roughness condition. The red circle represents a freshly formed microcrater in the vicinity of the primary rille. Black arrows depict the regolith with high volume scattering power. Dotted black line denotes the boundary between pyroclastic and mare deposits.

There are specific regions with enhanced volumetric scattering powers, represented in green colour. The black arrows further illustrate this effect. As observed in most of the cases, the increased scattering arises due to the presence of shadow. However, the dominance of green colour over yellow colour in the ejecta blanket shows strong evidence of volatile enrichment. A similar response is retrieved from the spectral signatures of the sites, wherein the absorption features are present near 2800 nm wavelength. The anomalously higher CPR values also confirm this behaviour, as shown in Figure 21(b). Moreover, the ejecta feature highlights the burial of impact melt glasses which comes in the category of cm- to m-scatterer. This indicates that there may be some fresh deposits located at ~1 m depth within the penetration capabilities of the incident radar wave. So, these inclusions may contribute to the additional subsurface scattering mechanisms, thereby explaining the significance of mixed ejecta behaviour.

On the other hand, the pyroclastic deposits offer an exploratory perspective of distinct radar response compared to the basaltic mare regolith. Evidently, there is a clear boundary between both regions, denoted by the black dotted line in Figure 21(a). The fine-grained structure of the pyroclasts (40 μm to 1 mm) provides a dominant odd bounce scattering response. Since the radar wave is sensitive to the cm- to m-scatterers, the relatively larger proportion of small-sized pyroclastic materials make the regolith appear darker in the image. This also results in smoother appearance than the surrounding gardened regolith, thereby retrieving the Bragg scattering mechanism. However, in the CPR image, this distinction is not clearly visible. Also, the enhancements in the volume scattering powers are significantly captured by the steep structures that are not in the direction of illumination. This is indicated by an abrupt surge in the CPR pixel values over 2. The pyroclastic regoliths are characterized with a mean CPR of 0.31, wherein cyan to green colour essentially represents a higher abundance of microcraters. One of the interesting aspects involves the association of lower CPR value with mixed dihedral and volumetric scattering response (denoted by a red circle). From the scattering patterns, it is quite apparent that the feature is highly sensitive to the incident radar wave owing to its freshly excavated material from the impact. This is also suggestive of higher cm- to m- scale scatterers, which are believed to be gardened within the regolith. From Figure 15 the feature exhibits an equal contribution of attenuated band depth and deposition of Fe^{2+} content towards space weathering processes. The observation is also in line with a relatively higher ilmenite abundance. However, the CPR indicator shows a much lower estimate of about 0.21, possibly attributing to the small scale roughness. This plausible behaviour may also be due to the inclusion of randomly polarized component in the retrieved scattering properties. Hence, there is a need to explore the petrophysical indicators to understand the regolith dynamics along with electromagnetic characteristics.

5.2.2. Dielectric Characterization of the Vallis Schroteri

The electrical properties of the lunar soil can be employed to describe the attenuation of the incident radar wave in terms of the dielectric permittivity. This further illustrates the understanding of the physical distribution of regolith grains aligned with dominant scattering processes. Moreover, the estimated dielectric behaviour characterizes the lithological structures associated with the water/ice signature. The dependence of radar backscatter with dielectric content, surface roughness, incidence angle and frequency is simulated, followed by performing dielectric inversion through MLP NN Regressor.

5.2.2.1. Sensitivity Analysis of the Radar Cross Section: IEM Model

The simulation of radar backscatter is carried out by adopting the IEM model, described in subsection 0. The contribution of the topmost regolith to the scattering mechanisms is considered in the model. The dielectric information of the regolith is mainly captured in the odd bounce scattering response as compared to the other mechanisms. Hence, the multiple scattering events arising from rocks, walls, and steep slopes are not taken into account. Figure 22 depicts the sensitivity of the radar backscattering coefficient in HH and VV polarimetric configuration with respect to varying incidence angles.

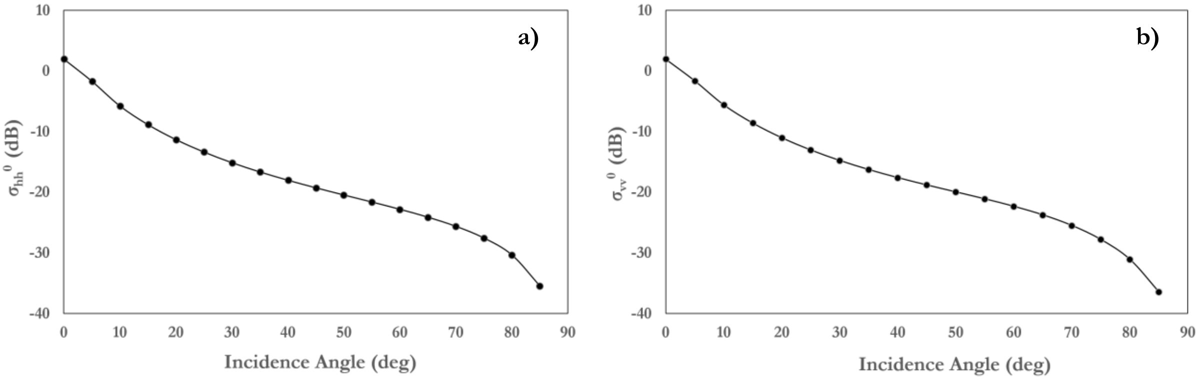

Figure 22: Simulated radar backscatter return as a function of incidence angle for a) HH-pol, and b) VV-pol.

The particular cases of HH-pol and VV-pol are indicated by Figure 22(a) and Figure 22(b) respectively at S-band frequency. The plot shows a decreasing trend of the polarized radar echo with the increase in incidence angle. This is also denoted by enhanced scattering powers from the top regolith for $\theta < 25^{o}$. However, the regolith with rock inclusions predominates the scattering behaviour for larger incidence angles. Also, the attenuation of the radar echo becomes increasingly significant in the subsurface due to the larger radar signal path length at a higher incidence. Hence, it is expected that the dominant scattering mechanisms in the S-band frequency are essentially coming from the surface and desiccated rocks mixed with the regolith. This can also be confirmed from Figure 21(a), which indicates the dominance of blue colour (Bragg scattering) over yellowish green colour (mixed scattering response) in the regolith. Specifically, the behaviour is observed in the pyroclastic and mare deposits. The lack of cm- to m-scatterers in the pyroclastic regolith contributes to the dominant surface scattering, whilst the large-sized buried rocks in the non-pyroclastic region provide the hazy appearance with included volume scattering component.

In Figure 23 and Figure 24, the sensitivity of the radar backscatter is observed with respect to changing dielectric constants and RMS heights. The real part of the complex dielectric constant ranges from 1.5 to 12. The imaginary part is fixed to the value of 0.003, attributing to its lower influence on the backscattering response. Equations (2.10f) and (2.10g) show that with increasing dielectric constant, the Fresnel reflection coefficients increase the surface scattering contribution. This trend is also visible in the sensitivity plots, depicted in Figure 23(b).

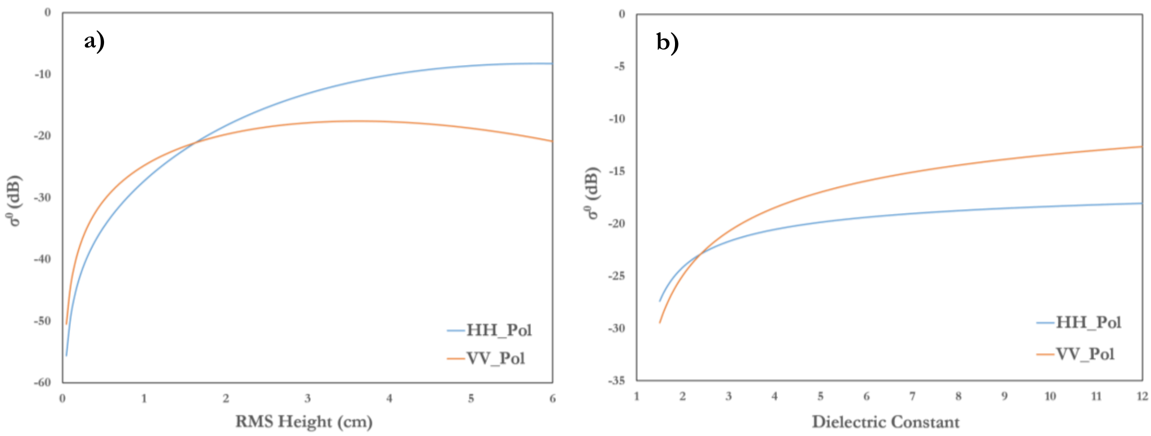

Figure 23: Simulated radar backscatter return as a function of a) surface roughness, and b) dielectric content. The incidence angle is considered 57.5º corresponding to bistatic MiniRF configuration.

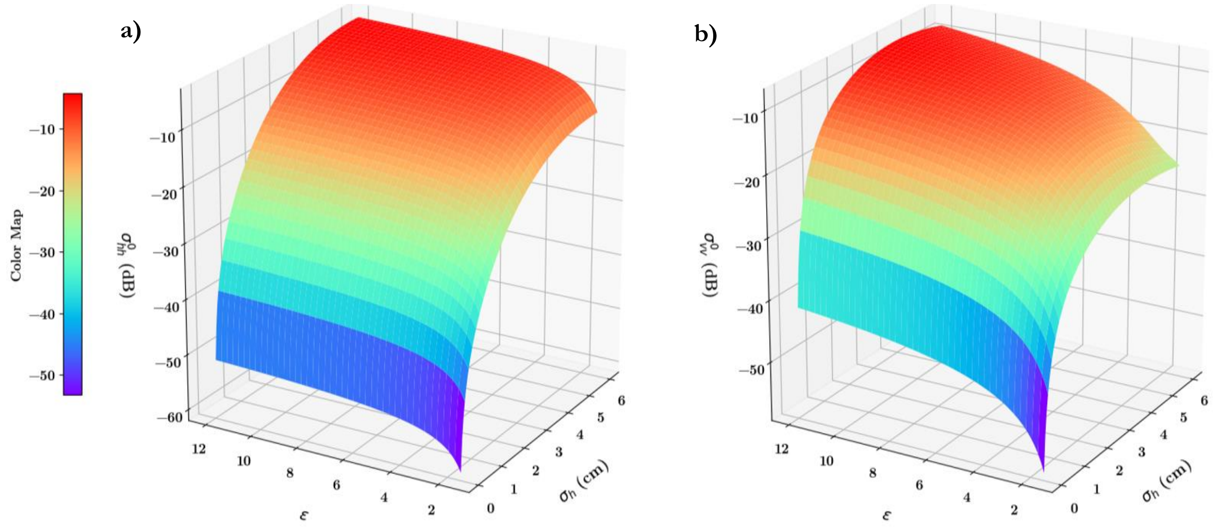

Figure 24: 3D Sensitivity plots representing the simulated radar backscatter as a function of surface roughness and dielectric properties for a) HH-pol, and b) VV-Pol. The incidence angle is 57.5° corresponding to bistatic MiniRF configuration.

One of the implications may be the increased penetration of the radar echo into the subsurface at lower dielectric constant reducing the backscattering contribution from the surface. This increases the dielectric contrast between the fine-grained regolith and buried rocks of cm- to m- scale. Similarly, the radar backscatter is also influenced by surface roughness that can be compared to the incident wavelength. Since the correlation length is assumed to be constant, the RMS height variations corresponding to the vertical profile of the roughness is considered for simulation. In Figure 23(a), it is observed that the backscattering coefficient increases with an increase in the RMS height. In principle, the radar energy tends to reflect from the smoother regoliths, which can be assumed as crater fills, and rock-poor dust mantling surface. This further implicates the lower amount of received energy, thereby darkening the structural appearance in the image. The pyroclastic regolith is in dark tonality as compared to the surrounding mare deposits in Figure 8(b), distinctly separated by a white dotted line. However, the structures exhibiting steep-sided walls and abrupt topographical terrains enhance the radar backscatter as the vertical component of the roughness is significantly increased. This case is more evident in the walls of Vallis Schroteri and Herodotus crater, which becomes a dihedral structure for the incident radar signal. Moreover, the plausible inclusion of impact melt deposits and broken rock fragments in the ejecta cover appears to have a relatively higher backscattering power.

From Figure 23(a) it can be inferred that the HH polarization enhances the radar wave intensity compared to the VV polarization with the increase in surface roughness. This attributes to the possible orientation of the regolith materials exhibiting higher Fresnel reflectivity in the HH polarization. The trend is found to be more evident beyond 1.65 cm RMS height, thereafter increasing significantly. Additionally, the visual comparison of the 3D sensitivity plots is carried out, which essentially represents the backscatter variability with RMS height and dielectric constant in Figure 24. The red colour intensity decreases downward in a uniform manner for the HH polarization compared to the radial trend as observed in the VV polarization. Furthermore, there is an average -3.25 dB difference between the sensitivity of horizontal backscatter and vertical backscatter to the dielectric constant. The plausible reason could be relating to the minor changes in penetration depths of different polarizations. The forward simulation modelling of radar backscatter with its dependency on surface components and configurational technicalities hence provides subsequent training data for the MLP neural network based dielectric inversion.

5.2.2.2. MLP Neural Network Regressor for Dielectric Content Retrieval

The necessary training data from the sensitivity simulation is fed into the neural network for extracting the dielectric properties of the study site under investigation. The inversion is performed by training 15600 patterns of which 20% of the data is allocated for testing. The K-fold shuffling is applied for training, wherein the data independency is inherently ensured (Pedregosa et al., 2011). In this, the training of the simulated data requires approximately 23.35 seconds of Central Processing Unit (CPU) time on a high-performance computing (HPC) having 3.4 GHz Xeon E7 with 40 cores. The achieved training R^2 value comes out to be 0.985 for around 175 iterations. Moreover, the L2 regularization term is set to 0.0001, which indicates that Ridge regression is performed between the training data and training label. The regression defines the associated penalty term as the square magnitude of the coefficient. This is usually added to the loss function in order to minimize the error. The robustness of the model is increased with the decrease in the loss function value, as depicted in Figure 25.

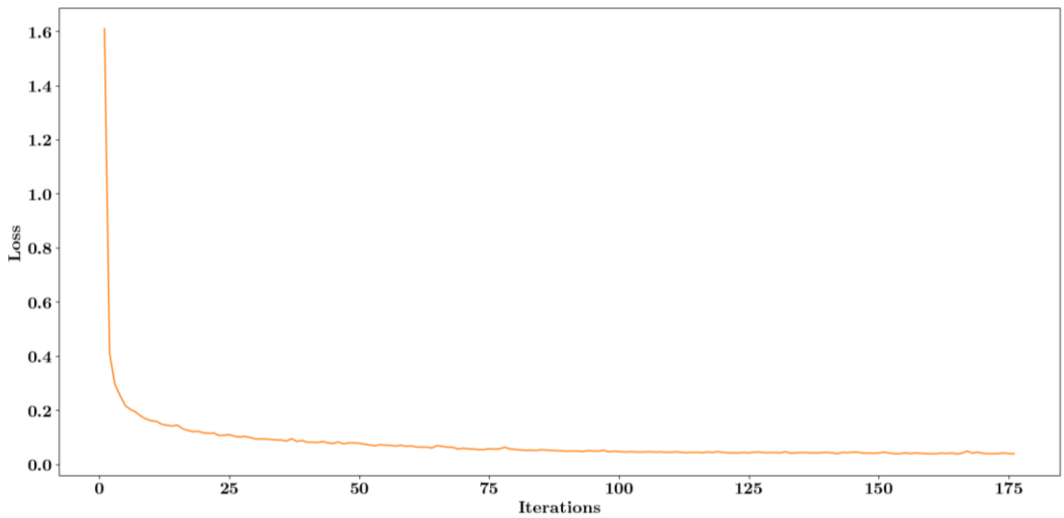

Figure 25: Changes in the loss with respect to the number of training iterations performed.

The trained network is then tested for 3120 radar backscatter patterns associated with two incidence angle of 35° and 49°. The choice of incidence angle values is made based on the identical incidence geometry of Chandrayaan-1 MiniSAR and LRO MiniRF radar instrument. The testing data yield an R^2 value of 0.987. Nearly equal training and testing R^2 signifies that the model is not overfitted. Furthermore, the evaluation is performed on the basis of statistical indicators by adopting the formulas described in equations (4.12)-(4.14). The accuracy of the retrieval is reflected in RMSE and MAE, which are found to be 0.26 and 0.13 respectively. Moreover, the degree of the model prediction error is estimated in terms of d_i. The value is 0.996, indicative of strong agreement with the observed dielectric constants. The applicability of the developed inversion model is also tested on the MiniRF CTLR radar data. Due to the lack of bistatic scenes for the Apollo landing sites, monostatic datasets are utilized and fed into the network. The in-situ measured dielectric constant values are then compared with the inverted results, as reported in Table 4.

Table 4: Comparison of the inverted and in-situ dielectric constant values of the Apollo landing sites. Note that only three sites are mentioned due to the limited availability of the MiniRF radar image.

Landing Site	Actual	Inverted
Apollo 11	11	11.18
Apollo 14	4.45	4.19
Apollo 16	5.64	5.69

The testing of the available monostatic scenes of the landing sites provides promising results as the inversion error appears low for all the reported sites. However, the reliability of the inversion is effectively governed by the sample space, which proves to be a limitation in this case. The future radar data acquisitions, specifically for the Apollo landing sites, could be employed for subsequent dielectric content retrieval using the developed model. This could hence validate the results further and comment upon the validity of the model for lunar regolith studies.

Looking upon the testing results, the topographically normalized horizontal and vertical components of the bistatic data is inputted to the network model along with the incidence angle of 57.5º. The testing of the Vallis Schroteri bistatic data and Apollo landing site monostatic data requires approximately 10 seconds for predicting the dielectric values on an HPC of similar configurations as that of the initial training. The final inverted image illustrates significant variations in the dielectric content of the Vallis Schroteri region, thereby showcasing the potential of MLP neural network in the complex retrieval problems. In Figure 26, the modal dielectric constant of the regolith is found to be 2.92 with a standard deviation of 0.17. One of the interesting results emerges out to be the dielectric behaviour of the pyroclastic units. The extensive mantling of the fine-grained glassy deposits exhibits a higher value of dielectric permittivity due to the possible association with hydroxyl ions. As the hydration in the geomorphological features increases, the dielectric content is expected to rise. The region also attributes to the smaller variations in the surface roughness, thereby depicting the lower intensity of the backscattered signal. Moreover, the boundary between the mare deposits and pyroclastic units, denoted by the dotted black line, is somewhat discernible similar to the m-Chi decomposed image in Figure 21(a). The blue colour in the image characterizes the agglutinated regolith with lower dielectric constant, which is suggestive of exposed soil-rock interface to the incident radar echo. This may implicate to a higher rate of regolith mixing derived from the prolonged cratering process, thereby resulting in an increased vertical roughness. The penetration of the radar echo thus decreases with a higher proportion of rocks brought from deeper regoliths. Several microcraters present in the nearby vicinity of the Vallis Schroteri, marked by black arrows, display predominantly yellow to red colour. This behaviour is usually associated with the relatively younger regolith having equal contributions of reddening effect and attenuation of mafic absorptions, as depicted in Figure 15.

The immature regolith, in the red circle, shows promising exposures of high dielectric permittivity, consistent with scattering properties in Figure 21(a). The gradual decrement of the colour intensity from the centre to radially outwards depict a smaller spread of ejecta generated from the microimpact events. The dielectric surge is also found to be strongly aligned with the lower penetration of the incident radar wave. In such cases, the density of the broken rock fragments that are comparable to the wavelength increases significantly. This results in the mixed scattering behaviour from the rocks and boulders lying over the gardened regolith. Additionally, the floor of the Vallis Schroteri is characterized by high dielectric permittivity, possibly attributing to the volcanic nature of the deposits. It may be expected that the floor contains larger pyroclastic enrichment, as compared to the marked area (solid black line). This is due to the closer proximity of the regolith to the source volcanic vent, Cobra head. The remarkably higher backscatter arising from the steeply sloped bedrock material with minimal deposition of soil exhibits an increased dielectric contrast relative to the surrounding regolith. Despite the categorization of dielectric contrast, the values show a relatively low to moderate variations in the region on a global perspective. Furthermore, there is a strong link between the dielectric properties and geotechnical variations in order to essentially determine the potential retentive nature of the soil towards solar wind volatiles.

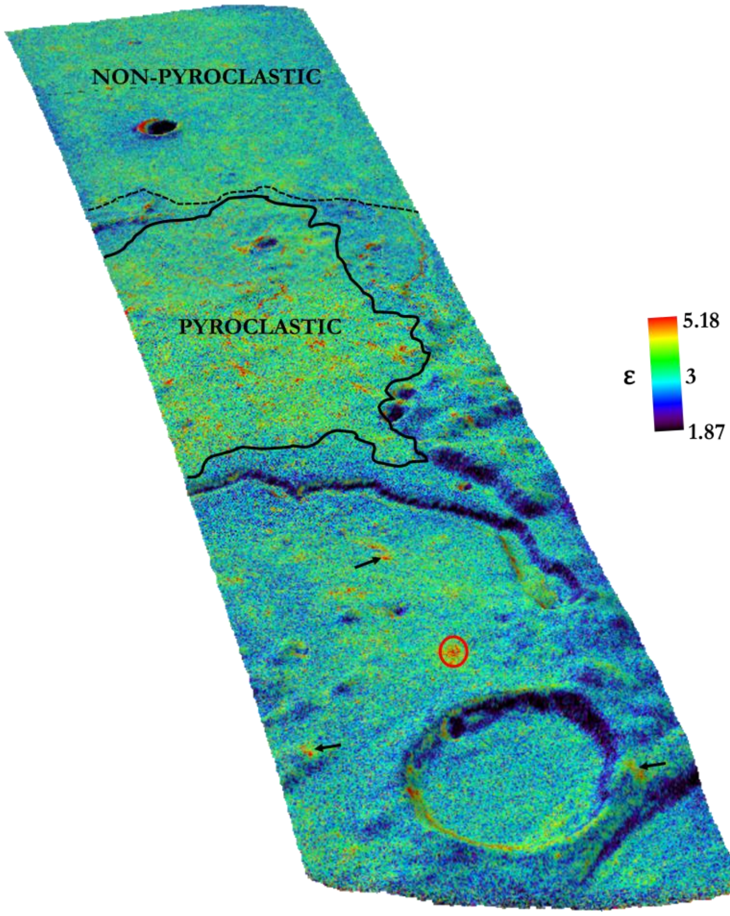

Figure 26: Retrieved dielectric constant of the study site from MLP NN-based inversion model. The observed standard deviation is 0.17.

5.2.3. Geotechnical Variants: Bulk Density, Relative Density, Porosity, and Void Ratio

The dielectric properties of the regolith are directly proportional to the bulk density, exhibiting a power relation from equation (2.13). It is observed that the regions dominated by Fe^{2+} content essentially represent relatively higher bulk density than the surrounding regolith, as shown in Figure 27(a). This is attributed to the nature of the space weathering process associated with the regolith. In some instances, the maturation of the soil wrongly captures the bulk density measurements. The region is expected to have larger number of microcraters, thereby signifying the increased agglutination of the regolith. The microimpact events eventually sputter materials from the nearby grain subject to comminution. This reduces the Fe^{2+} into metallic blebs of nanophase iron, thereby leading to an increase in the soil grain size. Moreover, the trend indicates the elevated value of porosity, which is a measure of void spaces in a particular grain. The results are consistent with the observation, and hence, suggestive of a dominant agglutination process associated with the regolith. The visual appearance of the variations in the bulk density is similar to the dielectric contrast. On average, the regolith is characterized by a modal bulk density of 1.06 g/cm^3. The associated standard deviation of the distribution comes out to be 0.13 g/cm^3. The retrieved bulk density measurements are in close agreement with the typical lunar values (Carrier III et al., 1973). Moreover, the increased bulk density trend denotes the compaction of the soil depending on the type of particle packing. The penetration of the radiation is also influenced by the bulk density of the regolith, depicting higher attenuation within the pyroclastic deposits.

The porosity of the regolith is estimated, using equation (2.15), for understanding the possible void spaces within the grain in an attempt to relate the volatile contamination. The larger soil grain tends to have more void spaces compared to the smaller grain. This is also attributed to the variations in the local maturation dominated by increased nanophase content. Figure 27(b) denotes the higher porosity of the nearby regions to the Vallis Schroteri, possibly indicating the association of agglutinated products of space weathering with pyroclasts. The average value is found to be 51% in the vicinity with a standard deviation of 0.02%. The higher order porosity values depicted by red colour essentially represents the shadowed regions or steep-sloped walls oriented in the non-illuminated radar zones. There is a relatively lower value for porosity in the central portion of the image, attributing to the fine-grained structure of the regolith with fewer void spaces. It can be noted that the estimated porosity includes both intragranular and intergranular aspects, which can potentially trap the incoming volatiles of exogenic origin. Moreover, this gives a hint towards possible hydroxyl inclusion within the grains. If the packing of the grains within a particular area is visualized, then the spaces between the grains are represented by a void ratio. As expected, the mantling of pyroclasts over regolith intensifies the packing to a relatively larger scale. This implies the gaps between the grains to be less, however, the intergranular and subgranular voids could indeed enhance the re-entrant surface.

From Figure 27(c) the void ratio is found to be high near the bottom portion of the image, mostly indicated by yellow colour. The emergence of significant geomorphological features, like Vallis Schroteri, Herodotus crater, and Agricola Mountains, displays the diversity of the local regolith. This also influences the distribution of the packing to a more loose structure, thereby creating larger number of voids. The average relative density is reported by considering the areal extent of the region as ~21%, which falls in the category of loose soil from Table 1. This is depicted by blue shades near the primary rille in Figure 27(d). Moreover, the structuring of the regolith facilitates the radar wave to penetrate and interact multiple times with the loosely packed grains due to the presence of voids. This is further indicated by high CPR value and dielectric constant for certain prone zones. On the contrary, the pyroclastic deposits in the middle portion of the image are relatively smoother associated with regional irregularities. The difference, however, is not significant but indicates a transition between loosely packed grains to moderately packed grains. In the void ratio image, a general trend is observed in the regoliths proximal to the dominant features exhibiting a gradual tonal shift from blue to green. This effect appears to descend in case of less significant features like microcraters and smaller rille. The blue and green colours are the representation of low void ratio and high void ratio respectively. In addition, while linking all the images in Figure 27, it is noteworthy that the conventions indicate the dissociation of regolith materials during the geological formation of the features either through impacts or emplacements. The intensity of the soil variations also depends on the size of the feature. For instance, in the pyroclastic regolith, there is a more dominant blue colour in the void ratio image with tints of green colour that fades with the distance from a particular microcrater.

The geotechnical characterization hence provides important clues regarding the nature of the regolith that could be subsequently tested for retentivity. The observations are strongly coupled with the corresponding scattering and dielectric properties in order to understand the implications of the associated physical processes. Moreover, the retrieved contents of the geotechnical characteristics essentially reflect the possibility of ^{3}He implantation subject to multisensor comparison.

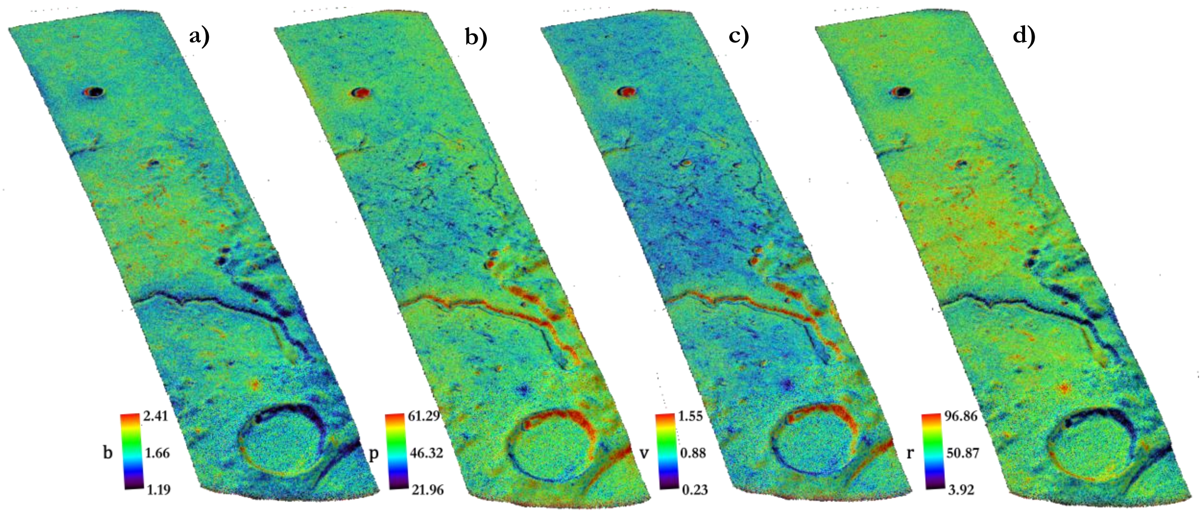

Figure 27: Geotechnical Characteristics of the Vallis Schroteri region. a) Bulk density, b in g/cm^3, b) Porosity, p in %, c) Void ratio, v, and d) Relative density, r in %.

5.3. Multisensor Data Analysis

The retained ^{3}He is compared with the petrophysical properties of the regolith in order to establish a possible hypothesis of the implantation mechanism. Due to the association of hydroxyl ions in the ejecta cover spectra, the lower ^{3}He abundance is considered vital for subsequent analysis. Meanwhile, the pyroclastic regoliths contain an increased concentration of ^{3}He per unit area, thereby serving as one of the prospective mining sites.

5.3.1. Influence of Petrophysical Properties on the Retained ^{3}He

The retrieved dielectric and geotechnical characteristics of the regolith varies with the retained ^{3}He content in the ejecta cover, as shown in Figure 28. It can be observed that the relatively younger regolith of the ejecta contains excavated feldspathic highland material associated with a lower dielectric constant and medium range of density. The higher values of relative density close to 0.8, as depicted in Figure 28(b), are intentionally taken from the elevated sloped terrain near the Herodotus crater for increasing the variability span. The retention of the ^{3}He tends to decrease for the regolith characterized by reduced dielectric constant values, as shown in Figure 28(a). Since the incoming solar wind essentially represents an ionizing radiation wave, the high dielectric contrast may lead to increased sputtering events. Apart from this, the penetration of the solar wind plasma in the loosely packed regolith may cause implantations at slightly greater depths than normal. The increasing retention trend could also be linked with the dielectric breakdown weathering of the soil. This is a type of weathering in which the charging of the topmost regolith occurs up to the point of the dielectric breakdown, mainly caused by solar energetic particles. In such events, substantial dissipation of charges takes place eventually as the materials placed at ~1 mm of the regolith gets vaporized and subsequently, electrically conductive. Although solar energetic particles are heavily dominated by high energy protons, there may also be some proportions of ^{3}He. The implantations thus may be aligned with the dielectric permittivity of the regolith. Despite the plausible inclusions of the immature impact melt deposits, the ejecta is observed to have lower dielectric constant values than the gardened regolith. This may have caused due to the intense dielectric breakdown. Apart from this, the increased roughness of the ejecta restricts the radar wave to penetrate, thereby attributing to the multiple scattering events. Figure 28(c) depicts that the retention is influenced dramatically by volume scattering as compared to the double bounce scattering mechanism. The associated correlation coefficient exhibits a sharp decline from 0.5 to 0.34. Since the increased volume scattering powers essentially originate from the buried anisotropic particles, this trend is of particular interest.

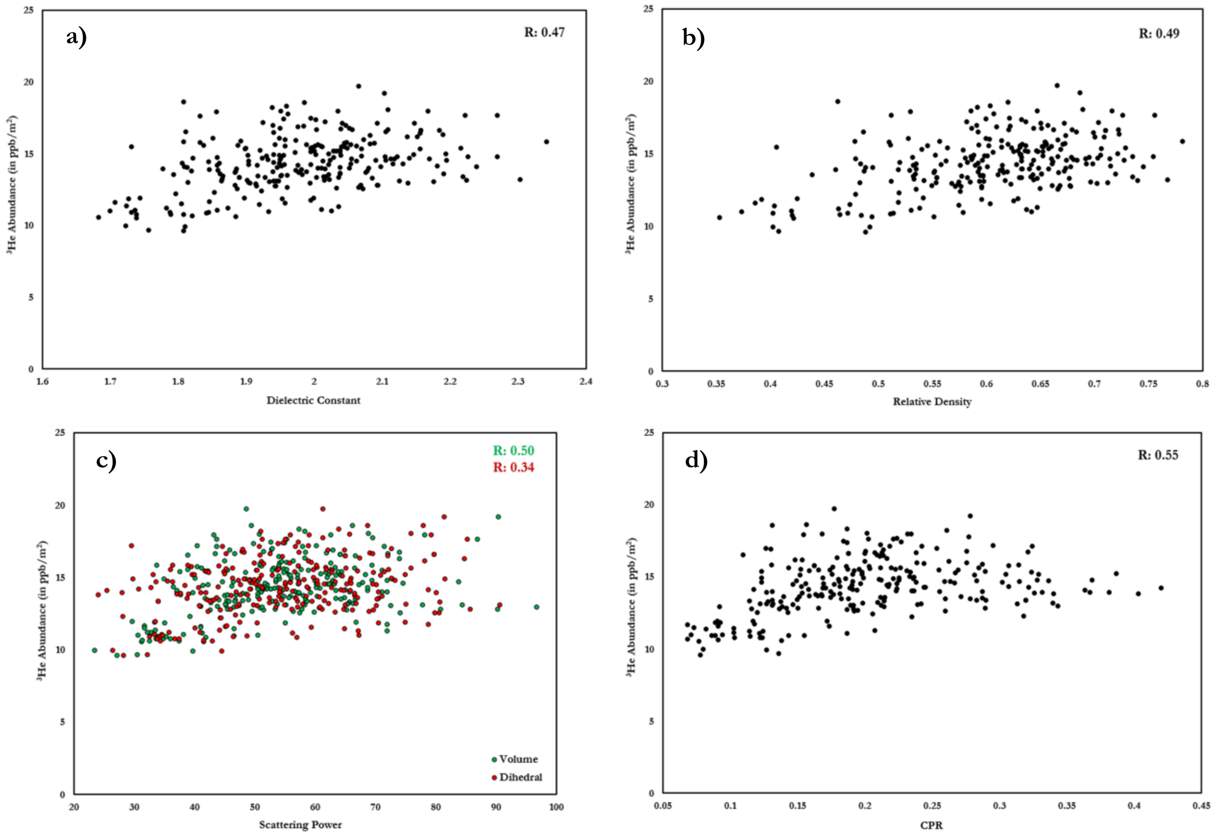

Figure 28: Multisensor comparison of ^3He content, for ejecta cover blanket, with a) Dielectric constant, b) Relative density, c) Scattering power, and d) CPR. Note that linear regression line is fitted for all the cases.

The ejecta materials are eventually marked with increased hydration from the spectroscopic analysis. Such an increase may be associated with volume scattering, wherein the specific hotspots of high dielectric contrast are formed. The behaviour is also supported by the ^3He abundance surge with the CPR. From Figure 28(d) the correlation coefficient is found to be 0.55. However, the CPR is low for the entire region, yielding an average pixel value of 0.27, which reflects that the variations are necessarily caused by the roughness alone. The retention of the ^3He thus is mainly related to the dipole-like grains buried within the gardened regolith. Moreover, in some of the instances, these grains contain exposures of hydroxyl ions, which proves significant for the mining operations. The distribution of the ^3He with dielectric constant and relative density provides an understanding for avoiding the loosely packed soils during the excavation process. The lower ^3He abundance of the region hence facilitates improved mapping related to the electrical and geotechnical properties of the weathered regolith. Furthermore, the effect of such relation is not inherently reflected in the abundance image due to the dominance of other governing factors like lower albedo and ilmenite content.

Also, the cross-variogram analysis is also performed for the lower abundant ejecta regolith and corresponding petrophysical indicators. As shown in Figure 33, it can be inferred that the semivariance values tend to decrease with distance for the correlation between retained ^3He and void ratio. It is noted that the void ratio values are log-transformed in order to fulfil the condition of normal distribution. The depicted relation is evident as the number of void spaces decreases with the increase in relative density. Also, the ejecta material is dominated by albedo, possibly representing the darkening of the soil. This yields a higher content of nanophase iron particles reduced from Fe^{2+}, which decreases the retention with time. As the void ratio increases, the possibility of ^3He to escape from the regolith significantly enhances due to the absence of the carrier upon which it is to be retained. Moreover, the porosity of the soil also increases accordingly, thereby exhibiting the similar variability trend. The gardening of the regolith is sufficiently high in the ejecta cover due to several microimpacts, clearly distinguishable from the mixed magenta colour contributing to the reddening effect in Figure 15. This attributes to the increase in the bulk density as there are a comparatively lower proportion of grains with a higher degree of crystallinity. The retention hence becomes positively dependent in correspondence to the bulk density measurements for the variations bounded by lower lag distances. However, there is a cyclic trend introduced in the semivariance of the samples after the lag distance of ~8000 m. This supports the incorporation of the reddening effect in addition to the albedo patterns across the ejecta cover over the geological timescale. Also, it could be inferred that the occurrence of the former effect is comparatively after the latter. The trend is not a strong representation, thereby attributing the dominance of the darkening effect possibly due to the young and immature regolith. In all the cross-variogram trends, the slightly cyclic pattern is induced at a higher lag distance, wherein the samples are not autocorrelated significantly. This may be the possible implication for the lower abundance of the ^{3}He with respect to the geotechnical properties of the ejecta regolith. Furthermore, the abundance is observed to be correlated with the surface scattering mechanism at lower lag distances. The variogram also exhibits a stepwise depreciation at higher lag distances. Figure 21(a) shows that the regolith of the ejecta is depicted in yellow colour with enhanced depolarization power and surface roughness. This is associated with double bounce and volume scattering with minimal contribution from the Bragg surface. Hence, the declining trend may be linked to the negative correlation of the ^{3}He concentration with surface scattering patterns.

Upon comparing the pyroclastic regoliths in Figure 34, the points marked by black arrows represent the potential outliers that are found to be prominent while decreasing the bin width. The general trend of the ^{3}He abundance and porosity exhibit an increasing spatial autocorrelation up to 1000 m followed by a declining cyclic pattern between the samples. The association of lower porosity with the fine-grained regolith weakly influences the abundance at shorter lag distances. However, as the lag distance increases, there is a negative correlation with the deposition of the ^{3}He into the grains, having enclosed and intragranular voids specifically. Moreover, the higher dielectric contrast of the soil is found to be correlated with the regional abundances. The regolith is mainly dominated by the mafic absorption band depths, which represents the relatively mature soil. This is also indicated by the fine-grained structure of the pyroclasts mantled over the regolith. Hence, the medium to high range of the dielectric permittivity is aligned well with the enhancements in the ^{3}He concentrations. In addition, the pyroclastic regoliths behave as a Bragg surface to the incident radar wave. This can be observed in Figure 21(a) with a dominant blue colour representing the surface scattering mechanism. According to the cross-variogram analysis, there is an existing spatial autocorrelation trend between the ^{3}He abundance and Bragg scattering power. The unboundedness of the spatial pattern emphasizes the relation between both variables. It can also be found that there is a slight dip in the trend before the increment. The reason may be the presence of microcraters responsible for increased roughness variations and lower surface scattering powers. Meanwhile, the associated ^{3}He abundances are observed to be relatively higher than normal, suggestive of negative correlation with the surface scattering element. On the contrary, the cross-variogram trend for the CPR is exactly opposite to the previous case, which is expected as the representation involves multiple scattering events, like dihedral and volume, arising from the immature microcraters.

5.3.2. Influence of Bistatic Angle on the ^{3}He content

The comparison of the retrieved ^{3}He abundance and bistatic angle for the low ^{3}He zone (ejecta cover) and high ^{3}He zone (pyroclasts) is shown in Figure 29. The samples of the ^{3}He abundance unaffected by the regolith thickness and affected by the exponential/uniform depth profile are taken into account for the subsequent analysis. In the pyroclastic regoliths, it is found that the concentration of the retained ^{3}He decreases with the increase in the bistatic angle. Interestingly, the amount of decrement depends on the distribution profile of the ^{3}He with respect to depth. Considering the surficial exposures, the correlation with the bistatic angle is observed to be less compared to the areal extent. The opposition is witnessed in the uniform ^{3}He profile with a higher correlation than the exponential profile. Moreover, the choice of the method also plays a vital role in defining the relation. For instance, the weighted average approach lessens the dependency of the bistatic angle on the ^{3}He estimates, particularly for the pyroclastic regoliths. However, the correlation tends to diminish for the ejecta regolith having lower concentration of ^{3}He. The response is more significant for the higher range of bistatic angles, i.e. greater than 5°.

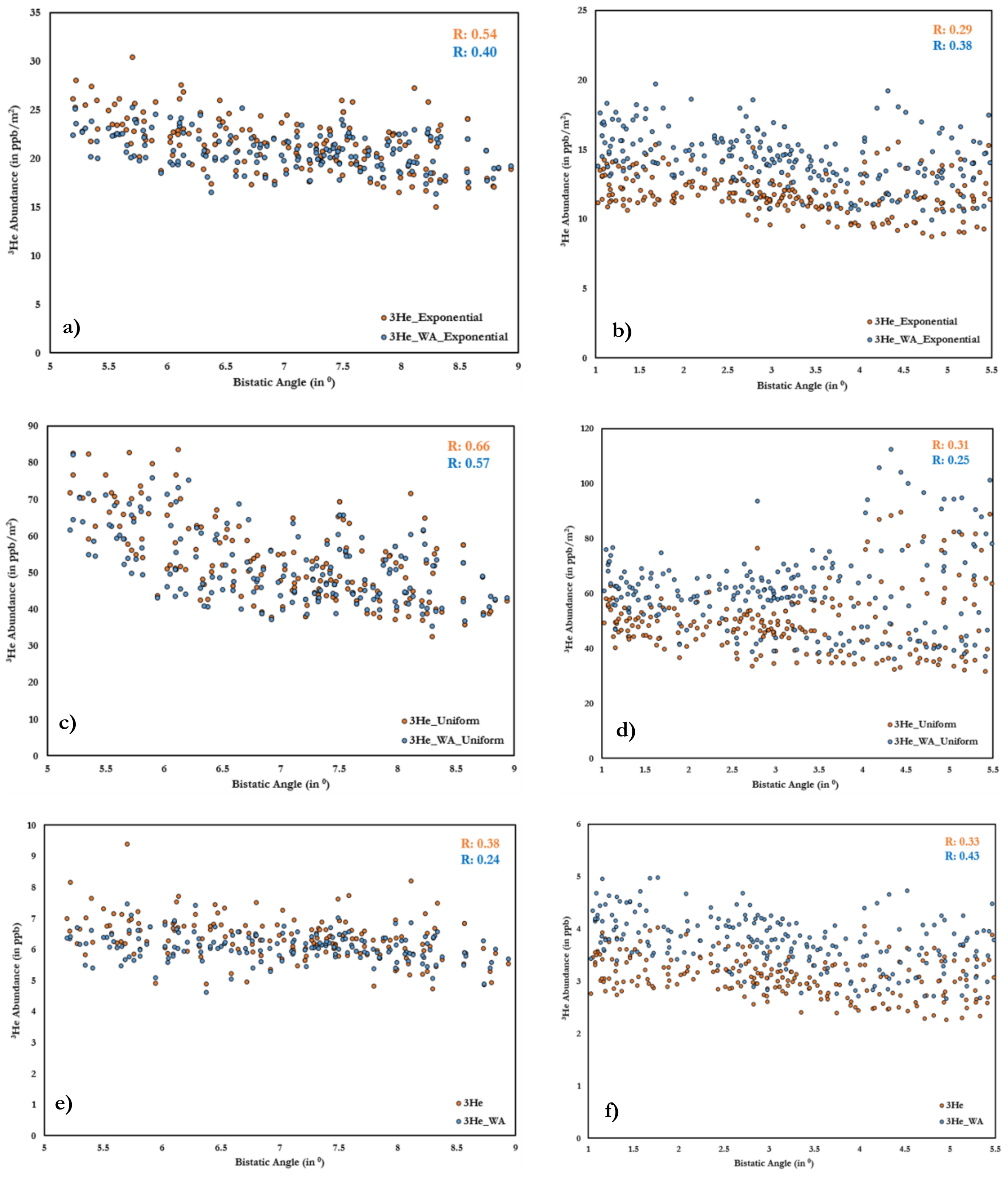

Figure 29: Effect of bistatic angle on retained ^{3}He content whilst considering uniform and exponential depth profile. a), c), and e) for Pyroclastic regolith. b), d), and f) for Ejecta cover blanket. Note that linear regression line is fitted for all the cases.

From the statistical viewpoint, the uncorrelated surficial ^3He exposures are found to be highly significant with an extremely low p-value. It is also shown that the correlation of the exponentially distributed ^3He with a bistatic angle (p value: 0.002) is more significant than the uniform case (p-value: 0.1) for the pyroclastic regolith. The choice of the ^3He depth profile is hence, reconfirmed for measuring the spatial variations across the regolith in section 5.1.4.1. In general, this peculiar behaviour of the regolith may be due to the possible opposition effect, stating the decreased ^3He abundance with an increase in the bistatic angle. Moreover, the emplacement of the pyroclasts over the already ^3He-rich regolith layer from the fire fountaining events may evolve the deeper regolith with volatiles. The subsequent gardening of such regoliths thus enhances the surficial concentration from the previously observed ^3He. This may lead to the miscalculations of the quantitative ^3He depth profile estimations. The Apollo and Luna samples, however, provide limited information on the distribution with respect to depth. Hence, the plausible explanation of the opposition response to the bistatic angle is left for further understanding.

5.4. Summary

The chapter highlights the data processing results, analysis and interpretation corresponding to the proposed research objectives and methodological framework. The retention hypothesis of the solar wind implanted ^3He is revisited by modelling space weathering trends of the lunar regolith along with topographically normalized solar wind fluence and ilmenite abundance. Moreover, the petrophysical indicators of the soil are essentially extracted by the bistatic MiniRF data, which includes dielectric and geotechnical characteristics. Furthermore, the multisensor data products are compared, wherein the influence of the petrophysical contents and bistatic angle on the retrieved ^3He abundance is studied. Finally, the relevant discussion is provided by considering the geological context for each of the results.

6. CONCLUSION AND RECOMMENDATIONS

The present research primarily focusses on the retention hypothesis of the solar wind implanted ^3He for the lunar regolith characterization using a multisensor approach. The spectroscopic measurements acquired from the Chandrayaan-1 M^3 data is employed for modelling the quantitative aspects of the retained ^3He into the regolith. The variations in the Earth's magnetospheric shielding of the Moon from the solar wind plasma are incorporated for normalizing the initial flux received by the surface. Moreover, the local incidence of the solar wind plasma particles is coupled for accommodating the selenographic variations in the flux. The retention of the received plasma flux for ^3He depends on the ilmenite abundance and space weathering trends of the regolith. Due to the absence of 415 nm spectral band in the M^3 data, the FeO-TiO_2 correlation diagram is utilized for characterizing the titanium content of the lunar soil (Shkuratov et al., 1999). In addition, three significant effects of the space weathering on the regolith are quantitatively represented by the spectral parameters, thereby capturing the subtle maturity variations in the regional soils.

One of the novel contributions of the research to the planetary community involves the conceptual association of the space weathering trends for subsequent prediction of the solar wind retained ^3He. This is established by building a hybrid spectral index, which is used in conjunction with the modelled solar wind fluence and in-situ ilmenite content. The index is mapped with the corresponding ^3He abundance for all the returned lunar samples to generate an empiric relation with an R^2 value of 0.7625. This approach essentially considers the independent nature of the parameters, however, the weathering processes are indeed interrelated to each other. Hence, the dependency among the altered weathering products is modelled to improve the retention mapping using a weighted average linear combination approach. The statistical parameters for indicating the reliability of the improved modelling shows an overall reduced error in terms of RMSE, MAE and d_i. On comparing with the OMAT based ^3He model, the error is significantly decreased from 3 ppb to 1.17 ppb.

The applicability of the developed models is further tested in the Vallis Schroteri region of the Aristarchus plateau, situated at the lunar nearside. The absolute mean difference of the ^3He abundance between both models is found to be 0.44 ppb. Based on the statistical error parameters, the weighted average approach is chosen for subsequent analyses. The most promising regions with higher abundance appear to be the pyroclastic regoliths and several hotspots in the nearby vicinity of the Vallis Schroteri. The floor of the Herodotus crater is characterized with medium to high ^3He concentrations, which is mantled by the low abundant ejecta cover. The reddening of the soil and attenuated mafic absorption band depths are found to be dominating weathering factors for delineating the high ^3He abundant zones. The reason may be associated with the increased nanophase iron particles reduced from Fe^{2+} content of the regolith. Moreover, the spatial variations of the ^3He distribution with depth are also assessed using directional variogram analysis for possible mining operations. In this context, the exponential depth profile is assumed and integrated over the regolith thickness to provide insights into the areal extent of the retained ^3He. The mean abundance per unit area of the study site is observed as 16.4 ppb/m^2. The characterization is greatly influenced by the electroconductive nature of the ilmenite mineral and hence, proves to be an important proxy. Additionally, the variogram of the ^3He exhibits a cyclic trend associated with the periodicity of an event over the geological timescale. The variations in the retained ^3He due to the weathering processes may serve as a potential periodic event. The intensity of the dips and colour density of the variogram image shows an increased orientation of highly abundant ^3He at around 135º.

In order to understand the physical processes associated with the retained ^3He, the radar backscatter information is employed using bistatic MiniRF CTLR data. The scattering mechanisms are extracted for the Vallis Schroteri region and analyzed for subsequent characterization of the regolith. The pyroclastic deposits show an increased response of surface scattering process, possibly due to the fine-grained structure and smooth appearance to the incident radar wave. Several microcraters near the primary rille exhibits the mixed response of double bounce and volume scattering, attributing to the higher proportions of cm- to m- scatterers in the freshly excavated regolith. The results are consistent for the CPR measurements, whereby the study site is characterized to have the mean pixel value of 0.41.

The dielectric properties of the regolith are modelled for exploring the regolith response to the ionizing radiation using coupled IEM and MLP NN Regressor. The radar cross section is simulated based on IEM, followed by performing a sensitivity analysis with the realistic values of incidence angle, dielectric constant and RMS height. The surface correlation function is assumed to be exponential depending on its better performance with the Earth-based radar observations. The known dielectric constant values from the Apollo landing sites are utilized for sensitivity analysis. The radar cross section is found to be directly proportional to the dielectric constant and surface roughness, while the response behaves inversely with the incidence angle. Hence, the observed relation is fed into the MLP NN Regressor as training data for the inversion modelling. The network is trained for two hidden layers with 32 nodes, and tanh activation function as the input data necessarily contains negative values. The reported training and testing R^2 values are 0.984 and 0.987, negating the overfitting problem of the data. Also, the testing of the network is performed for the Apollo landing sites, wherein the retrieved values are found to be in close agreement with the in-situ measurements. The higher dielectric contrast of the pyroclastic regoliths confirms the enhanced hydration observed in the spectral analysis. Overall, the mean dielectric constant of the study site is 3 associated with a standard deviation of 0.17. The immature microcraters proximal to the Vallis Schroteri depicts anomalously high dielectric contrast due to the increased number of excavated rocks and boulders mixed with the regolith.

The regolith dynamics of the Vallis Schroteri region are studied in conjunction with the geotechnical properties of the soil. Using the in-situ developed models, four parameters are retrieved: bulk density, relative density, porosity, and void ratio. The former two describes the compaction of the soil while the latter provides insights into the granular structure of the grain. The regolith comprises of loosely packed to medium packed grains with a mean relative density of 50.87%. Moreover, the void spaces present within the individual grains show an increased variation associated with the porosity. The bulk density of the pyroclastic regoliths is found to be relatively high, possibly due to the extensive mantling of the regolith during the fire fountaining event near the Cobra head. The combined dielectric and geotechnical characteristics are employed for subsequent understanding of the retention hypothesis of the solar wind ^3He through multisensor comparison.

The variability of the ^3He abundance per unit area is employed into comparing with petrophysical content of the regolith. The lower abundant regolith of the ejecta cover represents a relatively stronger correlation with volume scattering than dihedral scattering. This attributes to the presence of dipole-like features buried within the regolith. The results are also in concordance with the trace hydroxyl exposures of endogenic origin in the regolith. Moreover, the observed decreasing trend of the retained ^3He with the dielectric constant indicates that the loosely packed soils associated with higher relative density and void ratio necessarily contains lower ^3He abundance for ejecta cover regolith. The cross-variogram analyses further introduce cyclicity at a higher lag distance, indicative of reddening contribution to the highly dominated albedo within the gardened ejecta regolith. The fine-grained glassy pyroclastic materials in the regolith exhibit an increased spatial autocorrelation between the ^3He abundance and porosity of the soil at shorter lag distances. However, the trend becomes negatively correlated with an introduced cyclicity at more considerable lag distances, attributing to the weathering changes responsible for suppressing the ^{3}He contents. The increased surface scattering mechanisms from the smooth pyroclastic regoliths are found to have an affinity towards the ^{3}He retentions. On the contrary, the CPR is negatively correlated with the abundance as it primarily represents the depolarized scattering powers from the immature microcraters. Interestingly, the pyroclastic regoliths show an opposition effect of the ^{3}He to the bistatic angle, which suggests a decreased ^{3}He abundance with the increase in the bistatic angle. However, it is not observed significantly in the ejecta regolith. The plausible reason is yet to be explored. In this regard, the research proposes the pyroclastic regolith of the Aristarchus plateau be investigated for the subsequent mining operations due to the presence of both volatiles: hydroxyl and ^{3}He in huge amounts. The prospective landing site could be of significant importance in terms of the resources it can supply. Furthermore, the developed models and corresponding analyses in the research provide new insights into the possible retention hypothesis of the solar wind ^{3}He. The understanding could thus, enable the utilization of ISRU technologies for the establishment of the midlatitude lunar outposts near the Vallis Schroteri.

Recommendations

The applicability of the developed retention models could be tested for other lunar regions subject to the availability of the bistatic MiniRF datasets. Moreover, the upcoming higher spectral resolution data of the Imaging Infrared Spectrometer onboard ISRO Chandrayaan – 2 could be utilized to model the variations in the space weathering process. One of the aspects would be to integrate the contribution of the space weathering agents for prioritizing the retention framework based on probabilistic distribution. Moreover, the effect of energetic particles from the galactic cosmic rays on the quantitative estimation of the retained ^{3}He needs to be assessed. In the present research, the retention of the stable ^{3}He is considered, however, a future scope could involve the influence of unstable intergrained ^{3}He on the retained proportions. This can be evaluated by incorporating the regolith temperature in the retention model. Additionally, the observed hydroxyl exposures could be compared with the ^{3}He abundance in order to quantify the combined proportion per unit area of the regolith. Significantly, the temporal variations could be accounted for the retention modelling of the Apollo landing sites based on the Solar Wind Spectrometer measurements. Geostatistical techniques could then be applied for predicting the actual solar wind fluence of the Moon based on the spatial extent of the landing sites installed with corresponding spectrometers. Also, the implanted ^{3}He repository could be compared with the amount retained during the shielding of the Moon for accounting the variations in the measured quantity based on the spatiotemporal model. This could also be validated from the exospheric studies of the lunar surface, thereby contributing to the plasma environment near the soil. Although the axial tilt of the Moon is less significant in the solar wind fluence model, its consideration could develop a generic model for any of the airless bodies.

Coming to the petrophysical characterization, subsurface and multiple scattering mechanisms could be incorporated in the sensitivity analysis. The dielectric inversion modelling could then be refined based on the estimated radar cross-section. In the study, the influence of the bistatic angle on the observed scattering mechanisms and physical properties is not accounted for. Hence, this could be investigated for the subsequent coherent backscattering opposition effect. The inversion model seems more useful for the quad-pol data due to the utilization of the HH and VV polarizations. Moreover, the evaluation of the model for the multifrequency data could allow greater insights into the variations of the dielectric permittivity. The upcoming dual frequency SAR data onboard ISRO Chandrayaan-2 could be employed for evaluating the validity of the developed inversion model. In this regard, the study strongly recommends performing uncertainty simulations for the predicted ^{3}He values followed by directional and cross-variogram modelling.

LIST OF REFERENCES

Andrews, C. (1985). *The British Museum book of the Rosetta stone*. British Museum Press.

Arnold, J. R. (1975). Monte Carlo simulation of turnover processes in the lunar regolith. In *Lunar Science Conference* (pp. 2375–2395).

Atkinson, P. M., & Tatnall, A. R. L. (2010). Introduction Neural networks in remote sensing. *International Journal of Remote Sensing*, *18*(4), 699–709.

Baghdadi, N., Gaultier, S., & King, C. (2002). Retrieving surface roughness and soil moisture from synthetic aperture radar (SAR) data using neural networks. *Canadian Journal of Remote Sensing*, *28*(5), 701–711. https://doi.org/10.5589/m02-066

Beckmann, P., & Spizzichino, A. (1963). *The Scattering of Electromagnetic Waves from Rough Surfaces*. New York: Artech Print on Demand.

Bellucci, G., & Formisano, V. (1997). Imaging spectroscopy of the Moon: A study of the Aristarchus region. *Advances in Space Research*, *19*(10), 1535–1538. https://doi.org/10.1016/S0273-1177(97)00366-9

Bhatt, M. U. (2012). *Mineralogical analysis and iron abundance estimation of the Moon using the SIR-2 , HySI and M3 spectrometers on-board the lunar orbiter Chandrayaan-1*. Clausthal University of Technology.

Bhattacharya, A., Porwal, A., Dhingra, S., De, S., & Venkataraman, G. (2015). Remote estimation of dielectric permittivity of lunar surface regolith using compact polarimetric synthetic aperture radar data. *Advances in Space Research*, *56*(11), 2439–2448. https://doi.org/10.1016/j.asr.2015.10.007

Bishop, J. M. (2011). *Study of 12.5 cm RADAR as a means of mapping TiO2 in Lunar Basalts*. Honolulu.

Blewett, D. T., Lucey, P. G., Hawke, B. R., & Jolliff, B. L. (1997). Clementine images of the lunar sample-return stations: Refinement of FeO and TiO 2 mapping techniques. *Journal of Geophysical Research: Planets*, *102*(E7), 16319–16325. https://doi.org/10.1029/97JE01505

Bray, V. J., Atwood-Stone, C., & McEwen, A. M. (2012). Investigating the transition from central peak to peak-ring basins using central feature volume measurements from the Global Lunar DTM 100 m. *Geophysical Research Letters*, *39*(L21201), 1–5. https://doi.org/10.1029/2012GL053693

Cameron, E. N. (1987). Helium Site Mining on the and Moon : Selection. In *Lunar Helium-3 and Fusion Power (NASA Conference Publication 10018)* (pp. 35–63).

Cameron, W. S. (1964). An Interpretation of Schroter's Valley and Other Lunar Sinuous Rilles. *Journal of Geophysical Research*, *69*(12), 2423–2430.

Campbell, B. A., Carter, L. M., Hawke, B. R., Campbell, D. B., & Ghent, R. R. (2008). Volcanic and impact deposits of the Moon's Aristarchus Plateau: A new view from Earth-based radar images. *Geology*, *36*(2), 135–138. https://doi.org/10.1130/G24310A.1

Campbell, B. A., Hawke, B. R., & Thompson, T. W. (1997). Regolith Composition and Structure in the Lunar Maria: Results of Long-wavelength Radar Studies. *Journal of Geophysical Research E: Planets*, *102*(E8), 19307–19320. https://doi.org/10.1029/97JE00858

Campbell, B., Grant, J., & Maxwell, T. (2002). RADAR Penetration in Mars Analog Environments. In *Lunar and Planetary Science Conference* (Vol. 33, pp. 1–2).

Carrier III, W. D., Mitchell, J. K., & Mahmood, A. (1973). The relative density of lunar soil. In *Proceedings of the Lunar Science Conference* (Vol. 4, pp. 2403–2411).

Carrier III, W. D., Olhoeft, G. R., & Mendell, W. (1991). Physical Properties of the Lunar Surface. In *Lunar Sourcebook* (pp. 475–594). Cambridge University Press.

Charette, M. P., Adams, J. B., Soderblom, L. A., Gaffey, M. J., & McCord, T. B. (1976). Age-color relationship in the lunar highlands. In *Lunar Science Conference* (Vol. 7, pp. 132–134).

Charette, M. P., McCord, T. B., Pieters, C., & Adams, J. B. (1974). Application of Remote Spectral Reflectance Measurements to Lunar Geology Classification and Determination of Titanium Content of Lunar Soils. *Journal of Geophysical Research*, *79*(11), 1605–1613. https://doi.org/10.1029/JB079i011p01605

Chen, L. J. ., Bleacher, J. E., & Lowman, P. D. (2008). The Sinuosity of Lunar Rilles in the Aristarchus Plateau. In *Lunar and Planetary Science Conference* (Vol. 39). Houston.

Chevrel, S. D., Pinet, P. C., Daydou, Y., Le Mouélic, S., Langevin, Y., Costard, F., & Erard, S. (2009). The Aristarchus Plateau on the Moon: Mineralogical and structural study from integrated Clementine UV-Vis-NIR spectral data. *Icarus*, *199*(1), 9–24. https://doi.org/10.1016/j.icarus.2008.08.005

Chin, G., Brylow, S., Foote, M., Garvin, J., Kasper, J., Keller, J., … Zuber, M. (2007). Lunar reconnaissance orbiter overview: The instrument suite and mission. *Space Science Reviews*, *129*(4), 391–

419. https://doi.org/10.1007/s11214-007-9153-y
Chung, D. H., Simmons, G., & Westphal, W. B. (1970). Dielectric properties of Apollo 11 lunar samples and their comparison with earth materials. *Journal of Geophy*, *75*(32), 6524–6531. https://doi.org/10.1029/JB075i032p06524
Cladis, J. B.; Francis, W. E.; Vondrak, R. R. (1994). Transport toward earth of ions sputtered from the moon's surface by the solar wind. *Journal of Geophysical Research*, *99*, 53–64.
Clark, P., & McFadden, L. (2000). New results and implications for lunar crustal iron distribution using sensor data fusion techniques. *Journal of Geophysical Research*, *105*(E2), 4291–4316. https://doi.org/10.1029/1999JE001078
Clark, R. N., & Roush, T. L. (1984). Reflectance Spectroscopy: Quantitative Analysis Techniques for Remote Sensing Applications. *Journal of Geophysical Research*, *89*, 6329–6340.
Clark, R. N., Swayze, G. A., Livo, K. E., Kokaly, R. F., Sutley, S. J., Dalton, J. B., … Gent, C. A. (2003). Imaging spectroscopy : Earth and planetary remote sensing with the USGS Tetracorder and expert systems. *Journal of Geophysical Research*, *108*(E12), 5131. https://doi.org/10.1029/2002JE001847
Cloude, S. R. (2009). *Polarization: Application in Remote Sensing*. Oxford University Press.
Cloude, S. R., Goodenough, D. G., & Chen, H. (2012). Compact Decomposition Theory. *IEEE Geoscience and Remote Sensing Letters*, *9*(1), 28–32. https://doi.org/00300115 [pii]
Conrath, B., Gautier, D., Hanel, R., Lindal, G., & Marten, A. (1987). The Helium Abundance of Uranus From Voyager Measurements. *Journal of Geophysical Research*, *92*(A13), 15003–15010.
Conway, J. E. (1988). Lunar Helium-3 and Fusion Power. In *Proceedings of a workshop sponsored by the NASA office of Exploration and the Department of Energy Office of Fusion Energy* (pp. 1–233).
Davis, P. A. (1980). Iron and Titanium Distribution of the Moon from Orbital Gamma Ray Spectrometry with Implications for Crustal Evolutionary Models. *Journal of Geophysical Research: Solid Earth*, *85*(B6), 3209–3224. Retrieved from http://onlinelibrary.wiley.com/doi/10.1029/JB085iB06p03209/abstract
Dawson, M. S., Fung, A. K., & Manry, M. T. (1993). Surface parameter retrieval using fast learning neural networks Surface Parameter Retrieval Using Fast Learning Neural Networks. *Remote Sensing Reviews*, *7*(1), 1–18. https://doi.org/10.1080/02757259309532163
Dubois, P. C., Zyl, J. V., & Engman, T. (1995). Measuring Soil Moisture with Imaging Radars. *IEEE Transactions on Geoscience and Remote Sensing*, *33*(4), 915–926.
Dunkin, S. K., & Heather, D. J. (2000). Remote Sensing of the Moon: Past, Present and Future. In *Exploration and Utilisation of the Moon* (Vol. 4, pp. 5–10).
Eberhardt, P., Geiss, J., Graf, H., Grogler, N., Krahenbuhl, U., Schwaller, H., … Stettler, A. (1970). Trapped solar wind noble gases, exposure age and K/Ar-age in Apollo 11 lunar fine material. In *Apollo 11 Lunar Science Conference* (pp. 1037–1070).
Eliason, E. M., McEwen, A. S., Robinson, M. S., Lee, E. M., Becker, T., Gaddis, L., … Malaret, E. (1999). Digital Processing for a Global Multispectral Map of the Moon from the Clementine UVVIS Imaging Instrument. In *Lunar and Planetary Science Conference* (Vol. 30).
Elphic, R. C., Lawrence, D. J., Feldman, W. C., Barraclough, B. L., Maurice, S., Binder, A. B., & Lucey, P. G. (2000). Lunar rare earth element distribution and ramifications for FeO and TiO2: Lunar Prospector neutron spectrometer observations. *Journal of Geophysical Research*, *105*(E8), 20333–20345. https://doi.org/10.1029/1999JE001176
Fa, W., & Wieczorek, M. A. (2012). Regolith thickness over the lunar nearside: Results from Earth-based 70-cm Arecibo radar observations. *Icarus*, *218*(2), 771–787. https://doi.org/10.1016/j.icarus.2012.01.010
Fa, W., Wieczorek, M. A., & Heggy, E. (2011). Modeling polarimetric radar scattering from the lunar surface: Study on the effect of physical properties of the regolith layer. *Journal of Geophysical Research*, *116*(E3), E03005. https://doi.org/10.1029/2010JE003649
Fa, W. Z., & Jin, Y. Q. (2007). Quantitative estimation of helium-3 spatial distribution in the lunar regolith layer. *Icarus*, *190*(1), 15–23. https://doi.org/10.1016/j.icarus.2007.03.014
Fa, W. Z., & Jin, Y. Q. (2010). Global inventory of Helium-3 in lunar regoliths estimated by a multi-channel microwave radiometer on the Chang-E 1 lunar satellite. *Chinese Science Bulletin*, *55*(35), 4005–4009. https://doi.org/10.1007/s11434-010-4198-9
Farrell, W. M., Halekas, J. S., Killen, R. M., Delory, G. T., Gross, N., Bleacher, L. V., … Jackson, T. L. (2012). Solar-Storm/Lunar Atmosphere Model (SSLAM): An overview of the effort and description of the driving storm environment. *Journal of Geophysical Research E: Planets*, *117*(10), 1–11. https://doi.org/10.1029/2012JE004070
Farrell, W. M., Hurley, D. M., & Zimmerman, M. I. (2015). Solar wind implantation into lunar regolith:

Hydrogen retention in a surface with defects. *Icarus*, *255*, 116–126. https://doi.org/10.1016/j.icarus.2014.09.014
Fegley, B., & Swindle, T. D. (1993). *Lunar volatiles: implications for lunar resource utilization*. *Resources of Near-Earth Space*. Univ. of Arizona Press, Tucson.
Fung, A. K., Li, Z., & Chen, K. S. (1992). Backscattering from a Randomly Rough Dielectric Surface. *IEEE Transactions on Geoscience and Remote Sensing*, *30*(2), 356–369.
Futagami, T., Ozima, M., & Nakamura, Y. (1990). Helium ion implantation into minerals. *Earth and Planetary Science Letters*, *101*(1), 63–67. https://doi.org/10.1016/0012-821X(90)90124-G
Gaddis, L. R., Pieters, C. M., & Hawke, B. R. (1985). Remote Sensing of Lunar Pyroclastic Mantling Deposits. *Icarus*, *61*(3), 461–489. https://doi.org/10.1016/0019-1035(85)90136-8
Garner, R. (2017). Parker Solar Probe. Retrieved December 3, 2018, from https://www.nasa.gov/content/goddard/parker-solar-probe
Garry, W. B., & Bleacher, J. E. (2011). Emplacement Scenarios for Vallis Schroteri, Aristarchus Plateau, The Moon. In W. A. Ambrose & D. A. Williams (Eds.), *Recent Advances and Current Research Issues in Lunar Stratigraphy* (Vol. 477, pp. 77–95). https://doi.org/10.1130/9780813724775
Gillis, J. J., Jolliff, B. L., & Elphic, R. C. (2003). A revised algorithm for calculating TiO2 from Clementine UVVIS data: A synthesis of rock, soil, and remotely sensed TiO2 concentrations. *Journal of Geophysical Research*, *108*(E2), 5009. https://doi.org/10.1029/2001JE001515
Goetz, A. F. H., Vane, G., Solomon, J. E., & Rock, B. N. (1985). Imaging spectrometry for earth remote sensing. *Science*, *228*(4704), 1147–1153. https://doi.org/10.1126/science.228.4704.1147
Gold, T., Bilson, E., & Baron, R. L. (1976). Electrical properties of Apollo 17 rock and soil samples and a summary of the electrical properties of lunar material at 450 MHz frequency. In *Lunar Science Conference* (Vol. 7, pp. 2593–2603).
Greicius, T. (2015). Cassini at Saturn. Retrieved December 3, 2018, from https://www.nasa.gov/mission_pages/cassini/main/index.html
Hagfors, T. (1970). Remote probing of the moon by infrared and microwave emissions and by radar. *Radio Science*, *5*(2), 189–227.
Halekas, J. S., Bale, S. D., Mitchell, D. L., & Lin, R. P. (2005). Electrons and magnetic fields in the lunar plasma wake. *Journal of Geophysical Research: Space Physics*, *110*(A7). https://doi.org/10.1029/2004JA010991
Hawke, B. R., & Bell, J. F. (1981). Remote Sensing Studies of Lunar Dark-halo Implact Craters: Preliminary Results and Implications for Early Volcanism. In *Lunar Planetary Science Conference* (pp. 665–678).
Head, J. W., & Wilson, L. (1980). The formation of eroded depressions around the sources of lunar sinuous rilles: Observations. In *Lunar and Planetary Science Conference* (Vol. 11, pp. 426–428).
Heiken, G., & Vaniman, D. T. (1990). Characterization of Lunar Ilmenite Resources. In *Lunar and Planetary Science Conference* (Vol. 20, pp. 239–247).
Hiesinger, H., Wolf, U., Jaumann, R., & Neukum, G. (2003). Ages and stratigraphy of mare basalts in Oceanus Procellarum, Mare Nubium, Mare Cognitum, and Mare Insularum. *Journal of Geophysical Research*, *108*(E7), 5065. https://doi.org/10.1029/2002JE001985
Hood, L. L., & Williams, C. R. (1989). The Lunar Swirls: Distribution and Possible Origins. In *Lunar and Planetary Science Conference* (Vol. 19, pp. 99–113). Houston.
Horz, F., Grieve, R. A., Heiken, G., Spudis, P. D., & Binder, A. (1991). Lunar Surface Processes. In *Lunar Sourcebook* (pp. 61–120). https://doi.org/10.1017/CBO9781107415324.004
Housen, K. R., Wilkening, L. L., Chapman, C. R., & Greenberg, R. (1979). Asteroidal regoliths. *Icarus*, *39*(3), 317–351. https://doi.org/10.1016/0019-1035(79)90145-3
Isbell, C. E., Eliason, E. M., Adams, K. C., Becker, T. L., Bennett, A. L., Lee, E. M., … Weller, L. A. (1999). Clementine: A Multi-Spectral Digital Image Model Archive of the Moon. In *Lunar and Planetary Science Conference* (Vol. 30).
Johnson, J. R., Larson, S. M., & Singer, R. B. (1991). A Reevaluation of Spectral Ratios for Lunar Mare TiO2 Mapping. *Geophysical Research Letters*, *18*(11), 2153–2156.
Johnson, J. R., Swindle, T. D., & Lucey, P. G. (1999). Estimated Solar Wind Implanted Helium-3 Distribution on the Moon. *Geophysical Research Letters*, *26*(3), 385–388.
Johnson, R., Swindle, D., & Lucey, G. (1999). Estimated Solar Wind-Implanted Helium-3 Distribution On The Moon. *Geophysical Research Letters*, *26*(3), 385–388. https://doi.org/10.1029/1998GL900305
Jordan, J. L. (1990). Mapping Pyroclastic Deposits and Other Lunar Features for Solar Wind Implanted Helium. *Workshop on Lunar Volcanic Glasses: Scientific and Resource Potential*, (January), 43–45.

Keller, L. P., & Mckay, D. S. (1997). The nature and origin of rims on lunar soil grains. *Geochimica et Cosmochimica Acta*, *61*(I), 2311–2341. https://doi.org/10.1016/S0016-7037(97)00085-9

Kiko, J., Kirsten, T., & Ries, D. (1978). Distribution properties of implanted rare gases in individual olivine crystals from the lunar regolith. *Lunar and Planetary Science Conference Proceedings*, *9*, 1655–1665.

Kohonen, T. (1988). An introduction to neural computing. *Neural Networks*, *1*(1), 3–16. https://doi.org/10.1016/0893-6080(88)90020-2

Korotev, R. L., Jolliff, B. L., Zeigler, R. A., Gillis, J. J., & Haskin, L. A. (2003). Feldspathic Lunar Meteorites and their Implications for Compositional Remote Sensing of the Lunar Surface and the Composition of the Lunar Crust. *Geochimica et Cosmochimica Acta*, *67*(24), 4895–4923. https://doi.org/10.1016/j.gca.2003.08.001

Kulcinski, G. L., & Schmitt, H. H. (1988). The Moon: An Abundant Source of Clean and Safe Fusion Fuel for the 21st Century. In *Lunar Helium-3 and Fusion Power (NASA Conference Publication 10018)* (pp. 35–63).

Kumar, P. A., & Kumar, S. (2014). Estimation of optical maturity parameter for lunar soil characterization using Moon Mineralogy Mapper (M3). *Advances in Space Research*, *53*(12), 1694–1719. https://doi.org/10.1016/j.asr.2014.01.009

Le Mouélic, S., Lucey, P. G., Langevin, Y., & Hawke, B. R. (2002). Calculating iron contents of lunar highland materials surrounding Tycho crater from integrated Clementine UV-visible and near-infrared data. *Journal of Geophysical Research*, *107*(E10), 5074. https://doi.org/10.1029/2000JE001484

Lillesand, T. M., Kiefer, R. W., & Chipman, J. W. (2008). *Remote Sensing and Image Interpretation*. Hoboken, New Jersey: John Wiley & Sons, Inc.

Liu, N., Ye, H., & Jin, Y. Q. (2017). Dielectric Inversion of Lunar PSR Media with Topographic Mapping and Comment on " Quantification of Water Ice in the Hermite-A Crater of the Lunar North Pole." *IEEE Geoscience and Remote Sensing Letters*, *14*(9), 1444–1448.

Lucey, P. G., Blewett, D. T., & Jolliff, B. L. (2000). Lunar iron and titanium abundance algorithms based on final processing of Clementine ultraviolet-visible images. *Journal of Geophysical Research*, *105*(E8), 20297–20305. https://doi.org/10.1029/1999JE001117

Lucey, P. G., Blewett, D., Taylor, J., & Hawke, R. (2000). Imaging of lunar surface maturity. *Journal of Geophysical Research: Planets*, *105*(E8), 20377–20386. https://doi.org/10.1029/1999JE001110

Lucey, P. G., David, T., & Hawke, B. (1998). Mapping the FeO and TiO2 content of the lunar surface with multispectral imagery. *Journal of Geophysical Research*, *103*(E2), 3679–3699. https://doi.org/10.1029/97JE03019

Lucey, P. G., Hawke, B. R., Pieters, C. M., Head, J. W., & McCord, T. B. (1986). A Compositional Study of the Aristarchus Region of the Moon Using Near-Infrared Reflectance Spectroscopy. *Journal of Geophysical Research*, *91*(B4), D344–D354. https://doi.org/10.1029/JB091iB04p0D344

Lucey, P. G., Taylor, G. J., & Malaret, E. (1995). Abundance and Distribution of Iron on the Moon. *Science*, *268*, 1150–1153. https://doi.org/10.1126/science.268.5214.1150

Lucey, P., Korotev, R. L., Gillis, J. J., Taylor, L. A., Lawrence, D., Campbell, B. A., … Maurice, S. (2006). Understanding the Lunar Surface and Space-Moon Interactions. *Reviews in Mineralogy and Geochemistry*, *60*(1), 83–219. https://doi.org/10.2138/rmg.2006.60.2

Lue, C., Futaana, Y., Barabash, S., Wieser, M., Holmstrm, M., Bhardwaj, A., … Wurz, P. (2011). Strong influence of lunar crustal fields on the solar wind flow. *Geophysical Research Letters*, *38*(3), 4–8. https://doi.org/10.1029/2010GL046215

Lunar Exploration Science Working Group (LExSWG). (1992). *A Planetary Science Strategy for the Moon*.

McCall, G. H. J. (1970). Lunar Rilles and a Possible Terrestrial Analogue. *Nature*, (225), 714–716. https://doi.org/10.1038/228549a0

McEwen, A. S., Robinson, M. S., Eliason, E. M., Lucey, P. G., Duxburg, T. C., & Spudis, P. D. (1994). Clementine Observations of the Aristarchus Region of the Moon. *Science*, *266*, 1858–1862. https://doi.org/10.1126/science.1157880

Meek, T. T., Vaniman, D. T., Cocks, F. H., & Wright, R. A. (1985). Microwave Processing of Lunar Materials: Potential Applications. In *Lunar Bases and Space Activities of the 21st Century* (pp. 479–486).

Metzger, A. E., Johnson, T. V., & Matson, D. L. (1979). A comparison of mare surface titanium concentrations obtained by spectral reflectance and gamma-ray spectroscopy: An early assessment. In *Lunar and Planetary Science Conference* (Vol. 10, pp. 1719–1726).

Morris, R. V. (1976). Surface exposure indices of lunar soils: A comparative FMR study. In *Lunar Science Conference* (Vol. 7, pp. 315–335).

Morris, R. V. (1978). The Maturity of Lunar Soils: Concepts and More Values of Is/FeO. In *Lunar and*

Planetary Science Conference (Vol. 9, pp. 760–762).
NASA Manned Spacecraft Center. (1971). *Apollo 15: Preliminary Science Report.*
NASA STI/Recon Technical Report N. (1992). *Galileo Earth Moon Flyby*. Retrieved from http://adsabs.harvard.edu/abs/1992STIN...0000255
Nettles, J. W., Staid, M., Besse, S., Boardman, J., Clark, R. N., Dhingra, D., … Taylor, L. A. (2011). Optical maturity variation in lunar spectra as measured by Moon Mineralogy Mapper data. *Journal of Geophysical Research*, *116*(E00G17), 1–12. https://doi.org/10.1029/2010JE003748
Noble, S. K. (2004). *Turning rock into regolith: The physical and optical consequences of space weathering in the inner solar system*. Brown University.
Nozette, S., Lichtenberg, C. L., Spudis, P., Bonner, R., Ort, W., Malaret, E., … Shoemaker, E. M. (1996). The Clementine bistatic radar experiment. *Science*, *274*(5292), 1495–1498. https://doi.org/10.1126/science.274.5292.1495
Nozette, S., Spudis, P., Bussey, B., Jensen, R., Raney, K., Winters, H., … Robinson, M. (2010). The Lunar Reconnaissance Orbiter Miniature Radio Frequency (Mini-RF) Technology Demonstration. *Space Science Reviews*, *150*(1–4), 285–302. https://doi.org/10.1007/s11214-009-9607-5
Oberbeck, V. R., & Quaide, W. L. (1967). Estimated Thickness of a Fragmental Surface Layer of Oceanus Procellarum. *Journal of Geophysical Research*, *72*(18), 4697–4704.
Oh, Y., Sarabandi, K., & Ulaby, F. T. (1992). An Empirical Model and an Inversion Technique for Radar Scattering from Bare Soil Surfaces. *IEEE Transactions on Geoscience and Remote Sensing*, *30*(2), 370–381.
Oh, Y., Sarabandi, K., & Ulaby, F. T. (1994). An Inversion Algorithm For Retrieving Soil Moisture And Surface Roughness From Polarimetric Radar Observation. In *International Geoscience and Remote Sensing Symposium (IGARSS)* (pp. 1582–1584). Pasadena, CA, USA. https://doi.org/10.1109/IGARSS.1994.399504
Olhoeft, G. R., Frisillo, A. L., & Strangway, D. W. (1974). Electrical properties of lunar soil sample 15301,38. *Journal of Geophysical Research*, *79*(11), 1599–1604. https://doi.org/10.1029/JB079i011p01599
Olhoeft, G. R., & Strangway, D. W. (1975). Dielectric Properties of the first 100 meters of the Moon. *Earth and Planetary Science Letters*, *24*, 394–404.
Ozima, M., & Podosek, F. A. (1983). *Noble Gas Geochemistry* (First). Cambridge, UK: Cambridge University Press.
Parker, J. A., Kenyon, R. V., & Troxel, D. E. (1983). Comparison of Interpolating Methods for Image Resampling. *IEEE Transactions on Medical Imaging*, *MI-2*(1), 31–39. https://doi.org/10.1109/TMI.1983.4307610
Patterson, G. W., Stickle, A. M., Turner, F. S., Jensen, J. R., Bussey, D. B. J., Spudis, P., … Jakowatz, C. V. (2017). Bistatic radar observations of the Moon using Mini-RF on LRO and the Arecibo Observatory. *Icarus*, *283*, 2–19. https://doi.org/10.1016/j.icarus.2016.05.017
Pedregosa, F., Varoquaux, G., Gramfort, A., Michel, V., Thirion, B., Grisel, O., … Duchesnay, E. (2011). Scikit-learn: Machine Learning in Python. *Journal of Machine Learning Research*, *12*, 2825–2830. Retrieved from http://www.jmlr.org/papers/volume12/pedregosa11a/pedregosa11a.pdf
Pieters, C. M. (1978). Mare basalt types on the front side of the moon: A summary of spectral reflectance data. In *Lunar and Planetary Science Conference* (Vol. 9, pp. 2825–2849).
Pieters, C. M., Boardman, J., Buratti, B., Chatterjee, A., Clark, R., Glavich, T., … White, M. (2009). The Moon Mineralogy Mapper (M3) on Chandrayaan-1. *Current Science*, *96*(4), 500–505.
Pieters, C. M., & Noble, S. K. (2016). Space Weathering on Airless Bodies. *Journal of Geophysical Research: Planets*, *121*, 1865–1884. https://doi.org/10.1002/2016JE005128.Received
Poupeau, G., Michel-Levy, M. C., Mandeville, J. C., & Romary, P. (1978). Microcrater and solar-flare track maturation of the lunar regolith. *Geochmica et Cosmochimica Acta*, (January), 137–155. Retrieved from http://adsabs.harvard.edu/abs/1978mcvl.conf..137P
Quaide, W. L., & Oberbeck, V. R. (1968). Thickness determinations of the lunar surface layer from lunar impact craters. *Journal of Geophysical Research*, *73*(16), 5247–5270. https://doi.org/10.1029/JB073i016p05247
R Core Team. (2018). R: A language and environment for statistical computing. *R Foundation for Statistical Computing*. Vienna, Austria. Retrieved from https://www.r-project.org/
Raney, R. K. (2007). Hybrid-Polarity SAR Architecture. *IEEE Transactions on Geoscience and Remote Sensing*, *45*(11), 3397–3404.
Raney, R. K., Cahill, T. S., Patterson, G. W., & Bussey, D. J. (2012). The m-chi decomposition of hybrid dual-polarimetric radar data with application to lunar craters. *Journal of Geophysical Research*,

117(E00H21), 1–8. https://doi.org/10.1109/IGARSS.2012.6352465
Raney, R. K., Spudis, P. D., Bussey, B., Crusan, J., Jensen, J. R., Marinelli, W., … Winters, H. (2011). The Lunar Mini-RF Radars: Hybrid Polarimetric Architecture and Initial Results. *Proceedings of the IEEE*, *99*(5), 808–823. https://doi.org/10.1109/JPROC.2010.2084970
Rumelhart, D. E., Hinton, G. E., & Williams, R. J. (1986). Learning internal representations by error propagation. In D. E. Rumelhart & J. L. McClelland (Eds.), *Parallel distributed processing: explorations in the microstructures of cognition. Vol. 1* (pp. 318–362). Cambridge, Massachusetts: MIT Press.
Rynkiewicz, J. (2011). General bound of overfitting for MLP regression models. In *European Symposium on Artificial Neural Netrworks, Computational Intelligence and Machine Learning* (pp. 251–256). Bruges (Belgium).
Santarius, J. F. (2004). Lunar 3He and Fusion Power. *Fusion Technology*.
Santarius, J. F., Kulcinski, G. L., & Miley, G. H. (2006). A Strategy for D- 3He Fusion Development. *ANS Annual Meeting, Reno, NV*, (June), 4–8.
Schmugge, T. J. (1983). Remote Sensing of Soil Moisture: Recent Advances. *IEEE Transactions on Geoscience and Remote Sensing*, *GE-21*(3), 336–344.
Scholten, F., Oberst, J., Matz, K., Roatsch, T., Wählisch, M., Speyerer, E. J., & Robinson, M. S. (2012). GLD100 : The near-global lunar 100 m raster DTM from LROC WAC stereo image data. *Journal of Geophysical Research*, *117*(E00H17), 1–12. https://doi.org/10.1029/2011JE003926
Shkuratov, Y. G., Kaydash, V. G., & Opanasenko, N. V. (1999). Iron and Titanium Abundance and Maturity Degree Distribution on the Lunar Nearside. *Icarus*, *137*(2), 222–234. https://doi.org/10.1006/icar.1999.6046
Shukla, S., Kumar, S., & Agrawal, S. (2017). Mineral Mapping of FeO and TiO2 of the Cassini crater using Moon Mineralogy Mapper. In *Asian Conference on Remote Sensing* (Vol. 38, pp. 1–10).
Slyuta, E. N., Abdrakhimov, A. M., & Galimov, E. M. (2007). The Estimation of Helium-3 Probable Reserves in Lunar Regolith. In *Lunar and Planetary Science Conference* (pp. 3499–3504).
Soboleva, N. S., & Pariiskii, Y. N. (1964). The Possibility of Observing the Polarization of Thermal Radio Emission of Planets. *Soviet Astronomy-AJ*, *8*(2), 282–284.
Spudis, P. D., Bussey, D. B. J., Baloga, S. M., Butler, B. J., Carl, D., Carter, L. M., … Winters, H. L. (2010). Initial results for the north pole of the Moon from Mini-SAR, Chandrayaan-1 mission. *Geophysical Research Letters*, *37*(6), n/a-n/a. https://doi.org/10.1029/2009GL042259
Spudis, P. D., Bussey, D. B. J., Baloga, S. M., Cahill, J. T. S., Glaze, L. S., Patterson, G. W., … Ustinov, E. A. (2013). Evidence for water ice on the moon: Results for anomalous polar craters from the LRO Mini-RF imaging radar. *Journal of Geophysical Research E: Planets*, *118*(10), 2016–2029. https://doi.org/10.1002/jgre.20156
Staid, M. I., & Pieters, C. M. (2000). Integrated Spectral Analysis of Mare Soils and Craters: Applications to Eastern Nearside Basalts. *Icarus*, *145*(1), 122–139. https://doi.org/10.1006/icar.1999.6319
Staid, M. I., Pieters, C. M., Besse, S., Boardman, J., Dhingra, D., Green, R., … Taylor, L. A. (2011). The mineralogy of late stage lunar volcanism as observed by the Moon Mineralogy Mapper on Chandrayaan-1. *Journal of Geophysical Research*, *116*(4), 1–15. https://doi.org/10.1029/2010JE003735
Stern, S. A. (1999). The Lunar Atmosphere: History, Status, Current Problems, and Context. *Reviews of Geophysics*, *37*(4), 453–491.
Swindle, T. D. (1992). Abundance of 3He and Other Solar Wind Derived Volatiles in Lunar Soil. In *NASA Space Engineering Research Center for Utilization of Local Planetary Resources: Annual Progress Report 1992* (APR-92, p. III-19-III-26). Tucson, AZ 85712.
Swindle, T. D., Glass, C. E., & Poulton, M. M. (1990). *Mining Lunar Soils for 3He*. Tucson, AZ 85712.
Synder, J. P. (1987). *Map Projections: A Working Manual*. Washington.
Taylor, A., Keller, P., Morris, V., & Mckay, D. S. (2001). Lunar Mare Soils: Space weathering and the major effects of surface-correlated nanophase Fe. *Journal of Geophysical Research*, *106*, 27985–27999.
Taylor, L. A. (1994). Helium-3 on the Moon: Model Assumptions and Abundances. In *Engineering, Construction, and Operations in Space IV* (pp. 678–686).
Taylor, S. R. (1982). *Planetary Science: A Lunar Perspective. Lunar and Planetary Institute*. https://doi.org/10.1016/S0032-0633(96)00091-8
Tyler, G. L. (1968). Oblique-Scattering Radar Reflectivity of the Lunar Surface: Preliminary Results from Explorer 35. *Journal of Geophysical Research*, *73*(24), 7609–7620.
Ulaby, F. T., Moore, R. K., & Fung, A. K. (1982). *Microwave Remote Sensing: Active and Passive, Volume 2*. Norwood, Massachusetts: Artech House.
Ulaby, F. T., Moore, R. K., & Fung, A. K. (1986). *Microwave Remote Sensing: Active and Passive, Volume 3*.

Norwood, Massachusetts: Artech House.
Wahl, D. E., Yocky, D. A., Bussey, B., & Jakowatz, C. V. (2012). Generating lunar bistatic SAR images using Arecibo and Mini-RF, (May 2012), 83940D–83940D–4. https://doi.org/10.1117/12.923600
Wang, W., Liu, R., Wang, Y., Hu, Q., Shen, C., Jiang, C., & Zhu, C. (2017). Buildup of a highly twisted magnetic flux rope during a solar eruption. *Nature Communications*, *8*(1), 1–11. https://doi.org/10.1038/s41467-017-01207-x
Weitz, C. M., Head, J. W., & Pieters, C. M. (1998). Lunar regional dark mantle deposits: Geologic, multispectral, and modeling studies. *Journal of Geophysical Research E: Planets*, *103*(E10), 22725–22759. https://doi.org/10.1029/98JE02027
Whitford-Stark, J. L. (1982). Factors influencing the morphology of volcanic landforms: An earth-moon comparison. *Earth Science Reviews*, *18*(2), 109–168. https://doi.org/10.1016/0012-8252(82)90050-2
Wieler, R., Etique, P., Signer, P., & Poupeau, G. (1980). Record of the solar corpuscular radiation in minerals from lunar soils: A comparative study of noble gases and tracks. *Lunar and Planetary Science Conference*, *11*, 1369–1393.
Wilcox, B. B., Lucey, P. G., & Gillis, J. J. (2005). Mapping iron in the lunar mare: An improved approach. *Journal of Geophysical Research E: Planets*, *110*(11), 1–10. https://doi.org/10.1029/2005JE002512
Williams, D. A., Fagents, S. A., & Greeley, R. (2000). A reassessment of the emplacement and erosional potential of turbulent, low-viscosity lavas on the Moon. *Journal of Geophysical Research E: Planets*, *105*(E8), 20189–20205. https://doi.org/10.1029/1999JE001220
Willmott, C. J. (1982). Some Comments on the Evaluation of Model Performance. *Bulletin American Meteorological Society*, *11*, 1309–1313. https://doi.org/10.1175/1520-0477
Winske, D., Wu, C. S., Li, Y. Y., Mou, Z. Z., & Guo, S. Y. (1985). Coupling of Newborn Ions to the Solar Wind by Electromagnetic Instabilities and their Interaction with the Bow Shock. *Journal of Geophysical Research*, *90*, 2713–2726.
Wittenberg, L. J., Cameron, E. N., Kulcinski, G. L., Ott, S. H., Santarius, J. F., Sviatoslavsky, G. I. ., … Thompson, H. (1991). *A Review of Helium-3 Resources and Acquisition for use as Fusion Fuel*. Madison WI 53706.
Woodhouse, I. H. (2006). *Introduction to Microwave Remote Sensing*. Boca Raton, FL: Taylor & Francis.
Zhang, W. (2014). Estimate of Lunar TiO2 and FeO with M3 Data. In B. Cudnik (Ed.), *Encyclopedia of Lunar Science* (pp. 1–7). Springer International Publishing. https://doi.org/10.1007/978-3-319-05546-6_13-1
Zhang, W., & Bowles, N. E. (2013). Mapping lunar TiO2 and FeO with M3 data. In *European Planetary Science Congress* (Vol. 8, pp. 1–2).
Zimmerman, M. I., Farrell, W. M., Stubbs, T. J., Halekas, J. S., & Jackson, T. L. (2011). Solar wind access to lunar polar craters: Feedback between surface charging and plasma expansion. *Geophysical Research Letters*, *38*(19), 3–7. https://doi.org/10.1029/2011GL048880
Zisk, S. H., Hodges, C. A., Moore, H. J., Shorthill, R. W., Thompson, T. W., Whitaker, E. A., & Wilhelms, D. E. (1977). The Aristarchus-Harbinger region of the moon: Surface geology and history from recent remote-sensing observations. *The Moon*, *17*(1), 59–99. https://doi.org/10.1007/BF00566853

APPENDIX A

MLP Neural Network Regressor

Feed forward neural networks are a popular choice for non-linear statistical modelling. The MLP regression can be described as a model concerning parametric probability density functions. Typical neural network-based models are generally developed for classification problems or clustering. In contrast, for regression, the neural network model has to be adopted explicitly to approximate real values. In this context, selecting the right network architecture is often found to be difficult. Generally, a few networks are chosen randomly, and the network yielding the best performance among these is selected for further use. In typical use cases, MLP comprises of a static neural network structure having multiple successive hidden layers which are interconnected. These interconnections are represented by their corresponding adaptive weights. Mathematically, the problem of MLP regression is expressed in Rynkiewicz (2011).

The vector of inputs are assumed to be $x = \left(x(1), x(2), \ldots, x(m)\right)^T \in \mathbb{R}^m$. The hidden layer unit i is expressed as a parameter vector $w_i \coloneqq (w_{i1}, w_{i2}, \ldots, w_{im})^T \in \mathbb{R}^m$. Hence, the MLP function associated with k hidden units is written as

$$f_\psi(x) = \beta + \sum_{i=1}^{k} a_i \phi\left(w_i^T x + b_i\right) \tag{A 1}$$

where ϕ is the bounded transfer function, usually sigmoid, and ψ is the parameter vector of the model represented by $(\beta, a_1, \ldots, a_k, b_1, \ldots, b_k, w_{11}, \ldots, w_{1m}, \ldots, w_{k1}, \ldots, w_{km})$. Only real functions are considered. The closed and bounded set of possible parameters is given as $\Theta_k \subset \mathbb{R}^{k(m+2)+1}$. The regression model $S = \{f_\psi(y, x), \psi \in \Theta_k\}$ is considered with

$$Y = f_\psi(X) + \epsilon \tag{A 2}$$

where ϵ is the model noise and X is random input variable. The observed data $(x_1, y_1), \ldots, (x_n, y_n)$ is derived from a true model $(X_i, Y_i)_{i \in \mathbb{N}, i > 0}$ by considering strictly positive integer n. In this regard, for an ψ^0 in the interior of Θ_k, the true regression function is denoted by f_{ψ^0}. Hence, the probability distribution function of (X_i, Y_i) is P_d. The true estimation of ψ^0 is provided by minimizing the mean squared error function $E_n(\psi)$ with respect to the parameter vector $\psi \in \Theta_k$ in the non-linear regression.

$$E_n(\psi) \coloneqq \frac{1}{n} \sum_{t=1}^{n} \left(y_t - f_\psi(x_t)\right)^2 \tag{A 3}$$

The typical representation of the MLP neural network is illustrated in Figure 30.

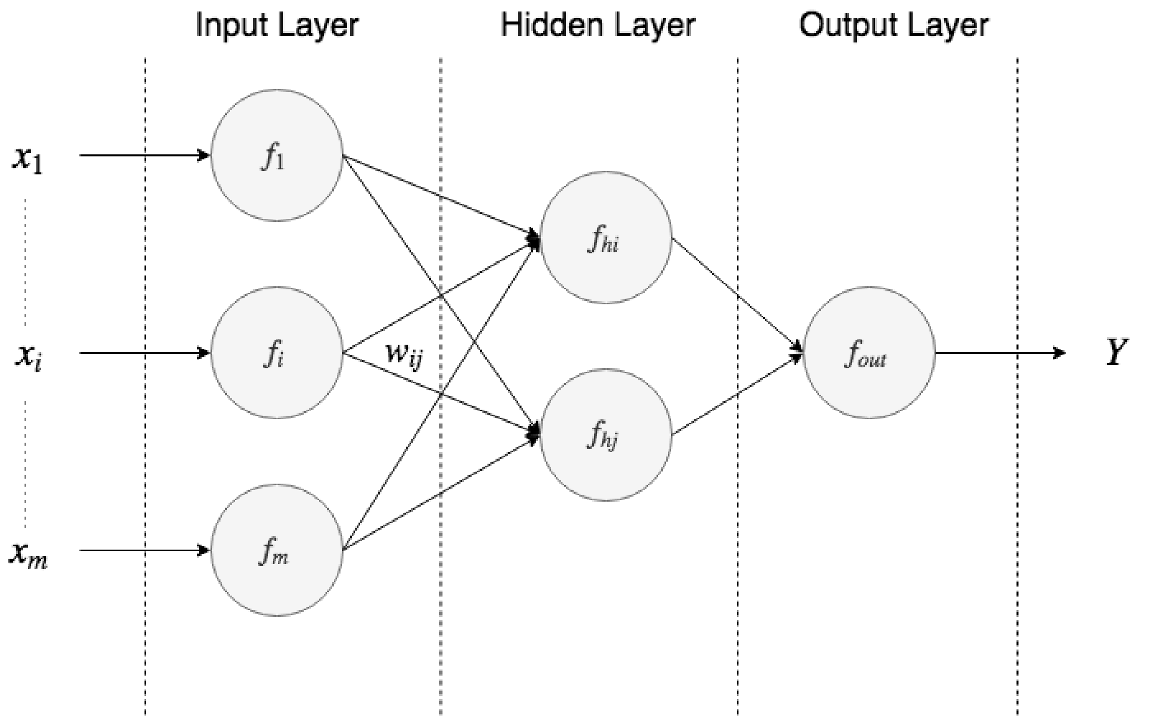

Figure 30: Schematic diagram of generic neural network with f_i representing the activation function of the i^{th} node.

APPENDIX B

The Chandrayaan – 1 M^3 spectral data is co-registered with the LRO MiniRF bistatic data by incorporating the topographic information from the GLDEM100. The framework for computing the error estimate with an elevation between the two images (RMSE_{topo}) requires the selection of a seed point, which is the most approximate feature location in both images. The prior information of the RMSE of each individual point, obtained through 2D co-registration approach, is utilized for defining a selection criterion. Hence, the point corresponding to the least RMSE is chosen as a suitable seed point. In Figure 31, point #21 displays a minimal RMSE of 0.0021 with a negligible error in the Y direction (-0.0003). The dimensionality of the point is usually resolved by associating the elevation information with it. This quantifies the separation of the seed point (#21) with all other points in the 3D space. Following the approach for 26 points, there is a decrease in the RMSE from 0.338 pixel to 0.222 pixel with respect to the base image. The associated uncertainty in the seed point measurement is estimated as 0.0525 (=0.222 × 26). Two major feature geometries, i.e. circular Herodotus crater and linear Vallis Schroteri rille, are highlighted in Figure 32. The overlapping of the image after co-registration represents minimal mismatching between the features. However, due to the different illumination conditions for both sensors, the overlapping seems misrepresented in certain regions, which in fact is not true whilst observing the zoomed images.

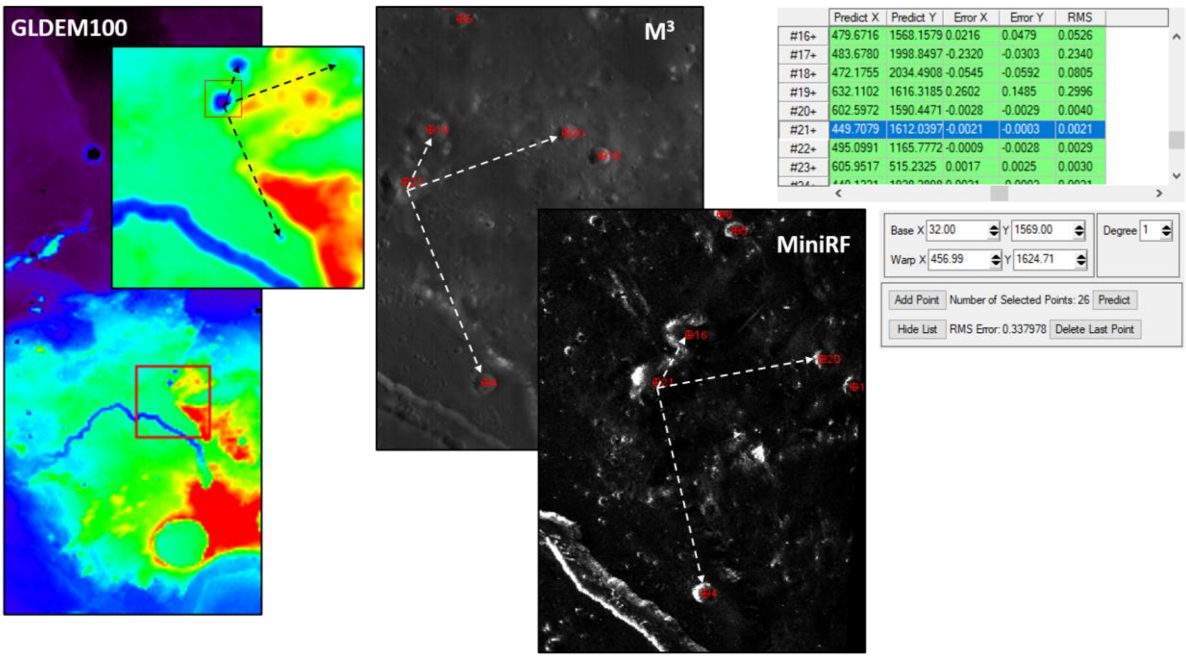

Figure 31: Co-registration approach for the M^3 and MiniRF data by taking into account the GLDEM100. The statistics shows the estimation of the 2D co-registration, with highlighted blue colour representing the seed point. The dotted line arrow depicts the separation of seed point and other points.

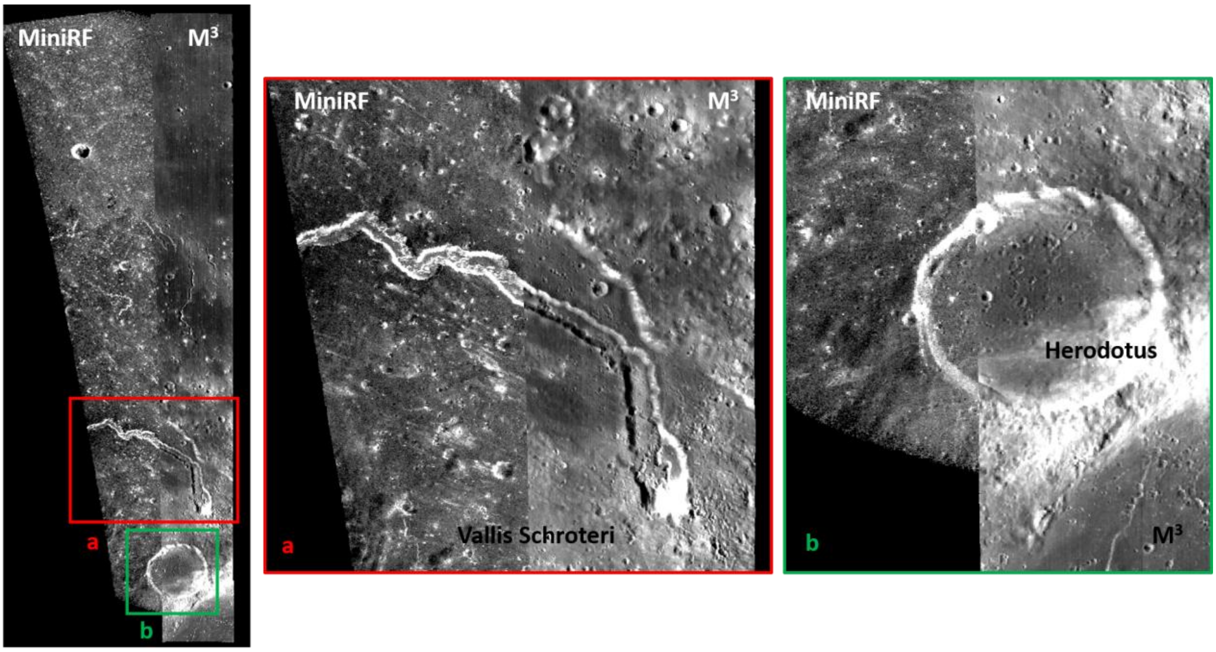

Figure 32: Co-registration results of the M^3 and MiniRF data strip. a) Vallis Schroteri representing the linear feature, and b) Herodotus crater representing the circular feature.

APPENDIX C

The cross-variogram plots for the retained ^{3}He with respect to the petrophysical indicators of the regolith are illustrated in this section. Two zones are specified for the analysis: Low ^{3}He abundant Ejecta regolith and High ^{3}He abundant pyroclastic regolith.

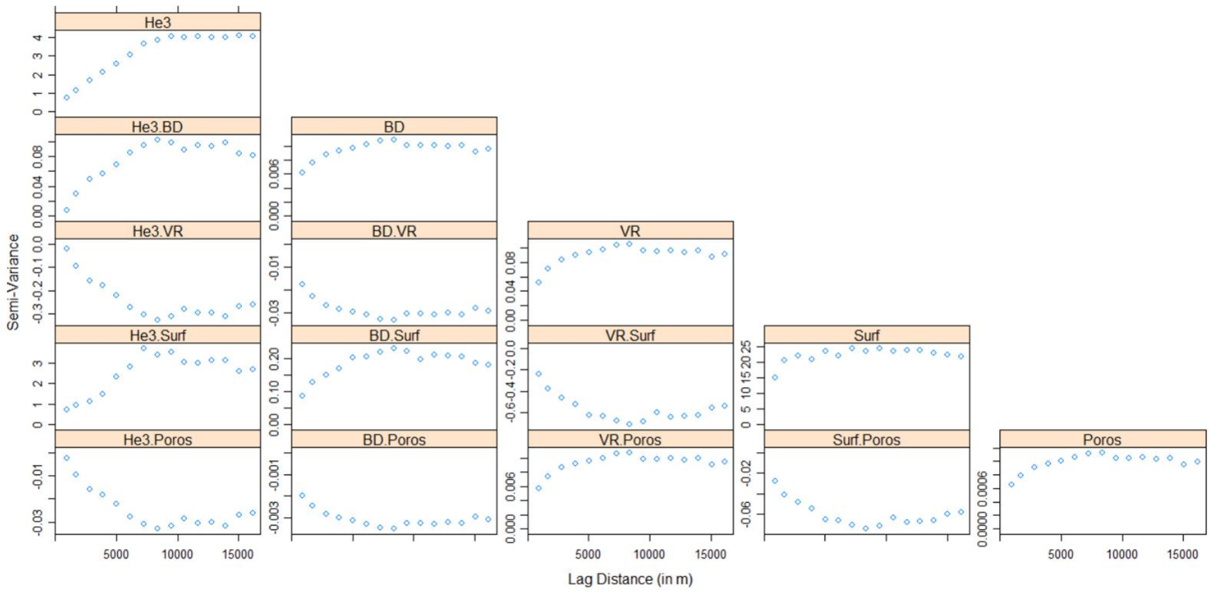

Figure 33: Cross-variogram between ^{3}He and physical properties of the low abundant ejecta cover regolith.

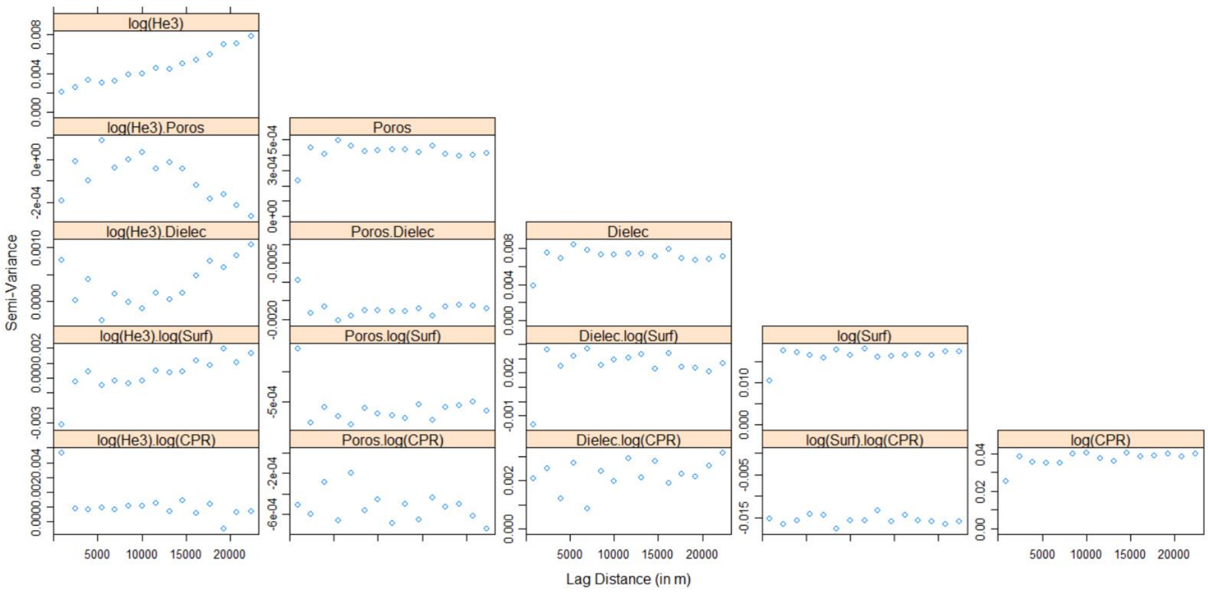

Figure 34: Cross-variogram between ^{3}He and physical properties of the high abundant pyroclastic regolith.